Title
Time-scales of crustal anatexis: monazite petrochronology of Himalayan granites

Author
Lederer, Graham William

Publication Date
2014

UNIVERSITY OF CALIFORNIA

Santa Barbara

Time-scales of crustal anatexis: monazite petrochronology of Himalayan granites

A dissertation submitted in partial satisfaction of the
requirements for the degree Doctor of Philosophy
in Geological Sciences

by

Graham William Lederer

Committee in charge:
Professor John M. Cottle, Chair
Professor Bradley R. Hacker
Professor Frank J. Spera

September 2014

The dissertation of Graham William Lederer is approved.

Bradley R. Hacker

Frank J. Spera

John M. Cottle, Committee Chair

September 2014

ACKNOWLEDGEMENTS

The work presented herein would not have been possible without the help and support of many individuals. Foremost, I would like to thank Dr. John Cottle, who has served as my mentor, supervisor, editor, and source of guidance for the past five years. In addition to serving as committee members, Professors Brad Hacker, Phil Gans, and Frank Spera have provided me with very useful academic insight and professional advice. Drs. Andrew Kylander-Clark and Gareth Seward provided valuable technical expertise with the analytical facilities at UCSB, and thanks are due to the many undergraduate and graduate students who have helped me along the way. Interdisciplinary research in the Himalaya was made possible through the dedicated efforts of my collaborators Micah Jessup, Jackie Langille, Talat Ahmad, Santa Man Rai, Dawn Kellett, Janelle McAtamney and especially Kyle Larson. Elizabeth Lee, Jacob Poletti, and Tyler Ambrose provided good company and valuable field assistance during my three excursions to India and Nepal. Teke, Pradap, Ngawang, Pemba, Chhiring, Bal Bahadur, Purna, Ash Kumar, Aurun, and Mongol Singh Tamang of Lapcha provided logistical trekking support to remote areas in Nepal, and the hospitality of the people of Nepal and Himachal, especially Chhang Dorje Lama in Philim, deserves mention. Special thanks go to residents of the Continental, as well as friends and family across the country. I would not have survived without the love, support, and patience of my parents, Jenny and Will, or my girls, Hannah and Ava.

Graham W. Lederer

Curriculum Vitae
Department of Earth Science
University of California
Santa Barbara, CA 93106
grahamlederer@umail.ucsb.edu

EDUCATION

2014	Ph.D.	Geological Sciences, University of California Santa Barbara Dissertation title: Time-scales of crustal anatexis: monazite petrochronology of Himalayan granites Advisor: Dr. J. M. Cottle
2009	B.S.	Geology and Environmental Science, College of William and Mary Honors thesis title: Geology and structural history of the Blue Ridge basement complex, Albemarle County, Virginia Advisor: Dr. C. M. Bailey

RESEARCH EMPHASES

U-Th/Pb geochronology; monazite; trace element geochemistry; granite petrogenesis; crustal anatexis; melt generation, migration and emplacement; structural mapping; rare earth element mineralization; collisional orogenesis; gneiss dome formation and exhumation; Himalaya; Grenville

PROFESSIONAL EXPERIENCE

2014-present	Lecturer, *Geological Catastrophes,* University of California Santa Barbara
2009-present	Graduate Student Researcher, University of California Santa Barbara
2009-2013	Graduate Teaching Assistant, University of California Santa Barbara *Courses taught: geological catastrophes, physical geology, summer field geology, geochronology, petrology, optical mineralogy, analytical methods*
2011	Geologist, United States Geological Survey, Reston, Virginia
2008	Undergraduate Teaching Assistant, College of William and Mary
2007-2008	Undergraduate Student Researcher, College of William and Mary

HONORS AND AWARDS

2013	Doctoral Student Travel Grant, University of California Santa Barbara
2012	ExxonMobil Global Recruiting Grant
2011-2012	Dean's Fellowship Award, University of California Santa Barbara
2011	Preston Cloud Memorial Award, University of California Santa Barbara
2011	Outstanding Student Poster, Geological Society of America Fall Meeting
2009	Cum Laude with High Honors in Geology, College of William and Mary
2009	Alumni Association Award in Geology, College of William and Mary
2005-2009	Robert C. Byrd Honors Scholarship, Maryland Department of Education
2005	Valedictorian (GPA 4.00) Sherwood High School, Sandy Spring, MD

SHORT COURSES/CONFERENCES ATTENDED

2014	Linkages and Feedbacks in Orogenic Processes, GSA Penrose Conference, Asheville, NC
2013	Cooperative Institute for Dynamic Earth Research Program, UC Berkeley
2013	Imperial Barrel Award (IBA) Subsurface Characterization Course: *Introduction to Sequence Stratigraphy*, UCSB
2013	ExxonMobil Short Course: Salt Tectonics and Hydrocarbon Systems, UCSB
2011	U-Pb Geochronology by LA-ICPMS: Detrital and Petrochronology Applications, AGU Fall Meeting
2010	ExxonMobil Guadalupe Mountains Field Course, New Mexico/Texas

FIELD EXPERIENCE

Coastal California, Owens Valley, Panamint Valley, Death Valley, Mojave, eastern California; Nepal; northwest India; Blue Ridge, Virginia; Fish Lake Plateau, Utah; Snake Range, eastern Nevada; Big Bend, Texas; Guadalupe Mountains, New Mexico; northwest Scotland; central Spain;

PROFESSIONAL MEMBERSHIPS

2009	Mineralogical Society of America
2009	American Geophysical Union
2009	Geological Society of America
2013	American Association of Petroleum Geologists

PEER REVIEWED PUBLICATIONS

Lederer, G., Cottle, J., Jessup, M., Langille, J., and Ahmad, T., 2013, Timescales of partial melting in the Himalayan middle crust: insight from the Leo Pargil dome, northwest India, Contributions to Mineralogy and Petrology, doi: 10.1007/s00410-013-0935-9

Langille, J., Jessup, M., Cottle, J., **Lederer, G.**, and Ahmad, T., 2012, Timing of metamorphism, melting and exhumation of the Leo Pargil dome, northwest India. Journal of Metamorphic Geology, 30: 769–791. doi: 10.1111/j.1525-1314.2012.00998.x

CONFERENCE ABSTRACTS

Lead author:

Lederer, G., 2014, Timescales of crustal anatexis during collisional orogenesis: insight from monazite petrochronology of Himalayan leucogranites, Linkages and feedbacks in orogenic systems: GSA Penrose Conference.

Lederer, G., Cottle, J. Larson, K., McAtamney, J, Moulton, K., Kellett, D., 2013, Petrochronologic study of granites in the eastern Nepal Himalaya, Eos Transactions American Geophysical Union, v. 94.

Lederer, G., Cottle, J., Jessup, M., Langille, J., and Ahmad, T., 2011, Monazite in Himalayan leucogranites: investigating melt systematics in the mid-crust, GSA Abstracts with Programs, v. 43, p. 609.

Lederer, G., Cottle, J., Jessup, M., Langille, J., and Ahmad, T., 2010, Temporal constraints on partial melting and deformation in the Himalayan mid-crust, Leo Pargil Dome, NW India, Eos Transactions American Geophysical Union, v. 91.

Lederer, G., Cottle, J., Jessup, M., Langille, J., and Ahmad, T., 2010, Petrochronologic constraints on partial melting in the Leo Pargil Dome, NW India, Geochimica et Cosmochimica Acta, v. 74, p. A572.

Lederer, G., Cottle, J., Jessup, M., Langille J., and Ahmad, T., 2010, Time-scales of crustal melting within the Leo Pargil Dome, NW India, in Leech, M.L., Klemperer, S.L., and Mooney, W.D., eds., Proceedings of the 25th Himalaya-Karakoram-Tibet Workshop: U.S. Geological Survey Open-File Report 2010-1099, 242 p.

Lederer, G., and Bailey, C., 2009, Geology and structural history of the Blue Ridge basement complex in Albemarle County, Virginia, GSA Abstracts with Programs, v. 41, p. 56.

Contributing Author:

McKinney, S., Cottle, J., Lederer, G., Granneman, P., 2014, Evaluating mechanisms for rare earth element mineralization in Proterozoic gneiss, Music Valley, CA, Geochimica et Cosmochimica Acta

McAtamney, J., Cottle, J., Larson, K., **Lederer, G.**, Rai. S.M., 2013, Microstructural insights into strain variation along the Main Central thrust system; eastern Nepal Himalaya, Geological Society of America Abstracts with Programs, v. 45.

Langille, J., Jessup, M., Cottle, J., **Lederer, G.**, and Ahmad, T., 2011, Insights into metamorphism, crustal melting, and exhumation of the Leo Pargil Dome, Western Himalaya, from monazite geochronology, Geological Society of America Abstracts with Programs, v. 43, p. 608.

Langille, J., Jessup, M., Cottle, J., **Lederer, G.**, and Ahmad, T., 2010, Kinematic and timing constraints on the Leo Pargil Shear Zone: Implications for extension during exhumation of the Leo Pargil Dome, NW India, Geological Society of America Abstracts with Programs, v. 42, p. 619.

Jessup, M., Cottle, J., Langille, J., **Lederer, G.**, and Ahmad, T., 2010, Strain partitioning and crustal melting within the Leo Pargil Dome, NW India, Geological Society of America Abstracts with Programs, v. 42, p. 664.

Langille J., Jessup, M, Cottle, J., **Lederer, G.**, and Ahmad, T., 2010, Timing of metamorphism and extension in the western Himalaya: Leo Pargil Dome, NW India, Geochimica et Cosmochimica Acta, v. 74, p. A558.

Langille, J., Jessup, M., Cottle, J., **Lederer, G.**, and Ahmad, T., 2010, Timing of metamorphism and extension in the western Himalaya: Leo Pargil Dome, NW India, in Leech, M.L., Klemperer, S.L., and Mooney, W.D., eds., Proceedings of the 25th Himalaya-Karakoram-Tibet Workshop: U.S. Geological Survey Open-File Report 2010-1099, 242 p.

Jessup, M., Cottle, J., Langille, J., **Lederer, G.**, and Ahmad, T., 2010, Contrasting dome formation along the southern margin of the Tibetan plateau: Leo Pargil Dome and Ama Drime Massif, India/Tibet, in Leech, M.L., Klemperer, S.L., and Mooney, W.D., eds., Proceedings of the 25th Himalaya-Karakoram-Tibet Workshop: U.S. Geological Survey Open-File Report 2010-1099, 242 p.

Laskowski, A., Bailey, C., Nicholls, O., Garber, J., Knieser, B., **Lederer, G.**, and Murray, L., 2009, The Sugar Hollow Basin: a Neoproterozoic half graben complex in the central Virginia Blue Ridge, Geological Society of America Abstracts with Programs, v. 41, p. 55.

Gattuso, A.P., Bailey, C., Lemon, C., **Lederer, G.**, Hartmann, A., and Knuth, F., 2008, Geology of the Crozet 7.5' quadrangle, Blue Ridge Province, Virginia, Geological Society of America Abstracts with Programs, v. 40, p. 12.

ABSTRACT

Timescales of crustal anatexis: monazite petrochronology of Himalayan granites

by

Graham William Lederer

Accessory phases, such as monazite, xenotime, and zircon, record a wealth of information regarding the timing, duration, and sources of crustal melting. Combined U-Th/Pb and REE analysis of these petrochronometers by laser ablation split stream inductively coupled plasma mass spectrometry (LASS-ICPMS) reveals complex spatiotemporal relationships on a range of scales, from distinct chemical domains within a single crystal, to cross-cutting dikes within heterogeneous plutons composed of multiple melt batches. The anatectic core of the Himalaya exposes mid-crustal rocks well suited for investigations of the time-scales involved in melt processes, such as generation, segregation, amalgamation, mobilization, and emplacement. Three examples from different settings within the Himalayan orogen, including 1) the Leo Pargil leucogranite injection complex exposed in a gneiss dome in the hinterland, 2) the Manaslu pluton at the interface between the anatectic core and overlying metasediments, and 3) Everest region and Mahabharat granites from the anatectic core to the crystalline thrust sheet of the foreland, illustrate the value of monazite for deciphering crystallization in source rocks and/or earlier melt batches in addition to determining granite emplacement age.

TABLE OF CONTENTS

LIST OF FIGURES AND TABLES

1. Introduction

The Himalaya form the highest mountains on Earth, and represent the culmination of tectonic processes in the ongoing continent-continent collision between India and Asia since ~55 Ma. Due to extensive erosion and development of astonishing vertical relief, the Himalaya provide an informative view into the crustal architecture of an active orogen. The high-grade metamorphic and anatectic core of the orogen, the Greater Himalayan Sequence (GHS), forms a remarkably continuous belt along the >2000 km length of the range, and in addition to forming many of the highest peaks, is also exposed by extensional structures in the Tibetan hinterland as well as in thrust sheets of the Indian foreland (Fig 1.1).

The focus of this work is to elucidate the timing of partial melting processes within the Himalayan middle crust at three different orogenic settings, each of which forms the basis for one chapter. The first chapter focuses on the granites of the Leo Pargil dome of northwest India, where orogen-parallel extensional structures have exposed mid-crustal rocks within the hinterland of the orogen. The second chapter investigates the granites and host gneisses of the GHS along a ~100 km N-S transect from the Everest region to the Mahabharat range in eastern Nepal, with particular emphasis on the changes in melt production from hinterland to foreland. The third chapter reexamines the timescales of granite generation and emplacement of the extensively studied Manaslu pluton in central Nepal, which occurs at the interface between the GHS and overlying sediments.

Through petrochronologic investigation, three essential questions are addressed: 1) Over what timescales do melt generation, transport, and emplacement operate? 2) Do compositionally heterogeneous granites represent mixing of melt batches from distinct

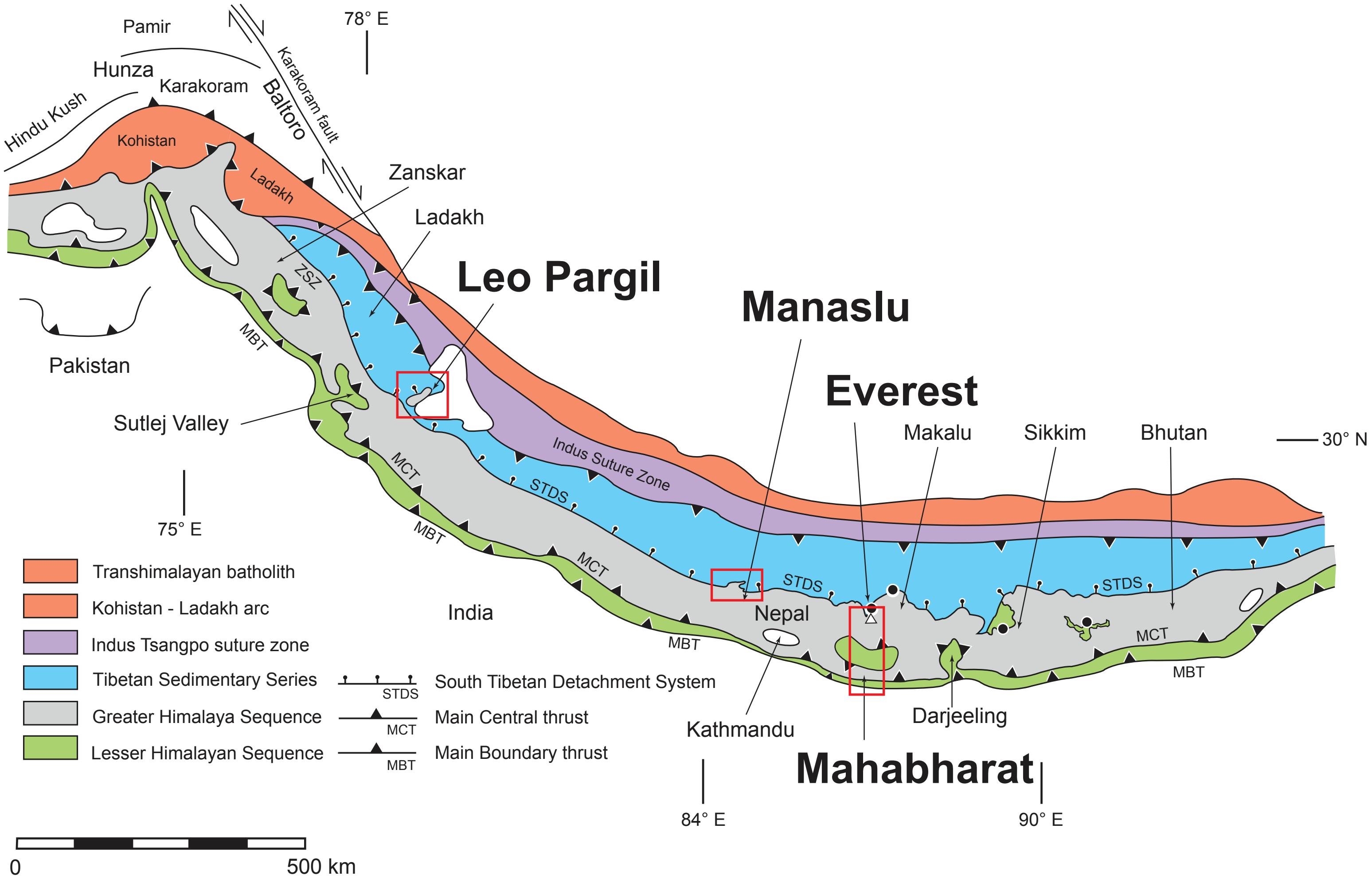

Figure 1.1 Geologic map of the Himalaya (after Searle 2013) with study areas indicated by red boxes.

sources or the chemical evolution of a single source? 3) How are large plutons assembled compared to individual granite bodies? The answers to these questions have direct bearing on tectonic models proposed for specifically for the Himalaya, and in general for the evolution of continent-continent collisional orogens.

1.1 The Greater Himalayan Sequence

The Greater Himalayan Sequence (GHS) represents the orogenic core of the Himalaya and consists of a ~2000-km-long continuous belt of schists and gneisses pervasively intruded by leucogranites derived from partial melting of crustal sources (Fig. 1.1). The GHS was emplaced over low-grade metasedimentary rocks and Paleoproterozoic granitoid gneisses of the Lesser Himalayan Sequence (LHS) along the Main Central thrust (MCT), an orogen-scale structure consisting of a broad ductile shear zone and brittle thrust faults. The upper contact of the GHS is the South Tibetan Detachment (STD), which displaced Paleozoic-Tertiary sediments of the Tibetan sedimentary series (TSS) along a system of brittle normal faults and low-angle detachments (Fig. 1.2).

The GHS is characterized by an inverted metamorphic gradient at its base, and a normal metamorphic gradient at its top (Grujic, 1996; Fig. 1.2). From biotite-grade schists and gneisses of the lower GHS in the immediate hanging wall of the MCT, metamorphic grade increases up section to sillimanite-grade migmatites of the upper GHS. GHS schists and gneisses are pervasively deformed, and tectonic thinning of the GHS by dominantly pure shear resulted in telescoping of metamorphic isograds to a thickness of less than 10 km. The rapid decrease in metamorphic grade at the top of the GHS is inferred to reflect exhumation along the STD (Fig. 1.2). The GHS experienced

a) Model 1: Lower GHS records highest P-T (i.e. Kohn, 2014)

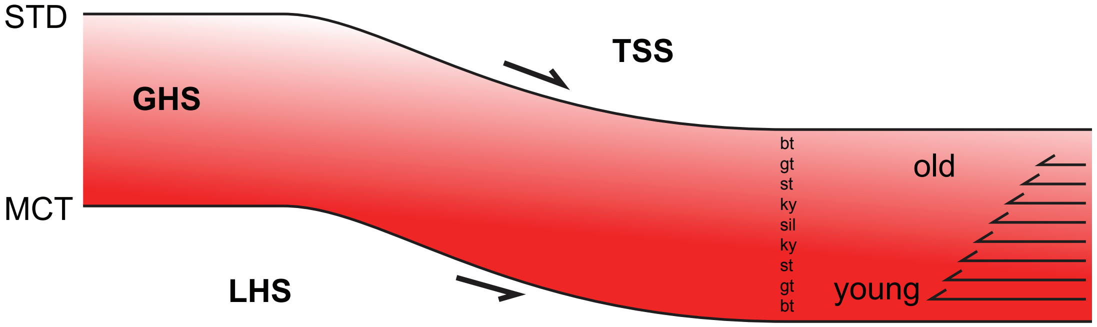

b) Model 2: Middle GHS records the highest P-T (i.e. Searle, 2013)

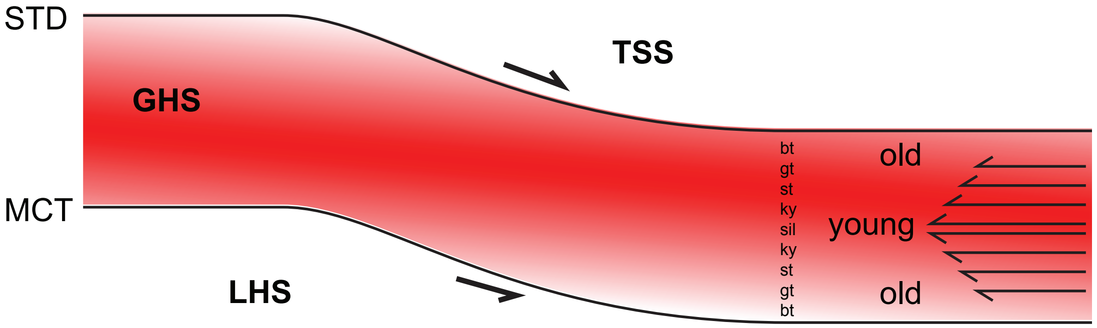

c) Model 3: Hybrid model involving migration of the MCT (i.e. Larson, 2010)

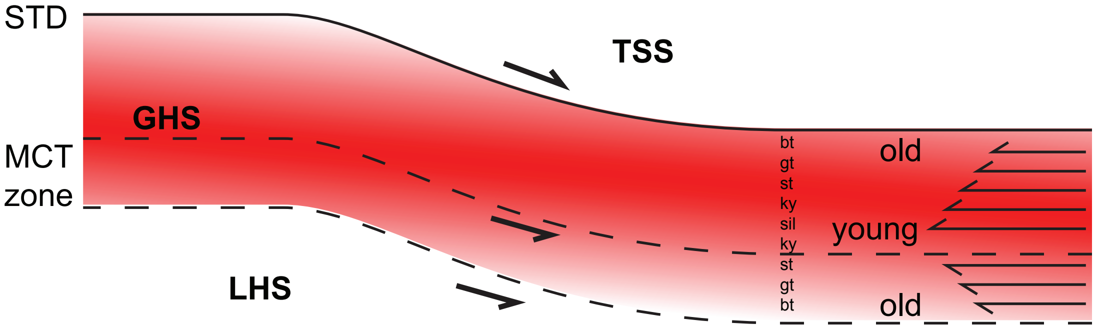

Figure 1.2 Different geodynamic models for the evolution of Greater Himalayan Sequence (GHS) include a) critical taper, b) channel flow, and c) a hybrid model that predicts predict different age relationships for melting in relation to bounding structures. TSS, Tibetan Sedimentary series; LHS, Lesser Himalayan Sequence; MCT, Main Central thrust; STD, South Tibetan Detachment.

prograde metamorphism from the Eocene to Oligocene (30-23 Ma), followed by isothermal decompression in the Miocene (20-16 Ma).

Granite bodies within the GHS range in size from cm-scale dikes to km-scale plutons, and occur in a variety of tectonic settings, from extensional domes in the hinterland, to thrust sheets in the foreland (Fig. 1.1). Leucogranite dikes occur above the kyanite isograd, but are more pervasive and volumetrically significant at structurally higher positions. Locally, leucosome segregations in migmatites can be traced into boudinaged and deformed leucogranite sills as well as dikes that cut across host rock foliations. Dikes and sills form interconnected injection complexes and feed broad laccolithic sheets of leucogranite up to 10-km-thick at the structurally highest positions in the GHS. The field relationships indicate a protracted history of melting and provide evidence for multiple melt batches resulting in early and late granites.

Geophysical evidence (Makovsky et al. 1996; Chen et al. 1996; Nelson et al. 1996; Brown et al. 1996; Unsworth et al. 2005) and petrologic constraints (Hacker, 2000; Hacker et al. 2014) indicate the middle to lower crust underwent partial melting at depths greater than 20 km beneath the Tibetan plateau.

The associations between metamorphism, melting, and deformation have prompted the development of several geodynamic models that attempt to fit available geologic constraints. The channel flow model (Beaumont et al. 2001, 2004) hypothesizes that partial melting reduced the effective viscosity of the middle crust, facilitating the exhumation of the GHS towards a zone of focused erosion bounded by coeval structures with opposing sense of shear. The model requires a minimum of ~2-5% partial melt is present at a given time and predicts that the most recent melting and youngest granites occur in the structurally deepest portions of the GHS. By contrast, critical taper or frictional wedge models invoke exhumation of the GHS rocks occurred mainly along a series of foreland propagating, in-sequence thrust faults and do necessarily predict a relationship between deformation and melting, although shear heating along major thrust faults may have provided additional heat to facilitate melting.

1.2 Monazite petrochronology

Geologic context, from the regional to local to microstructural scales, underpins each of the three studies presented here and therefore serves as an underlying thread of continuity between the projects. Field-based methods, including map-scale coverage and targeted sampling of different generations of granites based on outcrop-scale relations, form the foundation for further laboratory analysis. By progressively narrowing of the scale of observation and then reversing this process by building and lumping components together, a detailed, yet complete approach to the problem at hand is attempted.

Petrochronology combines detailed petrologic observations with the spatial resolution of laser ablation split stream inductively coupled plasma mass spectrometry (LASS-ICPMS) to measure trace elements and radiogenic isotopes of individual chemical domains of accessory mineral phases. Typically, the mineral zircon is utilized in geochronologic applications because of its high closure temperature and refractory character. Zircon U-Pb geochronology of Himalayan granites is complicated by the widespread occurrence of inherited detrital zircons with small magmatic overgrowths. For this reason, zircon analyses are used in this study to a lesser extent. Monazite is a light rare earth element (LREE) phosphate mineral that incorporates significant amounts of Th and U, and is more likely to record new growth during partial melting than zircon. Although monazite U-Th/Pb systematics can be complicated by compositional zoning

(Williams et al. 1999), secular disequilibrium (Schärer, 1984) and inheritance (Copeland et al. 1988; Harrison, McKeegan, et al. 1995; Harrison et al. 1999), LASS-ICPMS analysis provides spatial resolution of <10 μm, sufficient to repeatedly measure chemical domains. Furthermore, LASS-ICPMS permits rapid characterization of multiple monazite grains per sample and collection of large datasets that provide robust statistics. Comparison of monazite dates with zircon and xenotime dates provides insight into the behavior of these accessory phases during melting and metamorphism.

2. Time-scales of partial melting in the Himalayan middle crust: insight from the Leo Pargil dome, northwest India

2.1 Abstract

The Leo Pargil dome (LPD) in northwest India exposes an interconnected network of pre-, syn-, and post-kinematic leucogranite dikes and sills that pervasively intrude amphibolite-facies metapelites of the mid-crustal Greater Himalayan Sequence. Leucogranite bodies range from thin (5-cm-wide) locally-derived sills to thick (2-m-wide) cross-cutting dikes extending at least 100 m. Three-dimensional exposures elucidate cross-cutting relations between different phases of melt injection and crystallization. Combined laser ablation inductively coupled plasma mass spectrometry (LA-ICPMS) U-Th/Pb geochronology and trace element analysis on well-characterized monazite grains from nineteen representative leucogranites yields a large, internally consistent dataset of approximately 700 U-Th/Pb and 400 trace element analyses. Grain-scale variations in age correlate with trace element distributions and indicate semi-continuous crystallization of monazite from 30 to 18 Ma. The youngest U-Th/Pb ages in a given sample are consistent with the outcrop-scale cross-cutting relations, whereas older ages within individual samples record inheritance from partially crystallized melt and source metapelites. U-Th/Pb isotopic and trace element data are incorporated into a model of melting within the LPD that involves 1) steady-state equilibrium batch melting of compositionally homogeneous metapelitic sources; 2) pulses of increased melt mobility lasting 1 to 2 m.y. resulting in segregation of melt from its source and amalgamation into mixed magmas; and 3) rapid emplacement and final crystallization of

leucogranite bodies. Melt systems in the LPD evolved from locally-derived, in-situ melt in migmatitic source rocks into a vast network of dikes and sills in the overlying non-migmatitic host rocks.

2.2 Introduction

Continental collisions produce the most prominent mountain ranges in the world and expose middle to lower crustal rocks key to understanding the dynamic links between metamorphism, melting, and deformation in orogenic systems. Resulting from the Cenozoic collision of the Indian and Eurasian plates, the Himalaya provide an excellent location to study active orogenic processes and test geodynamic models that attempt to explain the inter-relationships between crustal thickening, ductile deformation, exhumation, and climate. Such models require a thorough understanding of how crustal rheology evolves through space and time.

A key factor controlling the rheological evolution of the crust is partial melting (e.g. review in Jamieson et al. 2011). Laboratory experiments (Rosenberg and Handy, 2005), theoretical calculations (Paterson, 2001), and field-based analysis (Schulmann et al. 2008) together indicate that small (<10%) fractions of partial melt can dramatically reduce the effective strength of the crust by ~ 600-700 MPa (differential stress). Rosenberg and Handy (2005) argued that the drop in strength, which they termed the ‘melt connectivity threshold’, is related to formation of interconnected networks of melt at grain boundaries. Because the strength drop is so dramatic, melting of the crust in orogenic systems has the potential to cause significant crustal weakening and associated localization of strain into melt-rich horizons (Jamieson et al. 2011).

Despite the clear link between melting and reduction in effective crustal strength, key questions remain regarding the time-scales of over which melting occurs in collisional orogens. Can conditions in the crust conducive to partial melting be maintained over large portions of the orogenic history (e.g. Viskupic and Hodges 2001) or is melting a transient and short-lived phenomena that occurs over only a small portion of the orogenic cycle (e.g. Collins and Williams 1995; Friedrich et al. 1999)? Answers to these questions help delineate the relative importance of melting in controlling the long-term rheological evolution of the crust during collisional orogenesis.

In an attempt to further understand the time-scales over which partial melt is produced, modified, transported, and crystallized, this study presents monazite petrography, U-Th/Pb, and rare earth element (REE) data from the Leo Pargil Dome (LPD) in the northwest Indian Himalaya. Our analysis indicates that melts were generated in migmatitic source regions and intruded into shallower crustal levels over a timespan of 12 m.y. through pulses of magmatism lasting 1-2 m.y. Furthermore, monazite geochronology and geochemistry suggest that the source of melting is distinct from the metamorphic rocks that host the leucogranites, and that, relative to the overall orogenic cycle, there is significant residence time of melt in the mid-crust during segregation and amalgamation prior to final mobilization and emplacement.

2.2.1 Partial melting in the Himalaya

Geologic and geophysical evidence for partial melting in the Himalaya includes abundant migmatite and leucogranite dikes and sills exposed in the Greater Himalayan Sequence (GHS), kilometer-scale leucogranite plutons the upper portion of the GHS, and bright-spots imaged beneath the Tibetan plateau, inferred to represent melt currently forming at 15-20 km depths (Makovsky et al. 1996; Chen et al. 1996; Nelson et al. 1996; Brown et al. 1996; Unsworth et al. 2005). Himalayan leucogranites are derived from fluid-absent incongruent melting of muscovite in metapelites and metagreywackes of the GHS at temperatures of 650 to 750ºC during decompression between 9 and 4 kbar (Harris and Massey 1994; Prince et al. 2001; Scaillet et al. 1990; Scaillet et al. 1996; Searle et al. 1999; Searle et al. 2010).

Due to the positive slope of the muscovite-dehydration reaction in P-T space, melting requires an increase in temperature and/or a decrease in pressure (Clemens and Vielzeuf, 1987). Three heat sources potentially contribute toward melting: 1) heat conducted from the mantle through the base of crust; 2) radiogenic heat produced by U, Th, and K in the crust; and 3) viscous or shear heating along high-strain zones (England and Thompson, 1984; Thompson and Connolly, 1995; Royden, 1993; Nabelek and Liu, 2007; Nabelek et al. 2010). A decrease in the apparent lithostatic pressure during rapid tectonic and erosional exhumation may also trigger melting (Zeitler et al. 2001). Possible feedbacks between melt production and exhumation have also been proposed (Lee et al. 2000, 2004; Teyssier and Whitney, 2002; Beaumont, 2004).

2.2.2 Geologic Setting

The Himalayan orogen, located along the southern margin of the Tibetan plateau, consists of a ~2500-km-long topographic arc bounded by the Namche Barwa and Nanga Parbat syntaxes to the east and west, respectively (Hodges 2000; Fig. 2.1 inset). Previous workers have distinguished three regionally extensive tectonostratigraphic units—the Lesser Himalayan Sequence (LHS), the GHS, and the Tibetan sedimentary series (TSS)—separated by two major north-dipping fault systems—the Main Central thrust

a)

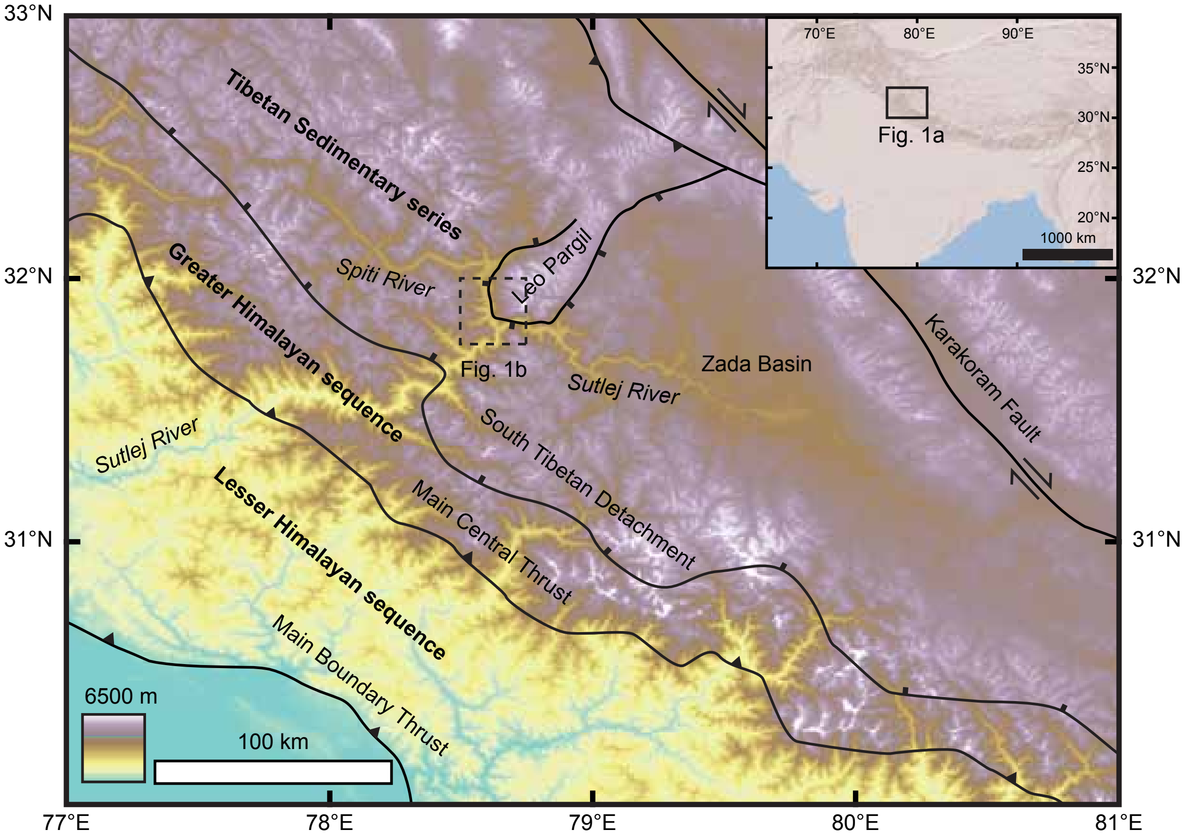

Figure 2.1 Geologic map of Leo Pargil and its position within the Himalayan orogen. a) Topographic overview map of northwest India highlighting orogen-scale units and structures (modified from Thiede et al. 2006). Inset map shows location.

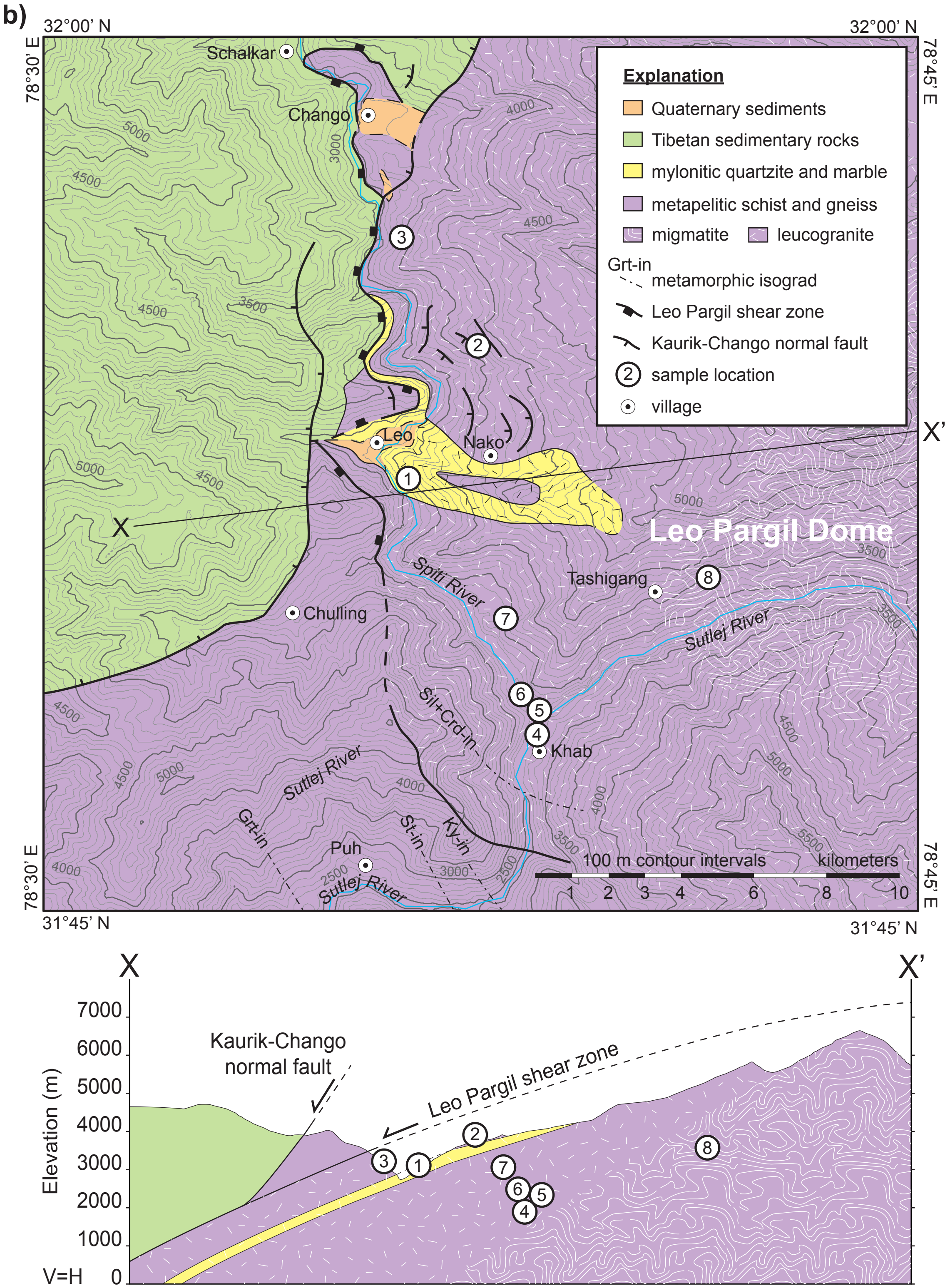

Figure 2.1 (continued) b) Detailed geologic map and cross section of the Leo Pargil dome (from Langille et al. 2012). Sample locations are projected into the cross-section to illustrate structural position.

(MCT) and the South Tibetan Detachment system (STD) (Gansser 1964; Hodges 2000; Fig. 2.1a).

The crystalline GHS lies between the MCT and the STD and consists of late Proterozoic to early Cambrian metasedimentary and meta-igneous rocks with abundant migmatite and leucogranite. The overlying TSS represents late Proterozoic through early Tertiary passive margin sediments that did not experience the high-grade regional metamorphism recorded by the GHS (Hodges 2000). Within the TSS, several domes expose high-grade metamorphic rocks and anatectic granites originating from extension, contraction, diapirism, or some combination thereof (Lee et al. 2004; Zhang et al. 2004; Murphy et al. 2002; Thiede et al. 2006; Aoya et al. 2005).

Recent geodynamic models attempt to explain the evolution of the GHS and bounding structures by channel flow, or gravity-driven southward movement of partially molten rock within a mid-crustal channel due to a gradient in lithostatic pressure between the Tibetan plateau and the Himalayan foreland and associated ductile extrusion of the GHS accommodated by simultaneous movement on the reverse-sense MCT and the normal-sense STD (see Godin et al. 2006 and references therein for a review). Recent work by Beaumont and Jamieson (2010) and Larson et al. (2010) suggests that the channel flow model and alternative frictional critical taper models (Bollinger et al. 2006; Robinson et al. 2006; Kohn, 2008) may in fact represent parts of the same mechanism in which there is a transition between hinterland gravity-driven channel flow deformation and foreland frictional fold-and-thrust belt deformation. The duration over which partially molten material persists within the mid-crust represents a critical factor in the evaluation of such models.

2.2.3 Leo Pargil dome

This study seeks to further refine the evolution of leucogranites within the middle crust by investigating the LPD. The LPD was chosen because its metamorphic and exhumational history as well as its relationship to orogen-scale structures are fairly well-understood (e.g. Chambers et al. 2009; Hintersberger et al. 2010; Langille et al. 2012; Thiede et al. 2006; Thöni et al. 2012; Fig. 2.1).

Leo Pargil represents an example of a dome formed by orogen-parallel extension (Thiede et al. 2006). The LPD consists of a high-grade metamorphic and anatectic core juxtaposed against low-grade Tibetan metasedimentary rocks by the Leo Pargil shear zone (LPSZ) and the Kaurik-Chango normal fault system. The LPSZ is a broadly distributed low-angle, normal-sense shear zone (Fig. 2.1b). Leucogranite dikes and sills pervasively intrude kyanite-bearing schist and gneiss in the lower portion of the LPSZ. The abundance of leucogranites gradually decreases toward the southern margin of the LPD, and terminates to the south where lower grade rocks in the hanging wall of the LPSZ contain no leucogranites (Langille et al. 2012; Thiede et al. 2006). The individual intrusions are small in volume and extent, ranging from 5-cm- to 2-m-wide by 20-cm- to >100-m-long, and form a complex network of crosscutting bodies distinguishable by differences in mineralogy and chemistry. Leucogranites range from in-situ leucosomes hosted by migmatites to large bodies intruding non-migmatitic host rocks, and indicate variable melt transport distances of 0 to >100 m. Solid-state fabric development in the leucogranites ranges from moderately and weakly foliated to isotropic. The presence of deformed and undeformed granites suggests pre-, syn-, and post-kinematic emplacement with respect to the dominant tectonic fabric in the host gneiss. Deformed and undeformed leucogranites found within the LPSZ potentially provide minimum age constraints for movement along the LPSZ.

U-Pb monazite dates from metamorphic rocks of the GHS exposed in the Sutlej valley (Haimanta Group) indicate garnet growth from 34 to 30 Ma and continued monazite crystallization after the cessation of garnet growth at 30 to 27 Ma (Chambers et al. 2009). Thermobarometry and U-Th/Pb dating of monazite from Leo Pargil metapelites indicates conditions of garnet growth in the host rocks were 600-650°C and 6-8 kbar at ~30 Ma (Langille et al. 2012), consistent with data from the Haimanta Group south of the LPD (Chambers et al. 2009). Near-isothermal decompression of the LPSZ footwall rocks to 4 kbar occurred at a minimum rate of 1.3 mm/year and contributed to growth of metamorphic monazite until 23 Ma (Langille et al. 2012).

Leech (2008) reported 93 individual sensitive high-resolution ion microprobe (SHRIMP) zircon spot dates from eight unspecified leucogranite bodies within the Leo Pargil dome. From this dataset, analyses containing significant common lead (>2%) or high U concentrations (>4,000 ppm) yield old apparent ages and do not appear in the final discussion of the data (Leech 2008). The remaining 11 individual spot analyses representing seven leucogranites have U-Pb dates ranging from 27 to 19 Ma. Given the small dataset, lack of contextual information, and potential analytical issues identified, the appropriate interpretation of these analyses remains unclear and is strongly debated (Parrish, 2009; Searle and Phillips, 2009; Leech, 2009). Analytical issues aside, zircon ages may reflect 1) an actual spread in crystallization ages, or 2) a combination of magmatic crystallization and incorporation of inherited xenocrysts (Parrish, 2009).

Leucogranites sampled near the confluence of the Spiti and Sutlej rivers yield a garnet-whole rock Sm-Nd age of 18.8 ± 0.7 Ma, muscovite-whole rock Rb-Sr ages ranging from 19.7 to 17.2 Ma, and biotite-whole rock Rb-Sr ages ranging from 16.4 to 11.6 Ma and are interpreted to represent the final stage of crystallization and cooling (Thöni et al. 2012). ^{40}Ar/^{39}Ar mica ages constrain the moderate-temperature (300-450°C) thermal history of the dome, and suggest rapid cooling between 17 and 14 Ma throughout the dome, whereas apatite fission track (AFT) ages indicate the cessation of ductile movement along the LPSZ by 10 Ma and a transition to brittle normal faults (Hintersberger et al. 2010; Thiede et al. 2006).

2.3 Samples and Methods

In contrast to highly refractory zircon, monazite is more reactive in minimum-temperature melts and records new growth during leucogranite crystallization. Monazite U-Th/Pb geochronology has been successfully employed to date granites throughout the Himalaya (Harrison et al. 1999; Copeland et al. 1988, 1990; Parrish, 1990; Edwards and Harrison, 1997; Deniel et al. 1987; Simpson et al. 2000; Lee et al. 2004; Zhang et al. 2004; Cottle et al. 2007; Schärer, 1984; King et al. 2010; Cottle, Searle, et al. 2009; Cottle, Jessup, et al. 2009; Viskupic et al. 2005). Additionally, previous studies have linked trace element distributions in monazite to the chemical conditions present at the time of crystallization (Zhu and O'Nions, 1999; Stepanov et al. 2012; Williams et al. 2007, 1999; Cocherie et al. 1998; Kohn et al. 2005; Corrie and Kohn, 2008).

This study integrates LA-ICPMS U-Th/Pb monazite geochronology and geochemistry with field observations within the existing geologic context of the LPD. In order to obtain and interpret geochronologic data while preserving its context, samples were selected according to three specific criteria at a variety of scales: 1) km-scale spatial distribution and structural position; 2) m-scale outcrop relations; and 3) µm-scale mineral characteristics. The goal of this sampling strategy is to characterize the melting history of the dome with respect to structural position, deformation and chemical composition.

Nineteen granite samples were collected from eight different localities within the LPD (Table 2.1) including three outcrops within the upper LPSZ (locations 1, 2, and 3), four outcrops within the lower LPSZ (locations 4, 5, 6, and 7), and one outcrop within the migmatitic core of the LPD (location 8). Sampling was targeted to define, as well as possible given terrain constraints, a traverse across the LPD from shallower to deeper structural positions (Fig. 2.1b). Crosscutting relations, the degree of fabric development, and the orientation of the intrusive bodies relative to the metamorphic foliation(s) were documented (Fig. 2.2). Leucogranites range from medium- to very coarse-grained (3-10 mm) and share a peraluminous composition containing K-feldspar + plagioclase + quartz + muscovite ± tourmaline ± biotite ± garnet. Accessory phases include apatite, zircon, monazite, and occasional xenotime or intergrowths of zircon and xenotime. Monazite separates for each sample were prepared using standard techniques including crushing, milling, sieving, and separation by density and magnetic susceptibility. LPD leucogranites typically contain approximately 0.01 to 0.02% modal abundance of monazite, yielding a few hundred monazite grains from a 2 to 3 kg leucogranite sample. Monazite grains were handpicked, mounted in a 2.5 cm epoxy resin discs, and polished to expose equatorial sections through the grains.

Prior to U-Th/Pb analysis, monazite grains were imaged using an FEI Quanta scanning electron microscope equipped with a back-scattered electron detector. After this initial screening process, monazite grains were selected for further imaging using a Cameca SX-100 electron probe micro-analyzer (EPMA) housed at the University of California, Santa Barbara. X-ray maps were produced using five wavelength-dispersive

Location	Sample	Mineralogy	Texture	Field Relations	Zoning patterns	Trace element chemistry (values in ppm)	Distribution	Age(s) Ma	MSWD
1 Upper LPSZ 31.873581°N	LP09-16	ms, tur, gt, bt	v. coarse	cuts foliation, cuts 17	oscillatory, sector	Eu <150; Yb >60; U >15,000; Th/U <5	discrete	19.9 ± 0.1	0.6
78.604311°E 3020 m	LP09-17	ms, tur, bt	medium	cuts foliation	oscillatory	Eu >150; Yb <60; U <15,000; Th/U >5	single	21.5 ± 0.2	0.3
2 Upper LPSZ 31.911515°N	LP09-69	ms, tur, gt	medium	foliation parallel, boudinaged	sector	Y = 8,000-16,000; Eu <100; Yb >60; U >10,000, Th/U <7	single	26.2 ± 0.2	0.3
78.624264°R 3750 m	LP09-70	ms, bt	medium	cuts foliation, fault parallel	core/mantle/rim	Y >8000 (core); Y = 5,000-7,000 (mantle); Y >7000 (rim); Eu >100; Yb <60; U <15,000; Th/U >5	discrete	19.6 ± 0.1	0.3
3 Upper LPSZ 31.942396°N	LP09-73	ms, tur, gt	coarse	foliation parallel, folded	sector, core/rim	Nd <29,000; Th >100,000; U >20,000 (core); U <7,000 (rim)	single	29.0 ± 0.2	0.7
78.602511°E 3430 m	LP09-74	ms, tur, gt	v. coarse	cuts foliation	sector, core/rim	Nd >29,000; Th <90,000; U >30,000 (core); U <7,000 (rim)	discrete	23.7 ± 0.3 21.8 ± 0.4	0.2 0.1
4 Lower LPSZ 31.801421°N	LP09-153	ms, tur, gt	fine	cuts foliation	patchy, irregular	Eu >150; Yb <40	discrete	19.1 ± 0.3	1.2
78.641218°E 2575 m	LP09-154	ms, tur, gt	medium	foliation parallel, folded	patchy, irregular	Eu <50; Yb >40	continuous	22.1 ± 0.3	1.4
5 Lower LPSZ 31.808369°N	LP09-157	ms, tur, gt	medium	massive	oscillatory, core/rim	Y >10,000 (rim); Y <10,000 (core); Eu >100; U = 4,000-15,000	continuous	19.0 ± 0.3	0.3
78.640606°E 2625 m	LP09-158	ms, tur	v. coarse	cut by 157	patchy, core/rim	high-Th cores; low-Th rims; U = 18,000-65,000; Th/U = 1-3	continuous	20.2 ± 0.2	0.9
	LP09-166	ms, tur, gt	coarse	cuts 157	oscillatory	Eu <30; U = 18,000-55,000; Th/U = 1-3	single	18.6 ± 0.1	0.6
	LP09-167	ms, tur, gt	medium	same as 157	oscillatory, core/rim	Eu >150; U = 5,000-20,000	continuous	19.0 ± 0.2	1.2
6 Lower LPSZ 31.811423°N 78.637137°E 2615 m	LP09-168	ms, tur, gt, bt	medium	massive	patchy, core/rim	m008 and m096: Y >12,000; Eu >200; Th <46,000; Th/U = 2-4 m091 and m088 core: Y = 5,000-11,000; Eu <150; Th = 60,000-100,000; Th/U = 7-13 m021 and m088 rim: Y = 8,500-12,000; Eu = 150-200; Th = 48,000-60,000; Th/U = 5-10	discrete	23.9 ± 0.2 21.6 ± 0.2 19.2 ± 0.2	0.2 0.3 1
	LP09-169	ms, tur, gt	coarse	massive	patchy, core/rim	Y = 8,000-18,000; Th = 50,000-100,000; U = 10,000-35,000	continuous	20.1 ± 0.3	1.4
	LP09-171	ms, tur, gt	coarse	cuts foliation	patchy, core/rim	Y <10,000; Eu <100; Yb <10; Th >100,000; U >30,000 (core); U <10,000 (rim)	continuous	19.3 ± 0.2	1.1
	LP09-172	ms, tur, bt	medium	foliation parallel, boudinaged	oscillatory	Y = 9,000-13,000; Eu = 140-240; Th = 35,000-75,000; U = 12,000-25,000	single	21.7 ± 0.2	1.1
7 Lower LPSZ 31.833704°N	LP09-173	ms	coarse	foliation parallel, folded	core/rim	m001and m015: Y <2,000; Eu <50; Dy <1000; Er <25; Yb <10; Th >100,000 m002, m003, and m014: Y = 8,000-12,000; Eu >100; Dy >2000; Er >170; Yb >15; Th >100,000	discrete	20.7 ± 0.2	0.3
78.632215°E 2970 m	LP09-174	ms, tur, bt	medium	cuts foliation	patchy, core/rim	Y <10,000 (core); Y >10,000 (rim); Th = 30,000-80,000;	discrete	22.9 ± 0.2 19.6 ± 0.2	0.9 1.8
8 Core 31.845213°N 78.690359°E 3425 m	LP09-179	ms, tur, gt	medium	cuts foliation	oscillatory	Eu <20; U = 20,000-50,000	single	17.9 ± 0.1	0.9

Table 2.1 Summary of sample locations, descriptions, trace element chemistry, and Th-Pb ages; ms, muscovite; tur, tourmaline; gt, garnet; bt, biotite; LPSZ = Leo Pargil Shear Zone.

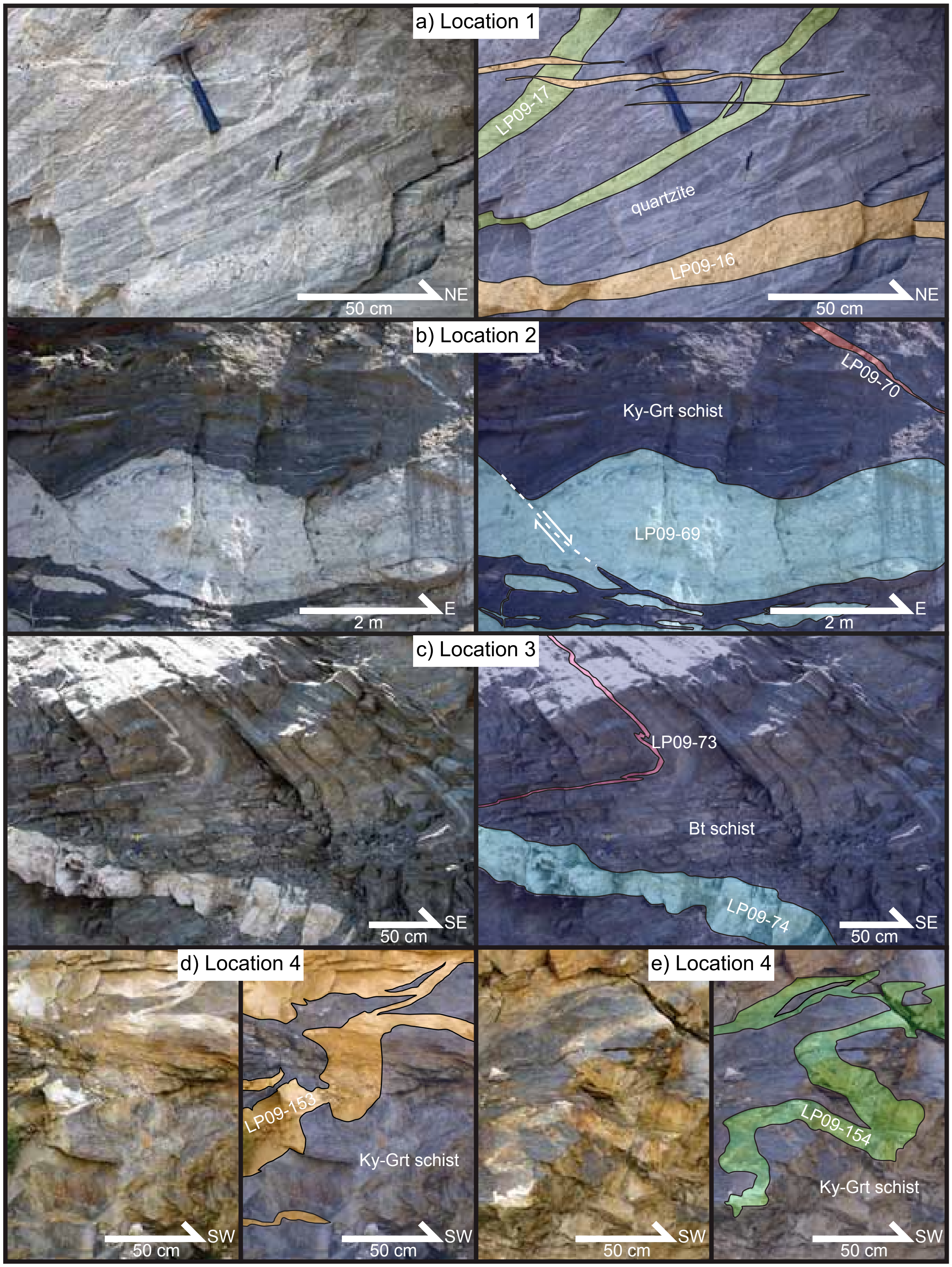

Figure 2.2 Outcrop photographs of sample locations; mineral abbreviations from Whitney and Evans (2010). a) Quartzite intruded by an early, foliated leucogranite (LP09-17) and cut by a later coarse-grained leucogranite (LP09-16). b) Kyanite-garnet schist intruded by a thick, boudinaged leucogranite (LP09-69) and cut by a thin leucogranite dike (LP09-70). The orientation of the thin dike coincides with a ductile normal fault in the boudinaged sill. c) Biotite schist intruded by a thin, folded leucogranite (LP09-73) with one limb cut by a late leucogranite dike (LP09-74). d) Kyanite-garnet gneiss intruded by a undeformed leucogranite (LP09-153). e) Kyanite-garnet gneiss intruded by a folded leucogranite (LP09-154). Photograph taken approximately 5 m from LP09-153.

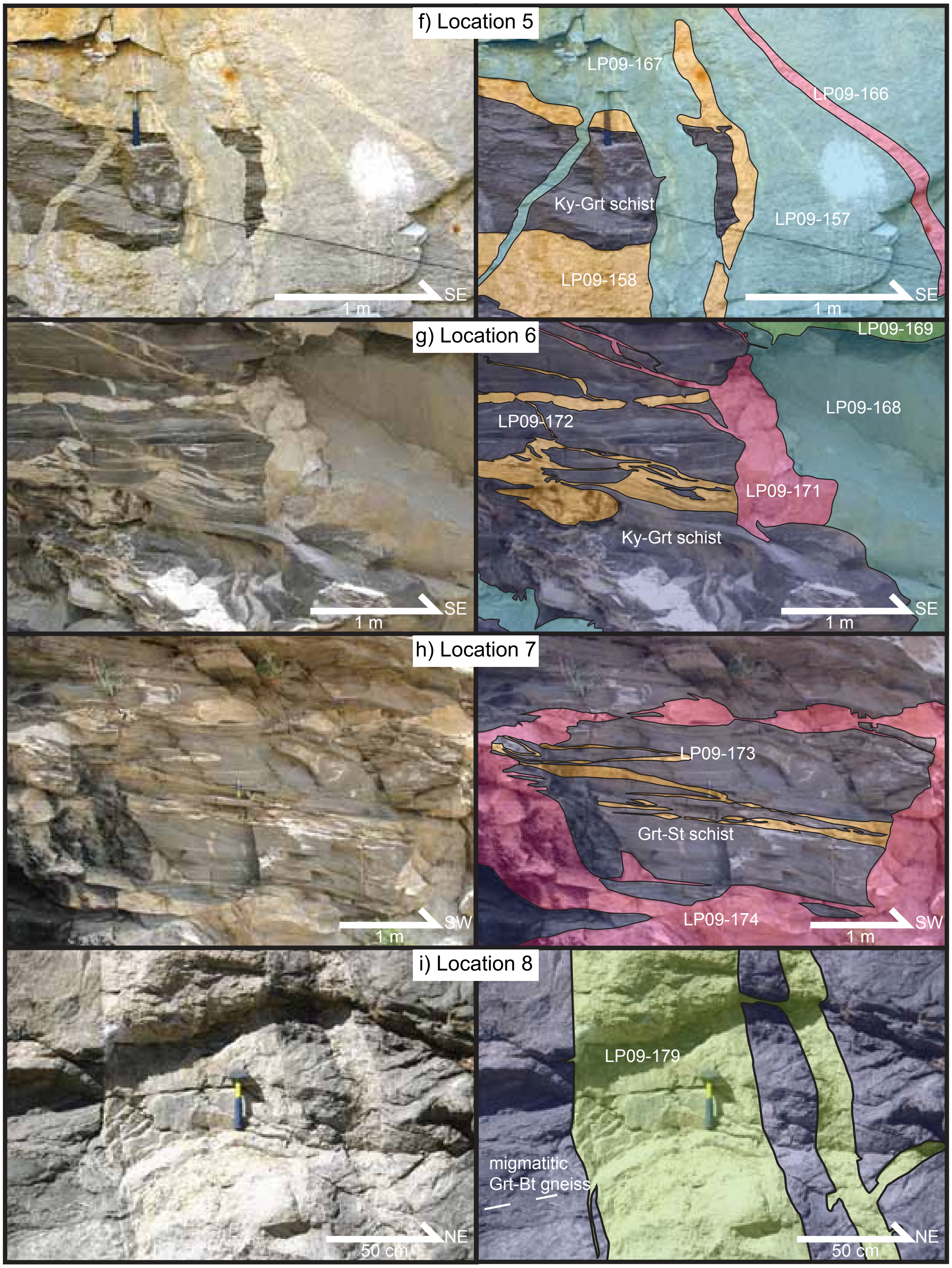

Figure 2.2 (continued) f) Kyanite-garnet gneiss intruded by three phases of leucogranite, including an early pegmatite (LP09-158), a medium-grained granite (LP09-157 and LP09-167) and a late pegmatite (LP09-166). g) Kyanite-garnet gneiss intruded by four generations of leucogranites (LP09-172, LP09-169, LP09-168, LP09-171). h) Garnet-staurolite gneiss intruded by a folded leucogranite sill (LP09-173) and cut by a leucogranite dike (LP09-174). i) Migmatitic garnet-biotite gneiss with segregations that can be traced into a leucogranite dike (LP09-179).

spectrometers positioned to measure Y (LTAP, Lα), La (LPET, Lα), Nd (PET, Lα), Th (LPET, Mα), and U (LPET, Mα).

U-Th/Pb analyses were carried out using a laser ablation multi-collector inductively coupled plasma mass spectrometer (LA-MC-ICPMS) at the University of California Santa Barbara (UCSB). Instrumentation consists of an Analyte 193 nm ArF excimer laser (Photon Machines, San Diego, USA) attached to a Nu Plasma HR MC-ICPMS (Nu Instruments, Wrexham, UK). (See Table 2.2, Appendix A; (Cottle et al. 2011; Kylander-Clark et al. 2013) for further analytical detail). After completion of U-Th/Pb analyses, trace element data were collected using the same laser system described above and a Nu Instruments AttoM single collector ICPMS. The AttoM was operated in Linked Scan mode to measure a range of masses, from ^{31}P to ^{174}Yb (Table 2.2).

Data reduction for U-Th/Pb and trace elements was carried out using Iolite v. 2.1.2 (Paton et al. 2010). 44069 monazite served as the primary reference material to monitor and correct for instrumental drift, mass bias, as well as Pb/U and Pb/Th down-hole fractionation while the remaining two reference materials were treated as unknowns in order to assess accuracy and precision within each run and session. Reported uncertainties on U-Th/Pb and trace element data incorporate an uncertainty component based on the reproducibility of the primary reference material over the analytical sessions. During the analytical period (1 continuous session over 72 hours), repeat analyses of 554 yield a weighted mean ^{208}Pb/^{232}Th date of 47.4 ± 1.8 Ma (n = 167 of 170). Repeat analyses of FC-1 yield a weighted mean ^{206}Pb/^{238}U age of 56.1 ± 0.9 (n = 178 of 184), and a weighted mean ^{208}Pb/^{232}Th age of 56.6 ± 1.0 Ma (n = 177 of 184).

Table 2.2 Analytical Parameters for LA-ICPMS

Analytical Parameters	U-Th-Pb	Trace Elements
Laser	193 ArF Excimer	193 ArF Excimer
Pit diameter	~7 µm	~6 µm
Repetition Rate	3 Hz	3 Hz
Shot count	120	90
Fluence	4.8 J/cm^2	3.2 J/cm^2
Laser energy	3 mJ	3 mJ
ICP-MS	Nu Plasma HR Multi-Collector	Nu AttoM Single-Collector
Secondary Electron Multipliers:		
IC0	^{204}X (^{204}Pb + ^{204}Hg)	^{31}P, ^{89}Y, ^{139}La, ^{140}Ce, ^{141}Pr, ^{146}Nd, ^{147}Sm, ^{153}Eu, ^{157}Gd, ^{163}Dy, ^{166}Er, ^{172}Yb,
IC1	^{206}Pb	
IC2	^{207}Pb	
IC3	^{208}Pb	
Faraday cups:		
Ex-H	^{238}U	
H2	^{232}Th	

2.4 Results

2.4.1 Field relations

Sample locations represent three structural positions (Fig. 2.1), including the upper LPSZ (locations 1, 2, and 3), the lower LPSZ (locations 4, 5, 6, and 7), and the migmatitic core of the LPD (location 8). Outcrop-scale observations at several locations suggest multiple generations of leucogranite emplacement (Fig. 2.2). The mineralogy, textures, and field relations used to identify and describe each leucogranite body are reported here and summarized in Table 2.1. Due to their restricted extent, variability in mineralogy, textures, thickness, orientation, and degree of deformation, generations of leucogranites between different locations have not been correlated. Rather, each outcrop is considered individually based on field relations and structural position within the dome.

2.4.1.1 Location 1

Location 1 consists of quartzite with a well-defined foliation dipping moderately to the southwest (295/35 SW) cut by two generations of leucogranite dikes (Fig. 2.2a). Representative of the earlier set of dikes, LP09-17 is a 10- to 15-cm-wide dike of medium-grained, muscovite-biotite-tourmaline granite with a weak macroscopic foliation discordant to the granite-quartzite contact and the host rock foliation. The later set of dikes, represented by LP09-16, cut the host rock and LP09-17 and consists of texturally identical 2- to 10-cm-wide bodies of very coarse-grained to pegmatitic granite with muscovite, biotite, garnet, and 1-cm-long fractured tourmaline. LP09-16 appears isotropic and the contact is discordant to the foliation in the host quartzite. Furthermore, the contact between LP09-17 and the host rock is more parallel to the foliation than the contact between LP09-16 and the host rock.

2.4.1.2 Location 2

This outcrop exposes garnet-biotite schist intruded by a 2-m-thick, foliation-parallel, boudinaged sill (LP09-69) consisting of a medium-grained muscovite-tourmaline-garnet leucogranite (Fig. 2.2b) The host rock and sill are cut by a mesoscopic ductile shear band with top-to-the-east shear sense and a 10-cm-wide, fine-to-medium-grained, muscovite-biotite leucogranite dike (LP09-70) oriented parallel to the shear band. An east-west oriented road cut provides exposure perpendicular to the local stretching lineation in the schist. Extensional shear bands that record top-to-the-east displacement could record flattening that occurred normal to the shear plane. The orientation of LP09-70 parallel to the shear band suggests intrusion of LP09-70 and shearing occurred under a similar kinematic setting.

2.4.1.3 Location 3

Located within the upper portion of the LPSZ, this outcrop consists of kyanite-garnet schist intruded by two generations of muscovite-tourmaline-garnet leucogranites (Fig. 2.2c). LP09-73 is a thin, 5-cm-wide sill oriented parallel to foliation in the host gneiss and has been folded and boudinaged. The sill is coarse-grained, white in color, and contains abundant muscovite, minor garnet, and abundant tourmaline near the margins where it has reacted with the host rock. LP09-74 is a very coarse-grained leucogranite with abundant muscovite and 1- to 2-mm-long tourmaline concentrated in 1-cm-wide pods. LP09-74 cuts the host rock foliation and LP09-73; it also cuts the fold, although not visible in the photograph (Fig. 2.2c). No fabric development was observed, but the thickness of the dike changes suggesting some deformation post-emplacement.

2.4.1.4 Location 4

This outcrop consists of two leucogranites (LP09-153 and LP09-154) from a deeper structural position in the LPSZ (Fig. 2.1b). The host kyanite-garnet schist is cut by two generations of 10-cm-thick muscovite-tourmaline-garnet leucogranite dikes (Figs. 2.2d, 2.2e). LP09-154 is medium-grained, intruded parallel to the foliation, and was subsequently folded. LP09-153 is fine-grained and cuts the host rock foliation.

2.4.1.5 Location 5

This outcrop consists of kyanite-garnet schist intruded by three generations of leucogranite dikes (Fig. 2.2f). The first generation consists of coarse-grained (3-10 mm) pegmatite with large (2-mm-wide) elongate tourmaline, books of muscovite, no macroscopic foliation, and undeformed margins and is represented by LP09-158. The second intrusion cuts the first generation and the host rock and consists of a medium grained (<3 mm) white to grey garnet-tourmaline granite. Two samples from this body were collected: LP09-157 represents the light-colored portion of the body, while LP09-167 represents the medium-grey portion. The contact between the two is gradational, with no discernable differences in mineralogy or grain size. The two nearly identical samples from the same leucogranite body provide a test of methods and sampling strategy by examining the reproducibility of age distributions within a leucogranite body. The third generation of leucogranite in the outcrop, represented by LP09-166, cuts the second generation and consists of coarse grained (<1.5 cm) undeformed pegmatite with garnet, books of muscovite, and elongate 3-mm-wide tourmaline fractured perpendicular to the long-axis. Langille et al. (2012) present ages for samples LP09-157, LP09-158, LP09-166, and LP09-167 from this location. This study present new data that incorporates x-ray imaging and trace element analysis to further understand the processes of crystallization and partial melting recorded by these leucogranites.

2.4.1.6 Location 6

This location consists of kyanite-garnet schist intruded by four generations of leucogranites (Fig. 2.2g). The earliest body (LP09-172) consists of medium-grained muscovite-tourmaline-biotite granite that forms 15-cm-thick boudins parallel to foliation developed in the host schist. The schist and LP09-172 are cut by a coarse-grained muscovite-tourmaline-garnet leucogranite (LP09-169); a medium-grained, muscovite-tourmaline-garnet-biotite granite (LP09-168); and a tourmaline-rich leucogranite (LP09-171).

2.4.1.7 Location 7

Exposed in the lower portion of the LPSZ, two generations of leucogranite intrude garnet-staurolite schist (Figs. 2.2h). The first generation of leucogranite, represented by LP09-173**,** consists of a muscovite-bearing, 10-cm-wide, foliation-parallel sill isoclinally folded along with the host gneiss. The second generation of leucogranite, LP09-174, consists of coarse-grained, muscovite-tourmaline-biotite granite that cuts the host rock and LP09-173.

2.4.1.8 Location 8

LP09-179 is a medium-grained muscovite-tourmaline-garnet leucogranite from the migmatitic core of the Leo Pargil dome (Fig. 2.1b). The 75-cm-wide vertical dike cuts the gently dipping foliation in the migmatitic garnet-biotite gneiss and leucosome segregations can be traced from the host rock into the dike (Fig. 2.2i).

2.4.2 Monazite trace element chemistry and U-Th/Pb geochronology

Isotopic ratios and calculated ages are summarized in Fig. 2.3. Low concentrations of radiogenic ^{207}Pb relative to background and/or common Pb in young monazite produce imprecise ^{207}Pb/^{235}U dates by in-situ methods. Additionally, the preferential incorporation of initial ^{230}Th by monazite results in excess ^{206}Pb (Schärer, 1984), thereby making apparent ^{206}Pb/^{238}U dates too old relative to ^{208}Pb/^{232}Th dates by as much as 50% in Himalayan leucogranites (Cottle, Searle, et al. 2009). Therefore, ^{208}Pb/^{232}Th dates are utilized in this study (Fig. 2.3). Analyses with resolvable common Pb were identified by >150 cps of ^{204}Pb and/or ^{207}Pb/^{206}Pb ratios >0.165 and are excluded from Fig. 2.3. Trace element analyses are summarized in Fig. 2.4.

2.4.2.1 Location 1

X-ray maps of monazite from both leucogranite samples reveal typical igneous textures including oscillatory and sector zoning (Fig. 2.5). Monazite grains from LP09-16

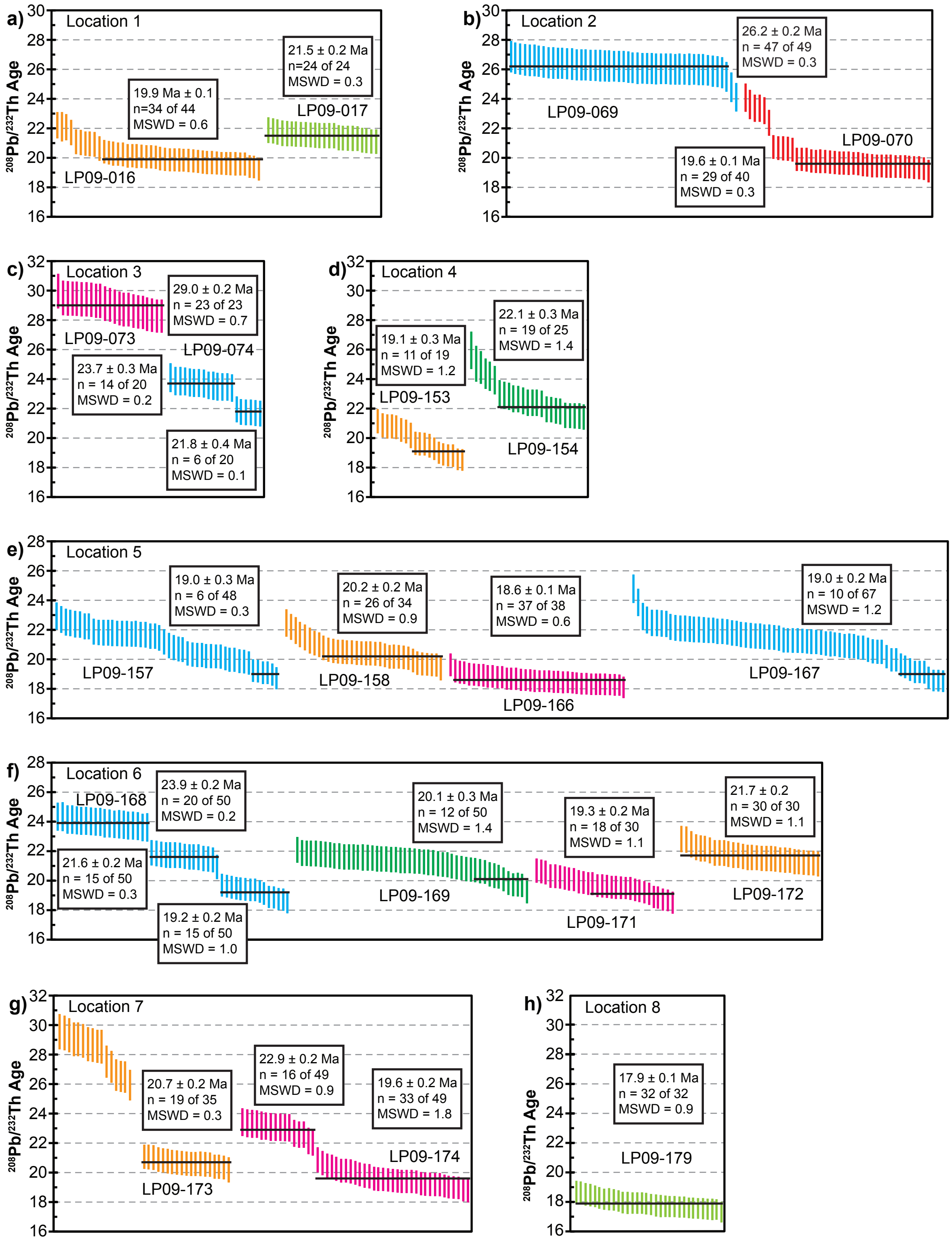

Figure 2.3 Weighted mean plots of ^{208}Pb/^{232}Th ages for all samples grouped by location. Data points are ordered by age with each horizontal black line indicating the weighted mean age for the population of data points it intersects. Colors are consistent with outcrop photographs in Fig. 2.2.

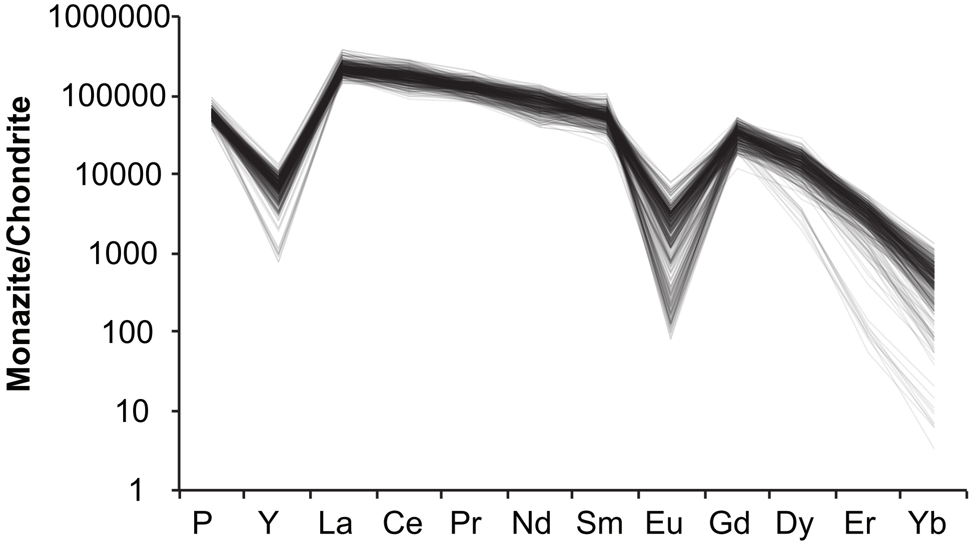

Figure 2.4 All Leo Pargil trace element data (n = 426) normalized to chondrite (McDonough and Sun, 1995); grey lines represents individual analyses, and black areas result from superimposing several analyses. Note that all analyses exhibit a pronounced negative Eu anomaly.

share a similar composition, with the exception of one grain (m052), which appears more similar to those of LP09-17 (Fig. 2.5a-b).

The earlier dike, LP09-17, yields a single population weighted mean age of 21.5 ± 0.2 (MSWD 0.3; Fig. 2.3a). The later dike, LP09-16, consists of two age populations: the larger population (n = 34) yields a weighted mean age of 19.9 ± 0.1 Ma (MSWD 0.6; Fig. 2.3a), whereas the other population (n = 10) consists of older ages between 20.6 ± 0.8 and 22.2 ± 0.9 Ma measured from grain m052 (Fig. 2.5c).

2.4.2.2 Location 2

Monazite grains from LP09-69 are fairly homogeneous in composition and exhibit sector zoning with moderate to high Y content (8,000 to 16,000 ppm), Eu <100 ppm, Yb >60 ppm, U >10,000 ppm, and Th/U ratios <7 (Fig. 2.6a-b). LP09-70 contains monazite with Eu >100 ppm, Yb <60 ppm, U <15,000 ppm, and Th/U ratios >5. In general, Y concentration is heterogeneous and varies from Y-rich (>8,000 ppm) cores, Y-poor (5,000-7,000 ppm) mantles, and Y-rich (>7,000 ppm) outer rims, although a very Y-poor (<3500 ppm) core in grain m022 represents an exception.

Ages from the boudinaged sill, LP09-69, define a homogeneous population with a weighted mean age of 26.2 ± 0.2 Ma (MSWD 0.3; Fig. 2.3b), however, two analyses from the high-U (>15,000 ppm) rim of grain m045 yield slightly younger dates of 24.1 to 24.8 Ma and are not included in the weighted mean age (Fig. 2.6). Ages from LP09-70, the cross-cutting dike, define a peak at 19.6 ± 0.1 Ma (MSWD 0.3; Fig. 2.3b), but older dates ranging from 24.1 ± 1.0 Ma to 20.6 ± 0.8 Ma are measured in the cores of grains m022 and m002 (Fig. 2.6c).

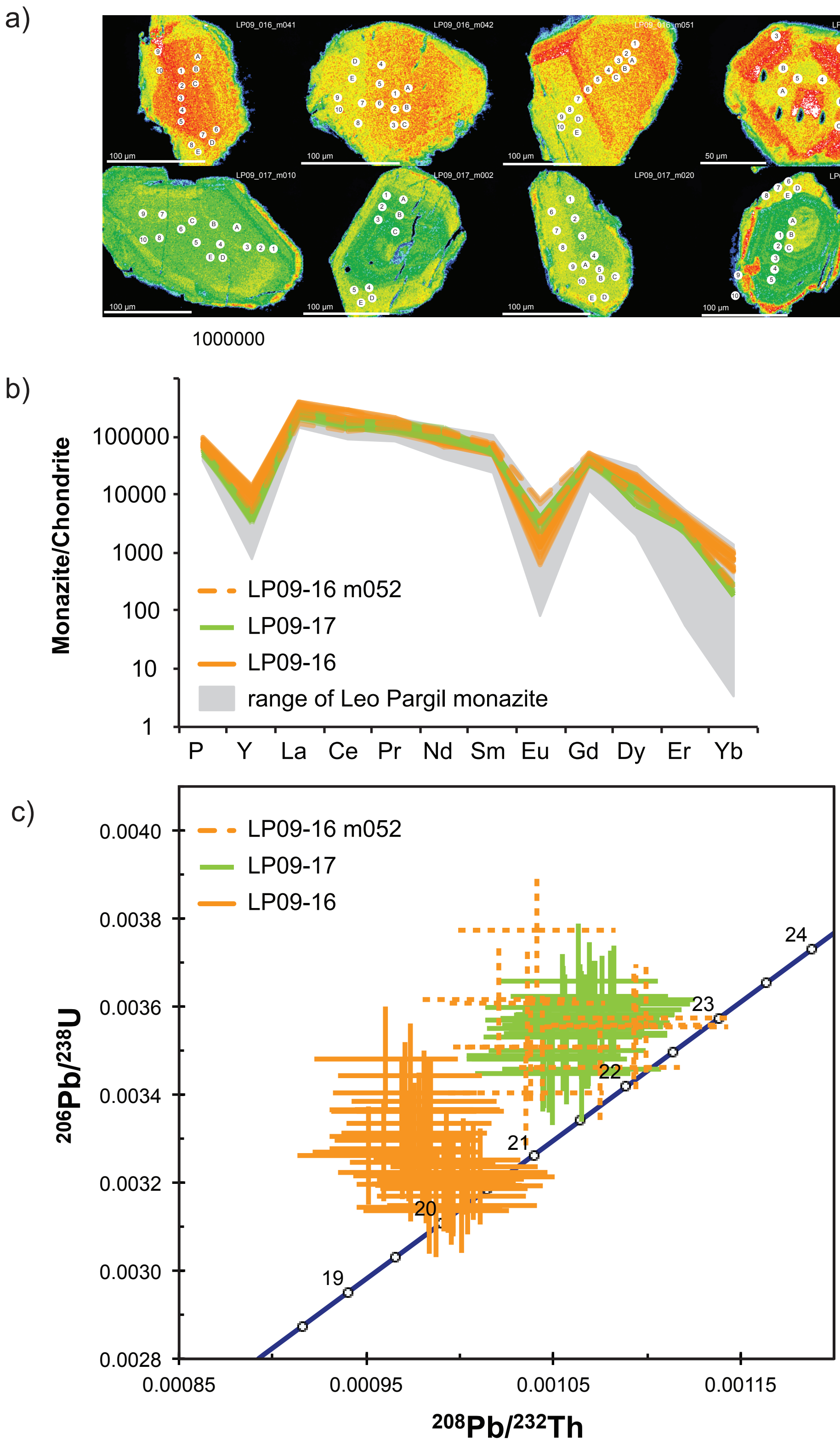

Figure 2.5 Geochronology and trace element results of LP09-16 and LP09-17. a) X-ray maps of Y; warmer colors indicate higher concentration of Y. b) Trace element diagrams of grains with different Y concentration. c) Concordia diagram with 208Pb/232Th ratio on the x-axis. Note that monazite grain m052 from LP09-16 is similar in appearance, chemistry, and age to LP09-17, except for the presence of a thin high-Y rim.

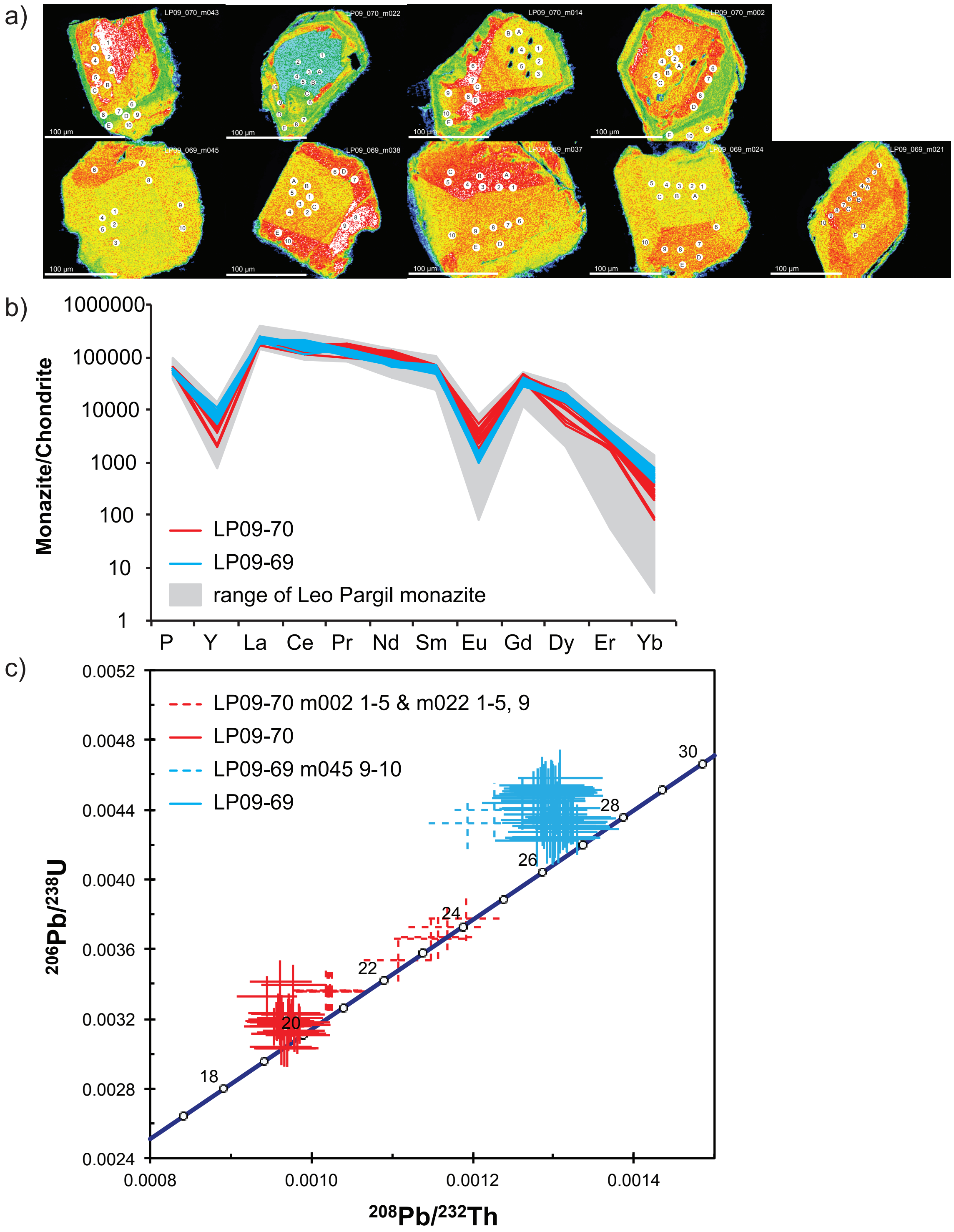

Figure 2.6 Geochronology and trace element results of LP09-69 and LP09-70. a) X-ray maps of Y; warmer colors indicate higher concentration of Y. b) Trace element diagrams of grains with different Y concentrations. c) Concordia diagram with ^{208}Pb/^{232}Th ratio on the x-axis.

2.4.2.3 Location 3

Monazites from LP09-73 exhibit sector zoning and have lower Nd (<29,000 ppm) and higher Th (>100,000 ppm) concentrations compared to other samples. Two grains (m008 and m030) have embayed high-U (>20,000 ppm) cores overgrown by low-U (<7,000 ppm) rims. Of the two grains recovered from LP09-74, m010 exhibits sector zoning, whereas m011 consists of an embayed high-U (>30,000 ppm) core in sharp contact with a low-U (<7,000 ppm) rim. Both grains have lower Th (<90,000 ppm) and higher Nd (>29,000 ppm) than LP09-73.

Ages from the folded sill, LP09-73, define a single population of 29.0 ± 0.2 Ma (MSWD 0.7; Fig. 2.3c). The cross-cutting dike, LP09-74, yields two age populations: high-U (>20,000 ppm) cores yield a weighted mean age of 23.7 Ma ± 0.3 (MSWD 0.2), whereas a low-U (<7,000 ppm) zone yields a weighted mean age of 21.8 ± 0.4 Ma (MSWD 0.1). Core ages are consistent with field relations and indicate folding occurred between the emplacement of LP09-73 at ~29 Ma and the emplacement of LP09-74 at 23.7 Ma.

2.4.2.4 Location 4

Maps of four grains from LP09-153 reveal patchy irregular zoning in Y, Th, and U; trace element analysis of the largest grain (m001) indicates high Eu (>150 ppm) and low Yb (<40 ppm). By comparison, LP09-154 monazites have Eu <50 ppm, Yb >40 ppm, and exhibit heterogeneous zoning in Y, Th, and U.

Dates from the folded granite, LP09-154, range from 25.9 to 21.4 Ma and yield a weighted mean age of 22.1 ± 0.3 Ma (MSWD 1.4; Fig. 2.3d). The cross-cutting dike, LP09-153, consists of two populations: older dates range from 21.1 to 20.2 Ma and younger dates define a weighted mean age of 19.3 ± 0.3 Ma (MSWD 1.2, Fig. 2.3d).

2.4.2.5 Location 5

LP09-157 monazites have Eu >100 ppm, U ranging from 4,000 to 15,000 ppm, and display heterogeneous Th and Y zoning where high-Y (>10,000 ppm) rims enclose relict low-Y (<10,000 ppm) cores. LP09-167 monazites have similar Th and Y zoning patterns as LP09-157, high Eu (>150 ppm) and heterogeneous U concentrations ranging from 5,000 to 25,000 ppm. Monazite grains from LP09-158 have very high U (18,000-65,000 ppm), low Th/U ratios (1-3), and high-Th cores enveloped by low-Th rims. LP09-166 monazites exhibit oscillatory Y zoning and have high U (18,000-55,000 ppm), low Eu (<30 ppm), and low Th/U ratios ranging from 1 to 3.

Dates from LP09-158, the first generation leucogranite, range from 22.5 to 19.3 Ma and yield a weighted mean age of 20.2 ± 0.2 Ma (MSWD 0.9; Fig. 2.3e). Two samples, LP09-157 and LP09-167, represent the second generation of leucogranite. Dates from LP09-157 range from 22.9 to 18.7 Ma with a broad plateau at ~22 Ma, and the youngest analyses define a weighted mean age of 19.0 ± 0.3 Ma (MSWD 0.3; Fig. 2.3e). Similarly, LP09-167 dates range from 24.8 to 18.5 Ma and consist of two main components: 22 Ma cores and younger rims that define a weighted mean age of 19.0 ± 0.2 Ma (MSWD 1.2; Fig. 2.3e). The third generation of granite, represented by LP09-166, yields a single population with a weighted mean age of 18.6 ± 0.1 Ma (MSWD 0.6; Fig. 2.3e).

Weighted mean ages calculated using the youngest set of analyses for each leucogranite body are consistent with the outcrop relations. The two samples of the same body (LP09-157 and LP09-167) are indistinguishable in both age distribution and weighted mean age of the youngest single population.

2.4.2.6 Location 6

LP09-168 consists of three distinct chemical compositions of monazite: 1) grains m096 and m008 have high Y (>12,000 ppm), high Eu (>200 ppm), low Th (<46,000 ppm), and low Th/U ratios ranging from 2-4; 2) grain m091 and the core of grain m088 have low Y (5,000-11,000 ppm), low Eu (<150 ppm), high Th (60,000-100,000 ppm), and Th/U ratios ranging from 7-13; and 3) grain m021 and the rim of grain m088 have intermediate Y (8,500-12,000 ppm), Eu (150-200 ppm), Th (48,000-60,000 ppm), and Th/U ratios ranging from 5-10 (Fig. 2.7a-b). X-ray maps of LP09-169 reveal heterogeneous patchy zoning with broad ranges in U (10,000-35,000 ppm), Th (50,000-100,000 ppm), and Y (8,000-18,000 ppm) content. LP09-171 monazites exhibit high-Th cores and low-Th rims, a broad range in Th (20,000-100,000 ppm) and U (7,500-45,000 ppm), and low Y (<10,000 ppm) and Eu (<100 ppm). LP09-172 monazites exhibit oscillatory zoning in U and fairly homogenous chemistry.

The earliest of the four generations of granite intrusions, LP09-172, yields a single population with a weighted mean age of 21.7 ± 0.2 Ma (MSWD 1.1; Fig. 2.3f). The second generation, represented by LP09-169, yields a broad age distribution from 22.1 to 19.2 Ma, with the youngest set of analyses defining a weighted mean age of 20.1 ± 0.3 (MSWD 1.4; Fig. 2.3f). Dates from LP09-171 range from 20.7 to 18.5 Ma, and the youngest set of analyses yield a weighted mean age of 19.3 ± 0.2 Ma (MSWD 1.1; Fig. 2.3f).

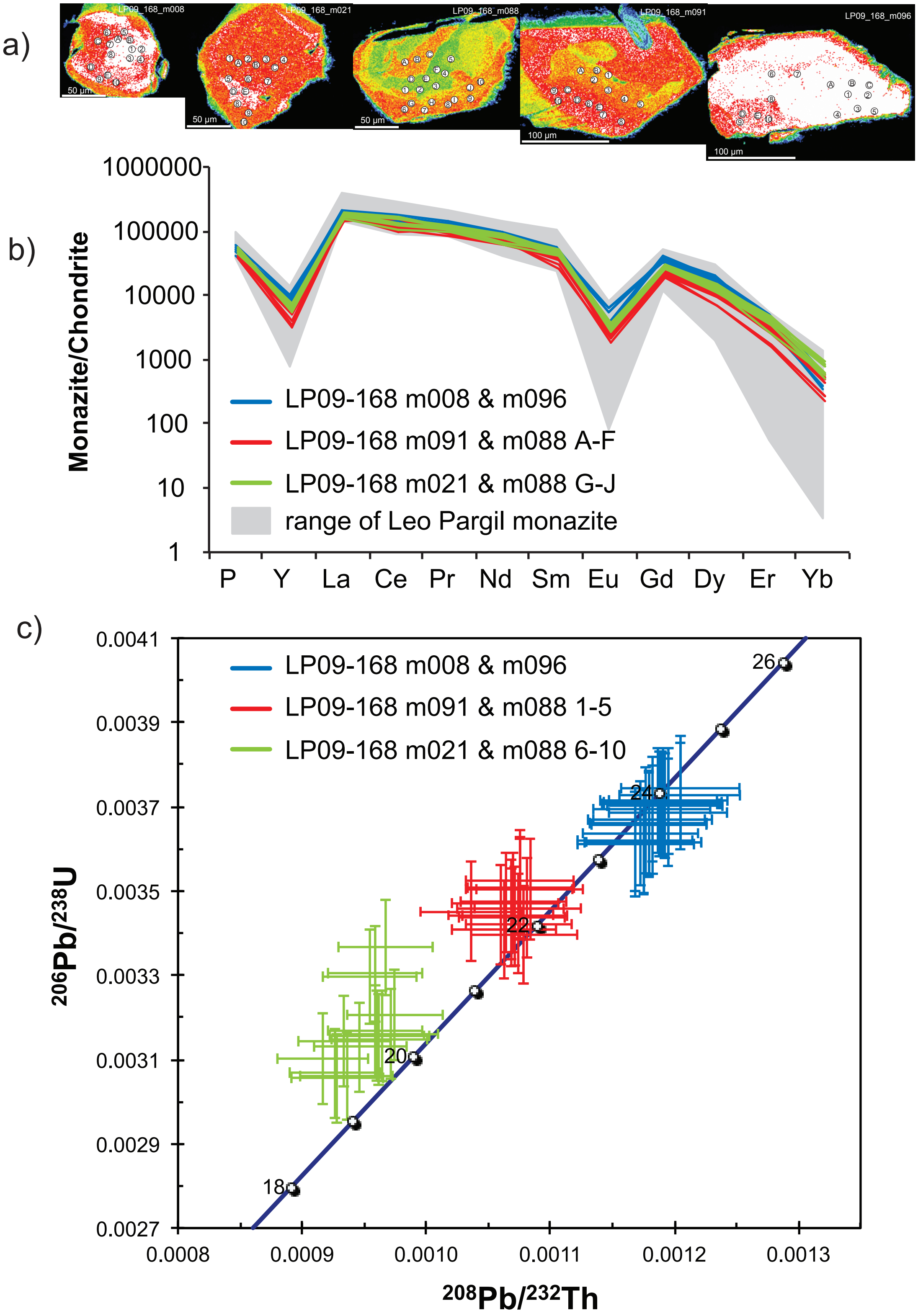

Figure 2.7 Geochronology and trace element results of LP09-168. a) X-ray maps; warmer colors indicate higher concentration of Y. b) Trace element diagrams of grains and domains with different Y concentrations. c) Concordia diagram with $^{208}Pb/^{232}Th$ ratio on the x-axis.

LP09-168 consists of three discrete age populations (Figs. 2.3f, 2.7c). Two grains, m008 and m096, yield a weighted mean age of 23.9 ± 0.2 (MSWD 0.2). Analyses of grain m091 and the core of grain m088 define a weighted mean age of 21.6 ± 0.2 (MSWD 0.3). Analyses of grain m021 and the rim of grain m088 yield a weighted mean age of 19.2 ± 0.2 (MSWD 1.0). The youngest set of analyses for each leucogranite body yield weighted mean ages consistent with the outcrop relations. Interestingly, The youngest body (LP09-168) also contains the oldest population of monazite, distinct in both chemistry and age from any other monazite populations observed from this location.

2.4.2.7 Location 7

LP09-173 monazites consist of two compositions: grains m001 and m015 have very low Y (<2,000 ppm), Eu (<50 ppm), Dy (<1,000 ppm), Er (<50 ppm) and Yb (<10 ppm) content, whereas grains m002, m003, and m014 have high Y (8,000-12,000 ppm), Eu (>100 ppm) and HREE content. Grain m015 exhibits a high-U (>30,000 ppm) core and a low-U (<10,000 ppm) rim. All grains contain Th >100,000 ppm. LP09-174 monazites contain high-Y rims enclosing low-Y cores and heterogeneous compositions with broad ranges in U (4,000-40,000 ppm), Th (30,000-80,000 ppm), and Th/U ratio (1-10).

For LP09-173, analyses of low-Y grains (m001 and m015) range from 29.6 to 25.9 Ma, whereas analyses of high-Y grains (m003 and m014) yield a weighted mean age of 20.7 ± 0.2 Ma (MSWD 0.3; Fig. 2.3g). Grain m002 yields dates from each of the two populations. LP09-174 also consists of two age populations: core analyses yield a weighted mean age of 22.9 ± 0.2 Ma (MSWD 0.9) while the rim analyses define a weighted mean age of 19.6 ± 0.2 Ma (MSWD 1.8, Fig. 2.3g).

2.4.2.8 Location 8

LP09-179 monazite grains exhibit oscillatory zoning in Y, Th, and U and have very high U (20,000-50,000 ppm) concentrations as well as a pronounced negative Eu (<20 ppm) anomaly. Several spot analyses of LP09-179 contain common Pb, and this is the only sample in which a significant amount of common lead is observed. Rejecting U-Th/Pb analyses with high $^{207}Pb/^{206}Pb$ ratios (>0.065) yields a single weighted mean age of 17.9 ± 0.1 Ma (MSWD = 0.9; Fig. 2.3h).

2.4.3 Summary of results

Ages of leucogranite bodies define broad textural and spatial trends. The age distribution of leucogranites spans from 30 to 18 Ma with a large proportion of dates between 23 and 19 Ma (Fig. 2.8a). The oldest leucogranite body (LP09-73) is a thin sill from a shallower structural position in the dome whereas the youngest sample (LP09-179) is from the migmatitic core of the dome. Three types of age distribution patterns are observed within individual leucogranites: single, discrete, and continuous. Leucogranites with a single age population contain monazite grains that are homogeneous in composition and/or exhibit concentric oscillatory zoning, and have only one age domain (e.g. LP09-17, LP09-69, LP09-73, LP09-166, LP09-172, and LP09-179). Leucogranites with discrete age components separated by time-gaps contain monazite with inter-grain and/or intra-grain variation in trace element chemistry (e.g. LP09-16, LP09-70, LP09-74, LP09-153, LP09-168, LP09-173, and LP09-174). Continuous age distributions consist of broad ranges of overlapping ages and exhibit heterogeneous variation in trace element

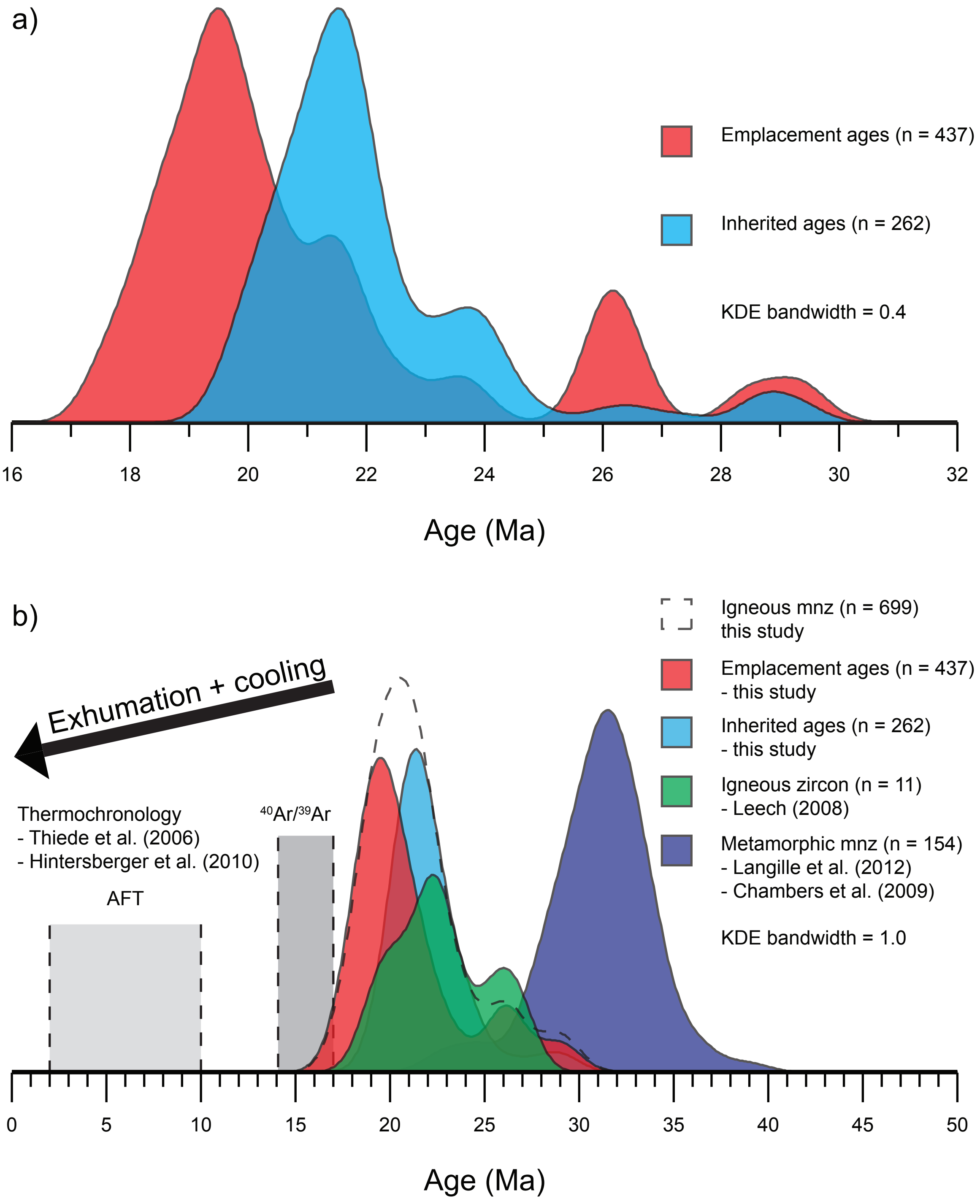

Figure 2.8 Summary of geochronologic and thermochronologic data from the Leo Pargil dome. a) Kernel Density Estimates (KDE; Vermeesch 2012) of ^{208}Pb/^{232}Th dates from this study; vertical axis units are arbitrary and represent relative % of each dataset. Inherited ages (blue) and emplacement ages (red) contribute to combined ages (dashed line). b) KDE of metamorphic monazite U-Th/Pb data (Chambers et al., 2009; Langille et al., 2012) in purple; KDE of zircon U/Pb data (Leech, 2008) in green; KDE of combined ^{208}Pb/^{232}Th dates from this study in orange; white mica ^{40}Ar/^{39}Ar data (Thiede et al., 2006; Hintersberger et al., 2010) shown as dark grey box; and apatite fission track (AFT) data (Thiede et al., 2006) plotted as light grey box.

chemistry (e.g. LP09-154, LP09-157, LP09-158, LP09-167, LP09-169, and LP09-171) In general, leucogranites from deeper structural positions (locations 4, 5, 6, and 7) yield broad age distributions whereas leucogranites from shallow structural positions (locations 1, 2, and 3) yield single or discrete age distributions (Figs. 2.2 and 2.3).

Three generalizations regarding the history of leucogranites in the LPD include: 1) early leucogranites (30-23 Ma) tend to be deformed along with the host rock whereas later intrusions (23-18 Ma) are less deformed and cut across host rock fabrics; 2) early leucogranites are small volume, thin bodies whereas later leucogranites are thick or massive; and 3) older leucogranites occur at shallower levels whereas younger leucogranites are more common at deeper structural levels. In addition to outcrop scale observations, key results from monazite chemical petrography include 1) leucogranites contain chemically heterogeneous populations of monazite grains; 2) individual monazite grains consist of distinct compositional domains, such as core/rim, sector, oscillatory, and patchy zoning; 3) distinct compositional domains on a single grain often yield different dates; and 4) grains with embayment textures provide evidence for dissolution of monazite.

2.5 Discussion

2.5.1 Age distribution patterns

Based on age distribution patterns, leucogranites from the Leo Pargil dome fall within two categories: 1) those that consist of a single, well-defined age population, indicated by an MSWD value approximately equal to 1; and 2) those characterized by excess scatter with an MSWD value much greater than 1 when all analyses of a given sample are included. Heterogeneous age distributions are either due to underestimation of individual data point uncertainty, or because the analyses actually represent more than one age population. Repeat analysis of secondary and tertiary reference materials consistently returns populations that are both accurate and have MSWD values of ~1 (see section 2), effectively ruling out underestimation of analytical uncertainty as the cause of the scatter. We therefore interpret the scatter as geologic rather than analytical in origin. The observed correlation between trace element compositions and age domains provides further support that heterogeneous age distributions reflect true geologic variation rather than analytical uncertainty and indicate that monazite within a single leucogranite crystallized at different times under different chemical conditions.

An alternative interpretation of heterogeneous age populations within a single sample is that older ages represent the crystallization age of the leucogranite and younger ages record disturbances to the U-Th/Pb system that occurred after primary crystallization. Processes such as thermal volume diffusion, dissolution/re-precipitation, and dynamic recrystallization may result in Pb-loss and/or new growth of monazite (Williams et al. 2011; Seydoux-Guillaume et al. 2002; Harlov et al. 2010; Hetherington et al. 2010; Cherniak et al. 2004; Cherniak and Pyle, 2008). However, minimum-temperature (650 to 750ºC) melts that characterize Himalayan leucogranites (Scaillet et al. 1990, 1996; Prince et al. 2001; Harris and Massey, 1994; Searle et al. 2010) contained insufficient heat for thermal diffusion of Pb in monazite, thought to occur above 900 ºC (Cherniak et al. 2004). Evidence of fluid-assisted or deformation-induced recrystallization is occasionally observed (e.g. LP09-74, where a 23.7 Ma high-U core is embayed along a sharp compositional contacts and overgrown by a 21.8 Ma low-U rim), but is easily identifiable using x-ray maps. In outcrops with multiple generations of intrusions, the youngest age populations are consistent with field relations (e.g. location 5; Figs. 2.2f, 2.3e) implying no thermal or fluid-assisted re-setting occurred during emplacement of successively younger leucogranites. Additionally, even when core age distributions overlap (e.g. LP09-169 and LP09-172 from location 6, Figs. 2.2g, 2.3f) the presence of younger rim ages support field interpretations. Furthermore, leucogranites within the LPD are fresh with little evidence of low-temperature hydrothermal alteration, such as replacement of primary phases (e.g. chlorite replacing biotite). Therefore, unless stated otherwise, we interpret monazite ages to represent primary crystallization from a melt.

To aid interpretation of heterogeneous age populations, analyses were assigned a designation of “emplacement”, “inherited”, or “recrystallized.” Recrystallized ages include 8 analyses from two grains for which there is textural evidence of recrystallization, such as embayed cores with irregular rims (e.g. LP09-74). For samples with homogeneous age distributions, the weighted mean age of the entire set of analyses is interpreted to represent the emplacement age of the leucogranite body. For samples with heterogeneous age distributions, the weighted mean age of the youngest set of analyses that define a single population (as indicated by low MSWD values) is interpreted to represent the emplacement age. For each individual leucogranite, any analyses older than the weighted mean emplacement age are interpreted to represent inherited age components. Throughout the LPD, emplacement and inherited ages overlap significantly, with inherited ages defining a broad peak 1-2 m.y. older than emplacement ages (Fig. 2.8a).

2.5.2 Sources of inheritance

Assuming that a single population or youngest population of ages records the time at which crystallization of leucogranite bodies occurred, then other sources for the component of older monazite ages must be identified. Three potential sources for older monazite include 1) pre-Himalayan monazite grains from the GHS protolith; 2) metamorphic monazite from either the source migmatite or host metapelites; or 3) igneous monazite that crystallized earlier in the history of the melt and was incorporated into younger melts. Inherited monazite has been observed in other Himalayan granites (Copeland et al. 1988; Harrison, McKeegan, et al. 1995; Viskupic et al. 2005; Simpson et al. 2000; Copeland et al. 1990).

The pre-Himalayan history of the GHS includes Proterozoic through Paleozoic deposition of Tethys Ocean sediments and the Cambro-Ordovician intrusion of granitoids and associated metamorphism. Detrital zircon (Parrish and Hodges, 1996; DeCelles, 2000) and monazite (White et al. 2001) studies of GHS metasediments yield age populations of 0.8 to 1.0 Ga, with a maximum at 1.7 Ga, and c. 500 Ma ages for orthogneiss and granitic plutons. U-Pb dating of Paleozoic magmatic rocks from the Himalaya range from c. 470 to 560 Ma (Miller et al. 2001; Schärer et al. 1986; Schärer and Allègre, 1983; Pognante et al. 1990; Girard and Bussy, 1999; Marquer et al. 2000). In this study, one grain (LP09_167_m003) out of the ~100 grains analyzed contains an inherited core with a ^{208}Pb/^{232}Th weighted mean age of 480 ± 7 Ma (n=3) overgrown by a 21.5 ± 0.6 Ma rim (Appendix B). The core may be derived from either a Cambro-Ordovician granitoid or from monazite that grew during Paleozoic metamorphism. Despite analyses of several hundred chemical domains, including cores and rims, no other Paleozoic or older ages were observed in this study. The existence of only one pre-

Himalayan monazite indicates that such ages are rare in the LPD protoliths, or that relict monazite rarely survives intact during minimum temperature melting. In either case, there is a minimal contribution of pre-Himalayan components to the observed inheritance patterns in the LPD.

Metamorphic rocks of the GHS constitute both the migmatitic source and metapelitic host rocks for Leo Pargil leucogranites, and therefore represent a possible source for inherited monazite. Following the onset of the India-Asia collision at ~55 Ma, metamorphic monazite formed during prograde, peak, and retrograde (i.e. isothermal decompression) metamorphic conditions and from 40 to 23 Ma in the LPD and adjacent GHS exposed in the Sutlej valley (Chambers et al. 2009; Langille et al. 2012). Kernel Density Estimate (KDE) plots (Vermeesch, 2012) of existing U-Th/Pb dates of monazite from metamorphic rocks compared to leucogranites from this study (Fig. 2.8b) indicates 7 m.y. of temporal overlap between the earliest leucogranite crystallization at 30 Ma and the end of metamorphic monazite growth at 23 Ma. Approximately 75% of the inherited ages in the leucogranites, however, post-date the youngest known metamorphic ages (23 Ma) of the host metapelites. For example, monazite ages from the host rock (LP09-162) at location 5 (Fig. 2.2f) range from 33.8 to 28.7 Ma, with one rim analysis at 23.0 ± 1.1 Ma (Langille et al. 2012). Within the same outcrop, monazites from leucogranites (Fig. 2.3e) yield a maximum age of 25.8 Ma, with most ages (185 of 187 analyses) between 23 and 19.5 Ma. Based on the differences in age, derivation of monazite from the host rock does not appear to explain the significant component of younger inherited ages observed. Migmatites in the deeper source region, on the other hand, may contribute metamorphic monazite younger than 23 Ma, but would be indistinguishable from igneous monazite. For example, leucogranite LP09-173 from the exposed migmatite terrane in the core of the LPD yields a crystallization age of 17.7 ± 0.1 Ma, but shows no clear evidence for inheritance of metamorphic monazite. The proportion of igneous monazite crystallization relative to metamorphic growth remains difficult to constrain volumetrically for the LPD because of the inherent bias in sampling leucogranites. While KDE plots (Fig. 2.8b) do not represent the absolute abundance of monazite with those ages, they serve to illustrate the temporal differences between the main pulse of igneous crystallization (<23 Ma) and metamorphic monazite growth (>23 Ma).

Igneous monazite that crystallized early in the melt history of the LPD represents another likely source of inheritance in the leucogranites. The size of a leucogranite body and the temperature of the host rock it intrudes exert strong controls on the cooling rate and final stage of crystallization. Due to their small width (cm- to m-scale), leucogranite bodies cooled rapidly after intruding non-migmatitic host metapelites (T <650ºC). Given these thermal constraints, long-lived crystallization (>1 Ma) of leucogranite bodies after emplacement is extremely unlikely (Harris et al. 2000). Furthermore, the nearly uniform ages with only slight variations (<0.1 Ma) observed in many samples (e.g. LP09-17, LP09-69, LP09-73, LP09-166, LP09-172, and LP09-179) imply that monazite crystallized within a short timeframe relative to emplacement. Therefore, the discrete and continuous patterns of inheritance observed in other samples are interpreted to represent early crystallization of igneous monazite prior to emplacement. Thus, the inheritance patterns have the potential to elucidate the time-scales over which processes such as generation, segregation, amalgamation, and mobilization occur. A discussion of five processes of melt evolution and their effect on monazite inheritance is described in detail below.

2.5.3 Five processes of melt evolution

The evolution of melt in the continental crust involves five processes: 1) generation, 2) segregation, 3) amalgamation, 4) mobilization, and 5) emplacement (Searle et al. 2010; Weinberg and Mark, 2008; Reichardt et al. 2010; Brown et al. 1995; Sawyer, 2001, 1994). Although these processes are roughly sequential, they need not progress in a linear fashion due to feedback relations (Brown, 2001; Brown and Solar, 1998). Rather, these processes operate simultaneously within the crust over variable time- and length-scales.

Melt generation occurs within metamorphic source rocks by fluid-absent incongruent melting of muscovite (Clemens and Vielzeuf, 1987; Inger and Harris, 1993; Searle et al. 2010). Under the P-T conditions required for melting, monazite precipitation is governed by the composition of the melt (LREE, P, H_2O) and the stability of other phases involved in melt reactions (apatite, garnet, xenotime). Apatite readily dissolves in strongly peraluminous melts with increased P solubility, causing LREE to precipitate into monazite (Wolf and London, 1995; Zeng et al. 2005). During first crystallization of the melt, the consumption of garnet releases Y and HREE into the system (Pyle and Spear, 2003). Monazite may incorporate the excess Y and HREE into rims on existing grains or into entirely new grains. Due to its low solubility (Rapp and Watson, 1986; Montel, 1993; Wolf and London, 1995) earlier metamorphic monazite cores may not equilibrate with the melt, and survive as resisitc grains (e.g. Appendix B). The time-scales over which melt generation occurs is limited by the rate of heat flow and has been modeled as exceeding 3 to 4 Ma (Harris et al. 2000).

As melt generation continues, migmatization proceeds through the process of segregation (Fig. 2.9). Melt-rich leucosome separates from the residuum in the

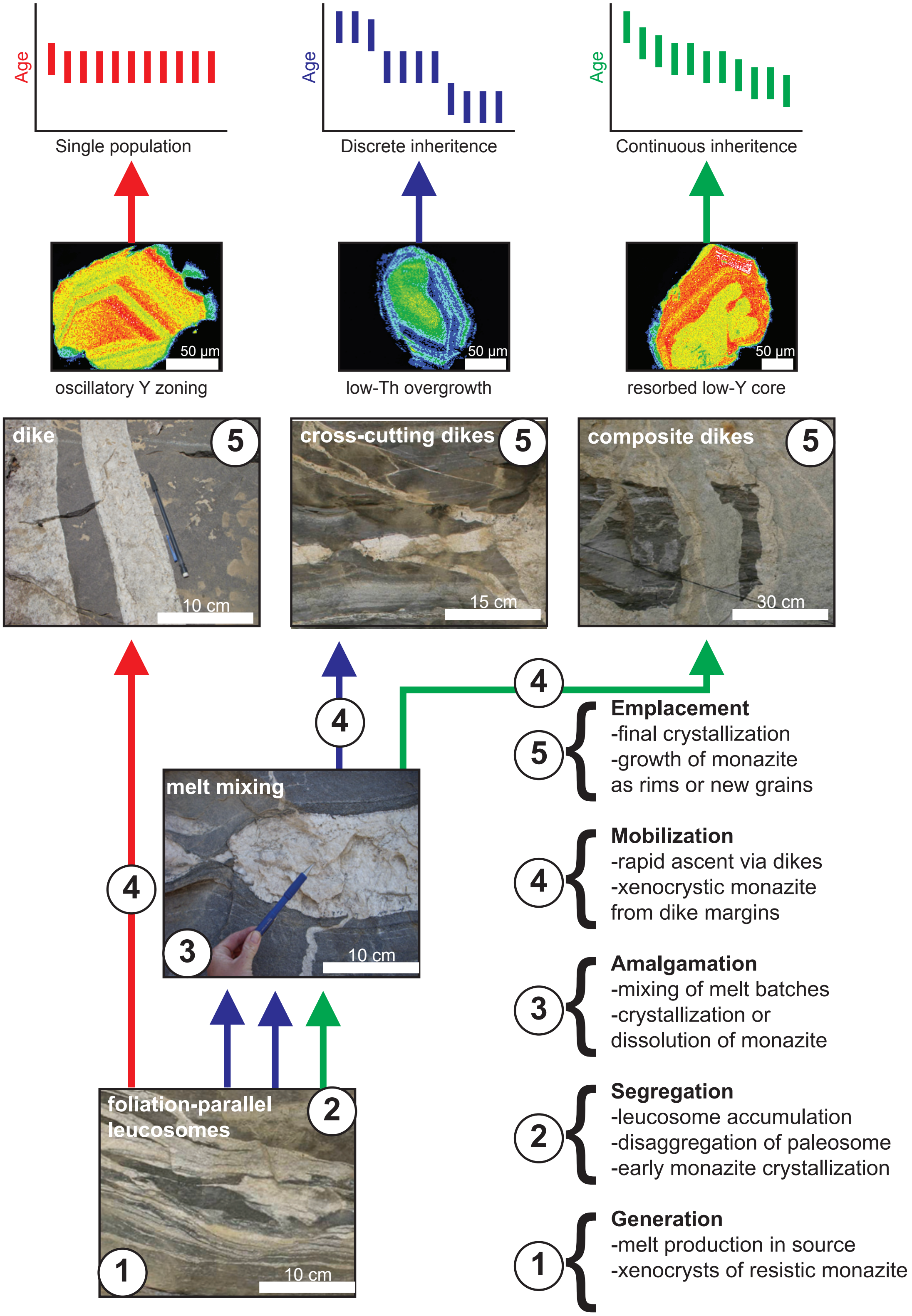

Figure 2.9 Schematic diagram illustrating how different combinations of processes affect age distributions and monazite chemistry. A single population (red) records generation, mobilization, and emplacement of a single dike and contains igneous monazite with oscillatory zoning. Discrete inheritance (blue) records early crystallization of high-Th cores during generation, segregation, and amalgamation of two different sources, followed by later crystallization of low-Th rims with oscillatory zoning. Continuous inheritance (green) records the early crystallization of a low-Y core during segregation, dissolution of the core during amalgamation, and overgrowth of a high-Y rim prior to emplacement.

melanosome and accumulates in low-pressure zones, such as in strain shadows, boudins, fold axes, and between foliation planes (Sawyer, 2001; Weinberg and Mark, 2008). For example, foliation-parallel sills such as LP09-73 LP09-172, LP09-173, and LP09-174 show where melt has accumulated as a result of segregation (Fig. 2.2). Extensive melting results in disaggregation of the paleosome (Brown et al. 1995; Weinberg and Mark, 2008), allowing intact metamorphic grains to become physically entrained in melt as xenocrysts. Igneous monazite continues to crystallize directly from the melt (Watt and Harley, 1993) as new grains and as overgrowths on the inherited monazite. Protracted crystallization results in continuous age distributions, such as those observed in LP09-157, LP09-158, LP09-167, LP09-169 and LP09-171 (Fig. 2.3).

Amalgamation occurs as migration pathways develop between leucosomal segregations along foliation planes, linking small isolated batches of melt into larger bodies (Brown and Solar, 1999; Weinberg, 1999). For example, melt in the leucosome can be traced into the dike LP09-179 (Fig. 2.2i). As melt batches from various sources mix together, previously crystallized monazites with contrasting trace element distributions may remain entrained in the melt. Comingling of individual melt batches affects the overall chemical composition of the melt, causing either dissolution of existing monazite or growth of new monazite depending on the saturation of H_2O, LREE and P (Rapp and Watson, 1986; Montel, 1993, 1986). If the melt mobilizes or freezes before achieving chemical equilibration with existing monazites through dissolution or diffusion, heterogeneous trace element distributions may be preserved (Sawyer, 1994). Heterogeneous trace element compositions of monazite grains and domains within a sample (e.g. LP09-70, LP09-153, LP09-154, LP09-157, LP09-167, LP09-168, LP09-169, LP09-171, LP09-173, and LP09-174) indicate chemical disequilibrium between the melt and inherited monazite, and may explain broad overlapping age distribution patterns.

Mobilization occurs when the volume of segregated or amalgamated melt increases and exceeds the confining pressure of the surrounding rock (Brown, 2004). Dikes propagate by hydraulic fracturing of the wall rock, opening up conduits that convey melt vertically to cooler, shallower levels (Rubin 1995; Weinberg 1996; Fig. 2.9). Ascent is rapid enough to prevent freezing of the cooling dike (Harris et al. 2000), and monazite crystallizes rapidly during this process. Furthermore, during hydraulic fracturing and ascent, fragments of wall rock may become incorporated into the leucogranite as xenoliths or xenocrysts. For example, dike LP09-16 cuts an earlier dike (LP09-17) and contains one inherited monazite (m052) with oscillatory zoning patterns and trace element compositions similar to low-U, low-Y monazites in LP09-17 but different than high-U, high-Y monazites from LP09-16 (Fig. 2.5). Ages from this monazite (20.6 to 22.2 Ma) overlap with LP09-17 (21.5 Ma) and are distinct from other LP09-16 monazites (19.9 Ma), suggesting that m052 was derived from the same leucogranite as LP09-17 and entrained during mobilization of LP09-16 melt.

Emplacement of a leucogranite into the host rock occurs when a dike freezes in place and undergoes the last increment of crystallization (Fig. 2.9). Heat flows through the surrounding host rock and previously intruded leucogranites, but is insufficient to cause further melting or assimilation, as indicated by sharp crosscutting relations in outcrop. Emplacement of a leucogranite could potentially affect monazite in adjacent rocks through Pb-loss, recrystallization, or dissolution and re-precipitation, especially if there are any fluids associated with the leucogranite, as is often the case in pegmatite dikes. In this study, however, examples of recrystallized monazite (e.g. LP09-74) are rare. Rapid emplacement and crystallization results in single age distributions with homogeneous trace element compositions (e.g. LP09-17, LP09-69, and LP09-166; Fig. 2.3).

Leucogranite emplacement is a function of the volume of melt, temperature of the melt and host rock, and structural position, however, a batch of melt may crystallize at any point during its evolution (Fig. 2.9). For example, generation alone produces a migmatite, whereas segregation results in the development of leucosomes (Fig. 2.9). Amalgamation may produce sills or ponds of melt that crystallize in place, and mobilization transports melt to shallower crustal levels through dikes. Furthermore, some melt processes have the potential to feedback into one another, such as mobilization leading to further amalgamation (Fig. 2.9). The emplacement age of each leucogranite body is represented by the last increment of crystallization regardless of where in the crust the leucogranite resides. Crystallization of monazite may occur over long time-scales (>10^6 yr) while mobilization and emplacement occur over much shorter time-scales (<10^3 yr). For example, the three discrete populations observed in LP09-168 span nearly 5 m.y. and indicate protracted monazite crystallization interpreted as distinct pulses of magmatism. The last increment of crystallization represents emplacement, whereas the spread in older ages represent early crystallization as the melt was generated, segregated, and amalgamated. Due to the high degree of complexity produced by the interaction of multiple processes, assigning specific ages to individual processes remains difficult; nevertheless, the overall age distribution, whether homogenous, discrete, or continuous, provides valuable insight regarding the evolution of melt in the LPD.

2.5.4 Melt history of Leo Pargil dome

Combined thermobarometric, geochronologic, geochemical and kinematic information indicates a protracted history of melting within the Leo Pargil dome (Fig. 2.8b). During prograde metamorphism, peak temperatures were attained by ~30 Ma (Chambers et al. 2009; Langille et al. 2012) and subsequent decompression of the metamorphic source rocks began producing melt by muscovite dehydration reactions. Granites crystallized during these initial stages of melt production from 30 to 23 Ma are foliated, boudinaged, and/or folded along with the metamorphic host rock (e.g. LP09-69, LP09-73). As melting continued from 23 to 18 Ma, larger volumes of melt were produced and emplaced as massive, crosscutting bodies, prevalent in lower structural positions of the LPD (e.g. LP09-157, LP09-167, LP09-168). Inherited monazite indicates melt residence time in the source region to be at least 1-2 m.y. Magmatism in the LPD is broadly synchronous with that of other regions of the GHS (Viskupic et al. 2005; Harrison et al. 1999; Copeland et al. 1990, 1988; King et al. 2010; Schärer et al. 1986; Schärer, 1984; Simpson et al. 2000) as well as the North Himalayan gneiss domes (Zhang et al. 2004; Lee et al. 2004; Aoya et al. 2005; Quigley et al. 2008).

Initiation of extension in the LPD by 23 Ma (Langille et al. 2012) coincides with the voluminous injection of leucogranites. Early pre-kinematic bodies of leucogranite (e.g. LP09-69, LP09-73) are cut by late post-kinematic intrusions (LP09-70, LP09-74), placing constraints on the timing of ductile deformation within the dome (Figs. 2.2b, 2.2c, 2.3b, 2.3c). The upper LPSZ was active at ~20 Ma, as indicated by ages of syn-kinematic, deformed leucogranites (LP09-16 and LP09-17) intruding it (Fig. 2.2a, 2.3a). Leucogranite emplacement diminished by 18 Ma, as the LPD continued to cool through 300-450ºC from 17 to 14 Ma (Thiede et al. 2006; Hintersberger et al. 2010). Final exhumation, E-W extension, and cooling below 120ºC occurred by brittle normal faulting from 10 to 2 Ma (Thiede et al. 2006; Fig. 2.8b).

2.6 Conclusions

The monazite crystallization record within leucogranites of the LPD indicates a protracted, pulsed melting history from 30 to 18 Ma. Monazite ages may be resolved into two components: 1) emplacement ages representing the crystallization of a dike or sill; and 2) inherited ages representing xenocrysts or antecrysts of monazite entrained in the melt at the time of emplacement. Emplacement ages provide constraints on the timing of melt injection relative to deformation, exhumation and cooling. Inherited ages are thought to represent early igneous crystallization, or late-stage metamorphic growth of monazite in the source region, but are younger than the prograde and retrograde metamorphic monazite of host rocks. Furthermore, inheritance patterns provide insight into the time-scales over which five processes of melt evolution (generation, segregation, amalgamation, mobilization, and emplacement) act. Partial melt may persist for at least 1-2 m.y. in the source region during segregation and amalgamation. This dataset provides constraints for geodynamic models involving partial melting of the Himalayan middle crust.

3. Granites of the Greater Himalayan Sequence from the Everest region to the Mahabharat range, eastern Nepal

3.1 Abstract

The orogenic core of the Himalaya consists of a continuous belt of schists and gneisses pervasively intruded by leucogranites derived from partial melting of crustal sources. This study employs high-temperature petrochronology of granites and granitoid gneisses to reveal the spatial and temporal relationships between metamorphism, melting, deformation, and exhumation of the Himalayan middle crust.

In eastern Nepal, the Greater Himalayan Sequence (GHS) extends southward from the Everest region to the Mahabharat range forming a broad thrust sheet above the Main Central thrust (MCT) zone. High-grade upper GHS rocks occur along two belts: 1) the main orographic front to the north and 2) the Mahabharat range to the south, whereas lower-grade rocks of the MCT zone and the Lesser Himalayan Sequence (LHS) occur between them near Okhaldungha. Three types of granitoids were distinguished along a ~100-km-long north-south transect across the area, including 1) weakly to highly deformed biotite-muscovite granitic orthogneisses of the MCT zone, 2) deformed tourmaline-bearing leucogranite dikes intruding kyanite-bearing gneisses of the Mahabharat range, and 3) undeformed to moderately deformed two-mica and tourmaline-bearing leucogranite dikes of the GHS. U-Th/Pb dating of zircon, monazite, xenotime, and allanite by LA-MC-ICPMS reveal magmatic ages and/or metamorphic overprints of each type of granite. Granites and orthogneisses of the MCT zone yield dates of c.1800 Ma with evidence for Archean inheritance and recent Pb-loss. Magmatic ages are

consistent with those of the Phaplu orthogneiss and Pb-loss may be a result of Tertiary deformation. The Mahabharat leucogranites dominantly yield ages of c. 480 Ma overprinted by Oligo-Miocene metamorphism and deformation. However, one leucogranite specimen from the Mahabharat yields magmatic zircon crystallization ages ranging from 28.5 to 21 Ma, providing evidence for Oligo-Miocene melting farther toward the foreland than previously recognized. By contrast, GHS granites yield monazite ages ranging from 23-18 Ma near Namche Bazaar, and 17-13 Ma near Dudh Kund. Monazite ages imply that the foreland edge of the GHS thrust sheet records an older history of metamorphism and a smaller amount of melting than the hinterland, whereas rocks of the intervening MCT zone do not record a metamorphic overprint.

3.2 Introduction

The Greater Himalayan Sequence (GHS) forms the core of the Himalayan orogen and is crucial to understanding the thermal history of continent-continent collisions. Much attention has been focused on understanding melting in the upper part of the GHS, however, comparatively less attention has focused on the exposures of the GHS thrust sheet that occur in the foreland of the orogen. This study exploits exposures of mid-crustal rocks in the eastern Nepal Himalaya extending from the high peaks of the Everest region (>8000 m) to the relatively low foothills (< 3500m) of the Mahabharat range over a structural thickness of 10-15 km and a geographic distance of ~100 km to examine in detail the contrasting styles and histories of metamorphism, melting, deformation, and exhumation between the hinterland and the foreland of the orogen.

A ~100-km-long orogen-perpendicular transect bisects two major tectonostratigraphic units: 1) amphibolite-facies to migmatitic schists and gneisses intruded by granites of the Greater Himalayan Sequence (GHS), and 2) greenschist-facies phyllites, psammites, and granitic orthogneisses of the Lesser Himalayan Sequence (LHS). The Main Central thrust (MCT) represents the major discontinuity that emplaced the crystalline GHS thrust sheet above the LHS footwall. Erosion of the gently extensive north-dipping GHS thrust sheet in eastern Nepal exposes the MCT zone and underlying LHS through several tectonic windows, including the Ramechap window (Schelling 1992), whereas the Mahabharat range to the south preserves crystalline rocks of GHS affinity (Fig. 3.1). Previous workers have referred to the rocks exposed in the Mahabharat range as the Lesser Himalayan crystallines (Le Fort 1975), the Lesser Himalayan crystalline nappes (Upreti and Le Fort, 1999), the Outer Crystalline klippen (Johnson, 2005). The rocks exposed in the Mahabharat share many similarities with those of the GHS north of the Ramechap window, however, whether they are part of the same thrust sheet (i.e. Schelling, 1992; Johnson, 2005) or represent a different tectonostratigraphic section (i.e. Upreti and Le Fort, 1999) remains a matter of debate with direct bearing on the significance of the MCT zone in this area. This study characterizes the geochronologic relationships between granitic rocks and host gneisses of the GHS, MCT zone, and Mahabharat in order to determine the timing of melt crystallization and metamorphism in different parts of the orogen.

3.2.1 Granites of the GHS and MCT zone

The GHS crystalline thrust sheet forms the core of the Himalayan orogen and consists of a series of schists, gneisses, and granites. The protolith to the GHS is a thick accumulation of Proterozoic through Cretaceous passive margin sediments including carbonates, sandstones, greywackes, and shales that have been metamorphosed to calc-

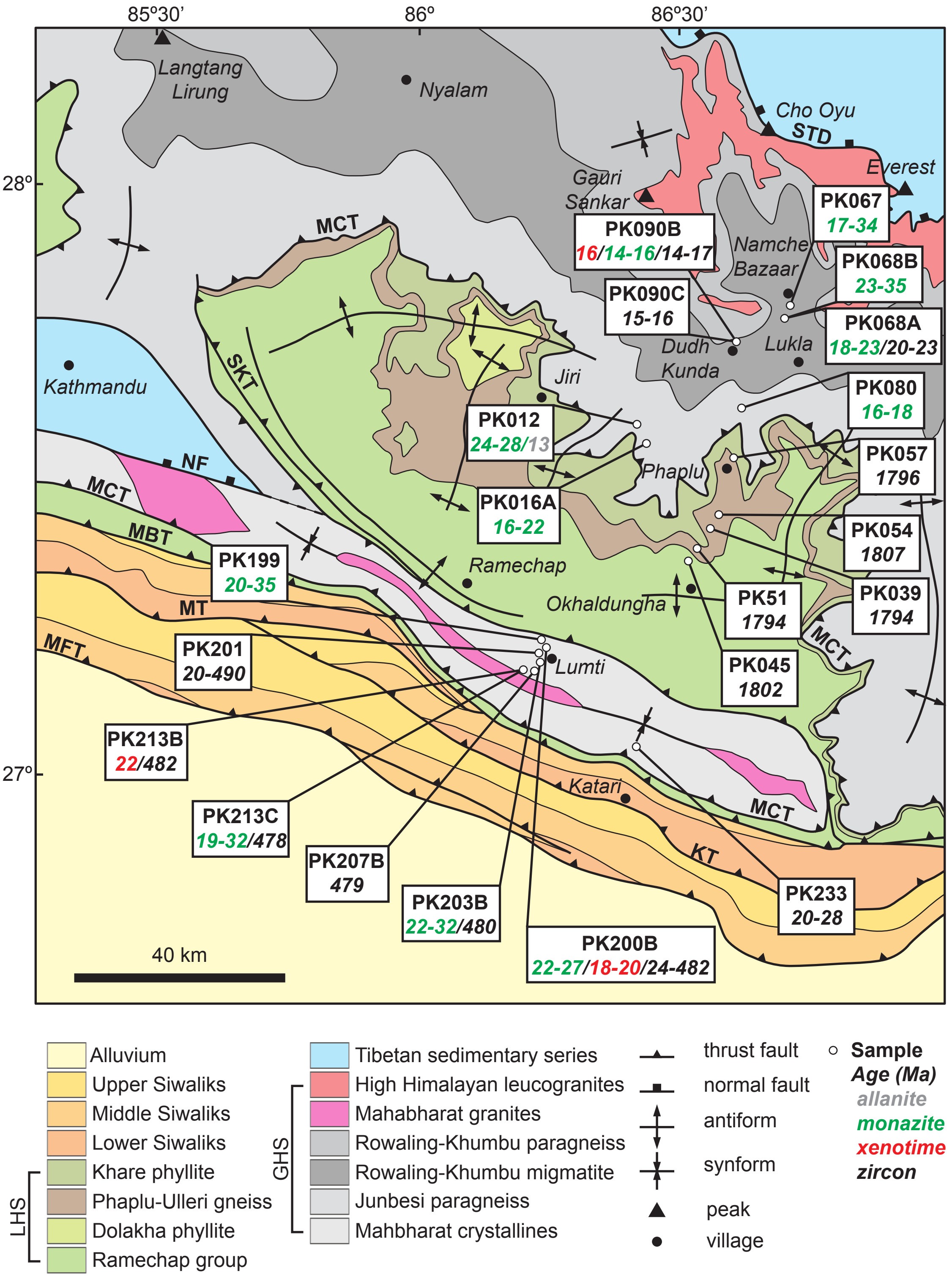

Figure 3.1 Regional geologic map of eastern Nepal (after Schelling 1992). Abbreviations are KT, Kamala thrust; MBT, Main Boundary thrust; MCT, Main Central thrust; MFT, Main Frontal thrust; MT, Marin thrust; NF, Narayan Than fault; SKT, Sun Kosi thrust; STD, South Tibetan detachment.

silicate gneisses, schists and paragneisses. In addition to metasedimentary rocks, several lower Paleozoic granites and augen gneisses occur throughout the GHS, and are well exposed in the Mahabharat range (Fig. 3.1). Innumerable bodies of Tertiary granites pervasively intrude migmatites of the upper GHS, forming plutons and dike networks in the High Himalaya. Additionally, Paleoproterozoic granitoid gneisses occur near the MCT zone at the interface between base of the GHS and the upper LHS. Prior geochronologic data for each of the three types of granitic rocks are summarized here.

The MCT was originally described as a discrete, gently dipping (25-30º) thrust contact between crystalline rocks of the hanging wall with mica-schist and orthogneiss at the base and low-grade metasedimentary rocks of the footwall with quartzite at their top (Heim and Gansser, 1939). Subsequently, other definitions have been used, including lithological differences or metamorphic criteria, such as the first appearance of kyanite (Le Fort 1975; Colchen et al. 1986), prompting the demarcation of multiple discrete structures (e.g. MCT I and MCT II of Arita, 1983). The term MCT zone is used here to describe the rocks previously attributed to the upper LHS and/or the lower GHS that occur between the two contrasting MCT locations. Our field observations suggest that a zone of distributed ductile shear recorded by phyllites, quartzites, and gneisses of the MCT zone is cut by late-stage brittle faults, which repeat the tectonostratigraphic section.

3.2.2 Paleoproterozoic gneisses

Paleoproterozoic gneisses comprise a large proportion of the Greater and Lesser Himalayan thrust sheets. Field relationships indicate that augen gneiss extends almost the entire length of the Himalaya and occurs at different structural positions levels within intercalated schists and metasandstones ((Le Fort, 1975; Arita, 1983; Schelling and Arita, 1991; Schelling, 1992; Le Fort and Rai, 1999; Singh and Jain, 2003; Searle et al. 2008). The variable deformation textures in the gneiss, ranging from undeformed granite to protomylonitic augen gneiss, and its widespread occurrence has prompted the use of several different names within Nepal, including the Ulleri gneiss (Le Fort and Pecher, 1974), Melung gneiss (Ishida and Ohta, 1973), the Syabru Bensi gneiss (MacFarlane et al. 1992), and the Phaplu gneiss (Maruo and Kizaki, 1981). The structural position of the gneiss has been interpreted to be above, or below, the MCT zone. Various authors have attributed the Phaplu-Ulleri gneiss to either the GHS (i.e. Hubbard et al. 1989; Searle et al. 2003; Goscombe et al. 2006; Searle et al. 2008), or the LHS (i.e. McFarlane et al. 1992; DeCelles et al, 2001; Robinson et al. 2001; Catlos et al. 2002).

Previous investigations of the Ulleri augen gneiss in western Nepal have determined a U-Pb zircon age of 1831 ± 17 Ma (DeCelles et al. 2001) whereas the Phaplu augen gneiss yielded a SHRIMP ^{208}Pb/^{232}Th monazite date of 1566 ± 49 Ma (Catlos et al. 2002). A similar orthogneiss unit, the Ama Drime orthogneiss, yields U-Pb xenotime, zircon, and monazite ages of ~1800 Ma (Cottle et al. 2009).

3.2.3 Ordovician granites of the Mahabharat

A belt of lower Paleozoic (Cambrian-Ordovician) peraluminous granitic plutons form the backbone of the Mahabharat range at the southern edge of the GHS crystalline thrust sheet (Le Fort, 1983; Debon et al. 1986, Le Fort and Rai, 1999; Johnson et al. 2000; Johnson et al. 2003). Compositionally, the Mahabharat granites are similar to augen gneisses of the GHS (i.e. Formation III of Le Fort et al. 1977), and consist of tourmaline-bearing and two-mica leucogranites. Their formation has been attributed to either large-scale crustal anatexis during extension of the northern margin of the India (e.g. Le Fort and Rai, 1999), or a Cambro-Ordovician orogenic event (e.g. the Bhimpehedian Orogeny of Cawood et al. 2007). In general, fabric development in the granites is minor, however, smaller bodies and the margins of larger plutons are highly sheared into granitic gneiss in an orientation concordant with the host rock foliation, indicating emplacement either predated or was contemporaneous with regional deformation (Schärer and Allegre, 1983; Rai and Le Fort, 1999; Upreti and Le Fort, 1999).

Geochronology of leucogranites exposed in the Mahabharat yield Paleozoic ages comparable to orthogneisses of the GHS (Schärer and Allègre, 1983; Gehrels et al. 1999, 2003; Cawood et al. 2007). In one of the earliest attempts at dating granites from the Himalaya by U-Pb, Schärer and Allegre (1983) obtained a U-Pb monazite date of 470 ± 4 Ma for the Palung granite exposed south of Kathmandu, with evidence of inherited zircon ranging from 800-1700 Ma and no disturbance of the U-Pb system during Himalayan thrusting. Additionally, previous workers have determined zircon U-Pb dates of 476 ± 3 Ma for the Simchar granite exposed east of the Palung granite (Cawood et al. 2007), 480 ± 11 Ma (Gehrels et al. 2006). Zircon cores sampled from the Simchar granite and associated xenoliths indicate inheritance from ~1000 Ma and ~500 Ma (Cawood et al. 2007). The inferred source for these granites is the Bhimphedi Group, equivalent in age to the Haimanta group.

3.2.4 Tertiary granites of the GHS

Granites of the Everest region have been studied extensively, providing a robust dataset for which to compare ages this study. In an early application of U-Pb dating to the Makalu leucogranites, Schärer (1984) obtained dates of 21.9 ± 0.2 and 24.0 ± 0.4 Ma from monazite, zircon, and xenotime grains, suggesting that the Makalu granite was generated over a period of at least 2 m.y. Copeland (1988) obtained a concordant zircon date of 19.5 ± 0.4 Ma, interpreted to represent the crystallization age of the Everest granite, as well as a older ages indicative of inheritance, whereas, monazite U-Pb analyses yield an array from an upper intercept of 471 ± 10 Ma to a reversely discordant data point with evidence for excess ^{206}Pb derived from initial disequilibrium of ^{230}Th (e.g. Schärer 1984). LA-ICPMS analysis of monazite from the Nuptse leucogranite yield a ^{208}Pb/^{232}Th age of 23.6 ± 0.7 Ma with evidence for protracted crystallization from 26-23 Ma (Jessup et al. 2008).

Metamorphic rocks of the Solu-Khumbu/Everest region record an Eohimalayan thermal event at around 32.4 ± 0.4 and a Neohimalayan event at 22.7 ± 0.2, with emplacement of the Everest granite at 20.5-21.3 Ma (Simpson, 2000). SIMS Th-Pb monazite ages of the GHS in the Everest region from 14.5 ± 0.7 to 548 ± 17 Ma, but dominantly record crystallization from 25 to 21 Ma (Catlos, Harrison, et al. 2002). A leucogranite yields a monazite Th-Pb date of 20.2 ± 0.6 Ma (Catlos et al. 2002). U-Pb crystallization ages of 21.33 ± 0.03 and 21.80 ± 0.05 Ma with evidence for earlier magmatic crystallization of monazite, xenotime, and zircon from 23-26 Ma were obtained from the Namche gneiss as well as leucogranites exposed in the Namche, Gokyo Ri, and Fifth Lake outcrops (Viskupic and Hodges, 2001; Viskupic et al. 2005).

3.3 Samples and Methods

3.3.1 Sampling strategy

In order to obtain and interpret geochronologic data while preserving its context, samples were selected according to three specific criteria at a variety of scales: 1) km-scale spatial distribution and structural position; 2) m-scale outcrop relations; and 3) µm-scale mineral characteristics. The goal of this sampling strategy is to characterize the melting history of the Himalaya with respect to structural setting, deformation and chemical composition. Crosscutting relations, the degree of fabric development, and the orientation of the intrusive bodies relative to host rock fabrics were documented. A total of 20 samples (5 orthogneiss, 7 Mahabharat leucogranites, 3 High Himalayan leucogranites, and 5 paragneisses) were collected and prepared for laboratory analysis. Leucogranites range from medium- to very coarse-grained (3-10 mm) and share a peraluminous composition containing K-feldspar + plagioclase + quartz + muscovite ± tourmaline ± biotite ± garnet. Accessory phases include apatite, zircon, monazite, and occasional xenotime or intergrowths of zircon and xenotime. Monazite separates from 3-5 kg granite samples are prepared using standard techniques including crushing, milling, sieving, and separation by density and magnetic susceptibility. Monazite grains are handpicked, mounted in a 2.5 cm epoxy resin discs, and polished to expose approximately equatorial sections through the grains.

Thin section billets of metamorphic samples were cut parallel to the lineation (where present) and perpendicular to the foliation. Thin sections were cut for the four (4) orthogneiss samples (excluding the aplitic dike) as well as the five (5) metapelites. Orthogneiss samples were subsequently crushed to separate enough crystalline zircons for analysis.

3.3.2 Monazite BSE imaging and zircon CL imaging

For thin sections, monazite and zircon grains were initially located and identified using an FEI Quanta Scanning Electron Microscope equipped with a backscattered electron (BSE) detector. Zircons were imaged using a cathodoluminescence (CL) detector in order to reveal internal zoning. Monazite zoning in BSE images reflects chemical zoning, but cannot be unequivocally linked to a specific element or group of elements. Therefore, several monazite grains were selected for further imaging.

3.3.3 EPMA X-ray chemical mapping

Five to ten representative monazite grains from each sample are selected for imaging using a Cameca SX-100 electron probe micro-analyzer (EPMA) using five Wavelength Dispersive Spectrometers (WDS) to measure o measure Y (LTAP, Lα), La (LPET, Lα), Nd (PET, Lα), Th (LPET, Mα), and U (LPET, Mβ) X-rays with a 100 ms dwell time, 15-20 keV accelerating voltage, and 200 nA beam current (equating to a ~1 μm^3 interaction volume). Qualitative X-ray maps reveal phase relations and the presence of inclusions to guide laser ablation analysis. For ease of comparison, maps are scaled so the same number of counts corresponds to the same color for all grains.

La represents the behavior of LREE during monazite crystallization, whereas Y serves as a proxy for the behavior of HREE. Nd, U, and Th variation are measured because they directly affect isotopic analyses of these elements. Although qualitative, X-ray maps reveal textural information such as internal zoning patterns and core-rim relationships and aid in targeting specific chemical domains for isotopic analysis. Understanding the distribution of these elements potentially provides important information on the growth history of individual crystals (Williams et al. 1999, 2007; Zhu and O'Nions, 1999; Cocherie et al. 1998; Stepanov et al. 2012).

3.3.4 LASS-ICPMS U-Th/Pb and trace element analysis

The laser ablation split stream inductively coupled plasma mass spectrometry (LASS-ICPMS) facility at the University of California Santa Barbara (UCSB) utilizes He gas to convey ablated material from the HelEx cell of a Photon Machines Analyte G1 193 nm ArF excimer laser into a glass mixing bulb, where, with the addition of Ar, the gas flow is split and directed into 1) a Nu Plasma HR multi-collector ICPMS to measure ^{238}U, ^{232}Th, and ^{208,207,206}Pb and ^{204}X isotopes (where X is the isotopes of Pb and Hg), and 2) an Agilent 7700S quadrupole ICPMS equipped with an additional interface rotary pump, to measure trace elements or 3) a Nu Instruments AttoM single collector ICPMS operated in Linked Scan mode to measure a range of masses, from ^{31}P to ^{174}Yb.

Trace element analyses were normalized to values determined by EPMA and LA-ICPMS for Bananeira monazite at UCSB. Uncertainties for trace elements include 2SE precision of 2-5% for elements more abundant than 100 ppm, 5-10% for elements down to 1 ppm, and >10% for those less than 1 ppm (e.g. Kylander-Clark et al. 2013).

Several data collection strategies were employed to analyze different materials and samples, including monazite spot analyses, monazite grain raster maps, zircon spot analyses, xenotime spot analyses, and allanite line scans. Ablation parameters were conducted at settings calibrated for different mineral phases. A spot size of 7-10 μm was used for monazite and xenotime, 12-25 μm for zircon, and 10-μm-wide line scans measuring 20-50 μm for allanite. Other parameters include laser energy of 3 to 4 mJ, repetition rate of 3 to 4 Hz, and an ablation pit depth of 2 to 5 μm.

To monitor and correct for down-hole fractionation, matrix-matched reference materials consisting of several monazite crystals or fragments with known isotopic ratios and/or trace element concentrations were analyzed before and after every 6 to 10 unknown analyses. “44069” monazite with an ID-TIMS Pb/U age of 424.9 Ma (Aleinikoff et al. 2006) served as the primary (U-Th)/Pb standard for isotopic ratios, whereas the in-house Bananeira monazite (512 Ma Pb/U age) was used to correct U, Th, and trace element concentrations. “FC-1” monazite with an ID-TIMS ^{206}Pb/^{238}U age of 55.7 Ma (Horstwood et al. 2003) provided an additional check on the correction factors applied to the unknowns for each analytical session. Data reduction, including corrections for baseline, instrumental drift, mass bias, and down-hole fractionation were carried out using Iolite v. 2.31 for Igor Pro v. 6.32 (Paton et al. 2011). Concordia and weighted mean plots were calculated in Isoplot v2.4 (Ludwig 2000) using the ^{238}U, ^{235}U, and ^{232}Th decay constants of Steiger and Jäger (1977). Based on the reproducibility of the ^{207}Pb/^{206}Pb, ^{206}Pb/^{238}U, ^{207}Pb/^{235}U, and ^{208}Pb/^{232}Th ratios of the secondary reference materials, an additional 1.5 to 2% uncertainty was added in quadrature to the 2σ internal error calculated using Iolite. Repeat analyses of Bananeira yield a ^{206}Pb/^{238}U date of 508.2 ± 1.3 (MSWD = 1.1) and ^{208}Pb/^{232}Th dates of 495.5 ± 1.7 (MSWD = 1.9). Analyses of FC-1 monazite and xenotime yield ^{206}Pb/^{238}U dates of 56.1 ± 0.2 (MSWD = 2.2) and ^{208}Pb/^{232}Th dates of 54.2 ± 0.2 (MSWD = 1.6). FC-1 xenotime, normalized to 44069 monazite, yields ^{206}Pb/^{238}U dates of 54.8 ± 0.5 (MSWD = 1.3).

Zircons were ablated using a spot diameter of 20 μm, with the exception of very high-U (i.e. >6,000 ppm) grains of PK201A analyzed using a 12-μm-diameter spot. Data were normalized to zircon 91500 (1065.4 ± 0.3 Ma ^{207}Pb/^{206}Pb ID-TIMS age and 1062.4 ±0.4 Ma ^{206}Pb/^{238}U ID-TIMS age, Wiedenbeck et al. 1995) as a primary reference material. Secondary reference materials GJ1 (608.5 ± 0.4 Ma ^{207}Pb/^{206}Pb ID-TIMS age, Jackson et al. 2004 and 601.7 ± 1.3 Ma ^{206}Pb/^{238}U ID-TIMS age, Condon, unpublished) yielded a population of 601.25 ± 0.69 (MSWD = 1.1) and Plešovice (337.13 ± 0.37 Ma

^{206}Pb/^{238}U ID-TIMS age; Sláma et al. 2008) yielded a population of 338.8 ± 7.8 (MSWD = 1.7).

Allanite grains were analyzed using 10-µm-wide line scans measuring 20-50 µm in length, in order to minimize down-hole fractionation and dependence on matrix-matched standards. Data was normalized to 44069 monazite as a primary reference material for U-Th/Pb isotopic measurements and Bananeira for REE. Additionally, analyses were screened for evidence of accidental overlap with other phases and anomalous points were rejected. Repeat analyses of the Diabosatsu allanite as a secondary reference material yielded an age of 12.2 ± 7.6 and 4935 ± 470 Ma (MSWD = 0.4), indistinguishable within uncertainty from previous ~13 Ma age determinations (McFarlane and McCulloch, 2007) confirming the accuracy of this analytical approach.

3.4 Results

In general, the three types of granites occur in spatially distinct zones in different parts of the orogen: orthogneisses occur in the MCT zone, Mahabharat granites occur toward the foreland south of the MCT zone and Ramechap window, and GHS leucogranites occur in the hinterland north of the MCT zone (Fig. 3.1). For each of the three types of granites structural and petrologic observations are reported followed by detailed results of coupled U-Th/Pb and REE petrochronologic analysis of accessory phases zircon, monazite, xenotime, and allanite (Table 3.1).

	Lat (ºN)	Long (ºE)	Elev (m)	Rock type	Relations	Mineral	Age (Ma)
Main Central thrust zone							
PK039	27.381076	86.530079	2962	orthogneiss	strongly deformed	zrn	1794 ± 1.3
PK045	27.353357	86.520277	2370	orthogneiss	undeformed	zrn	1802 ±2.3
PK051	27.414445	86.549553	2801	orthogneiss	weakly deformed	zrn	1794 ± 1.5
PK054	27.434227	86.572050	2281	orthogneiss	aplite dike	zrn	1807 ± 1.3
PK057	27.538061	86.594378	2472	orthogneiss	moderately deformed	zrn	1796 ± 2.0
PK012	27.580986	86.413289	1799	paragneiss	host rock	mnz	24-28
PK012						aln	13.3 ± 1.9
PK016A	27.551863	86.431086	3086	paragneiss	host rock	mnz	16-22
PK080	27.621495	86.611740	3538	paragneiss	host rock	mnz	16-18
Mahabharat							
PK199	27.224801	86.226367	1195	paragneiss	host rock	mnz	20-35
PK200B	27.223143	86.226217	1262	leucogranite	cuts foliation	zrn	24-482
						mnz	22-27
						xnt	18-20
PK201A	27.217259	86.222236	1352	leucogranite	foliated	zrn	20-490
PK203B	27.207639	86.218145	1296	leucogranite	foliation-parallel	zrn	480.1 ± 1.4
						mnz	22.3-31.5
PK207B	27.190567	86.213850	875	leucogranite	foliation-parallel	zrn	478.7 ± 1.3
PK213B	27.176512	86.200288	1182	leucogranite	foliation-parallel	zrn	~482
						xnt	21.8
PK213C	27.176512	86.200288	1182	leucogranite	cuts PK213B	zrn	~478
						mnz	19-32
PK233	27.052644	86.413334	1271	leucogranite	foliation-parallel	zrn	20-28
Greater Himalayan Sequence							
PK067	27.787514	86.719666	2762	migmatite	host rock	mnz	17-34
PK068B	27.761691	86.714496	2649	migmatite	host rock	mnz	23-35
PK068A	27.761691	86.714496	2649	leucogranite	foliation-parallel	zrn	20-23
						mnz	18-23
PK090B	27.712604	86.601222	4636	leucogranite	foliation-parallel	zrn	14.0-16.6
						mnz	14-17
						xnt	15.8
PK090C	27.712604	86.601222	4636	leucogranite	cuts foliation	zrn	15.4-16.1

Table 3.1 Summary of U-Th/Pb results; zrn, zircon; mnz, monazite; xnt, xenotime; aln, allanite.

3.4.1 Structural and petrologic observations

3.4.1.1 MCT zone orthogneisses

Within the MCT zone, a distinct orthogneiss unit is juxtaposed against intercalated greenschist-facies phyllite and metasandstone. Although individual outcrops of orthogneiss are discontinuous and dismembered by numerous brittle faults, they share a common mineralogy including the presence of biotite (sometimes altered to chlorite), pink-orange K-feldspar, plagioclase, and quartz. A total of five samples, including four orthogneisses with varying degrees of fabric development and an associated aplite, were collected along a 25-km section of the transect between Okhaldungha and Phaplu (Fig. 3.1).

PK045 is a weakly deformed coarse-grained granitoid gneiss sampled from within the footwall of the MCT zone (Fig. 3.2a). Large K-feldspars (5-10 mm) exhibit primary textures, such as simple twinning. PK051 is a weakly deformed orthogneiss from within the MCT zone. Compared to PK045, the gneiss shows evidence for grain size reduction and recrystallization (Fig. 3.2b). Collected ~2 km north of Phaplu, PK057 is a moderately deformed orthogneiss within the MCT zone and exhibits significant grain size reduction compared to PK051 or PK045 (Fig. 3.2c). PK039 is a strongly deformed biotite-bearing orthogneiss with augens of recrystallized K-feldspar and quartz from within the MCT zone (Figs. 3.2d, 3.3a). Large (1-3 cm) grains of bronze-colored biotite are present in weathered surfaces. The foliation (240/38º NW) is curviplanar, with a mineral lineation defined by elongated biotite (28º to 331). PK054 is a quartz-rich aplite vein sampled from within weakly deformed granitoid gneiss of the MCT zone (Fig. 3.3b). The vein is isotropic with regard to fabric development, and cuts the orthogneiss foliation.

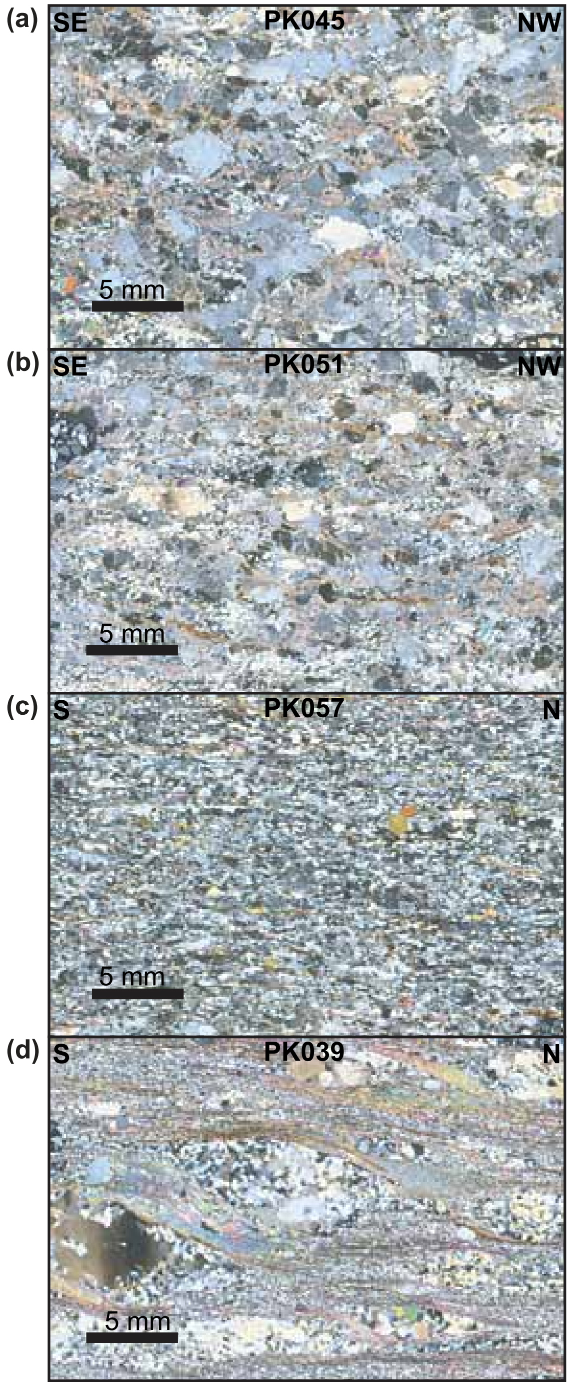

Figure 3.2 Thin section photomicrographs of **a)** undeformed granitic protolith (PK045) **b)** weakly deformed orthogneiss (PK051), **c)** moderately deformed orthogneiss (PK057), and **d)** strongly deformed augen gneiss (PK039).

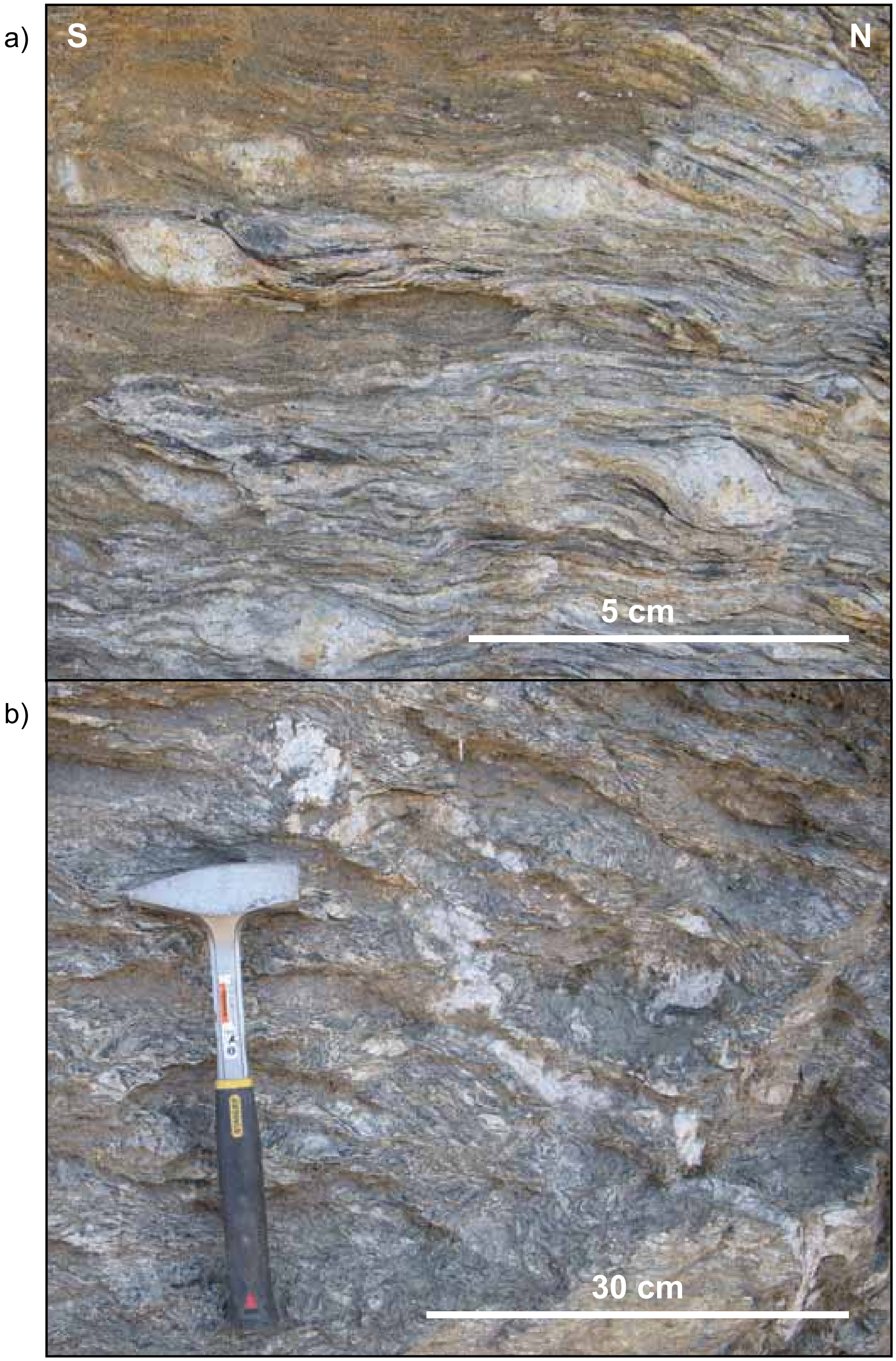

Figure 3.3 Field photographs of a) augen orthogneiss with top-to-the-south asymmetry visible in feldspar porphyroclasts, and b) deformed aplite dike (PK054) intruded into augen orthogneiss.

In addition to orthogneisses of the MCT zone, three metapelitic paragneisses were analyzed in order to assess the age of metamorphism associated with MCT deformation. PK012 is a garnet-bearing metapelite from the MCT zone near Jiri. that PK016A is a garnet-kyanite schist from structurally higher position within the GHS above the MCT zone with a well developed foliation (312/25º NE) and lineation (2º to 016). PK080 is a garnet-biotite gneiss from within the structurally higher migmatitic portion of the GHS (Fig. 3.1). Tourmaline-bearing leucosomes define a foliation (179/25º W) and lineation (14º to 166).

3.4.1.2 Mahabharat leucogranites

Several leucogranites occur within the kyanite-grade paragneisses and orthogneisses of the Mahabharat range, ranging from cm-scale leucosomes to m-scale dikes. Several elongate leucogranite plutons have been mapped in the Mahabharat range, but the granites collected in this study are exclusively smaller-scale bodies.

PK200B is a 20-cm-wide leucogranite dike that cuts foliation (157/14 SW) in the host orthogneiss (PK200A; Fig. 3.4a). The orthogneiss also contains 5- to 10-cm-wide leucosomes boudinaged parallel to foliation. PK201A is a coarse-grained leucogranite with 2-cm-long tourmaline and a weak foliation (063/30º SE) that crops out along the crest of the Mahabharat range near the village of Lumti (Fig. 3.1).

PK203B was sampled on the southern side of the Mahabharat range downslope from Lumti, and is a 20-cm-thick, coarse-grained leucogranite dike with l-cm-long tourmaline and 3-mm-diameter garnet. The dike is boudinaged in an orientation sub-parallel to the foliation (119/39º SW) of the host migmatite (PK203A; Fig. 3.4b). The migmatite contains tourmaline-bearing leucosomes defining a lineation plunging 20º

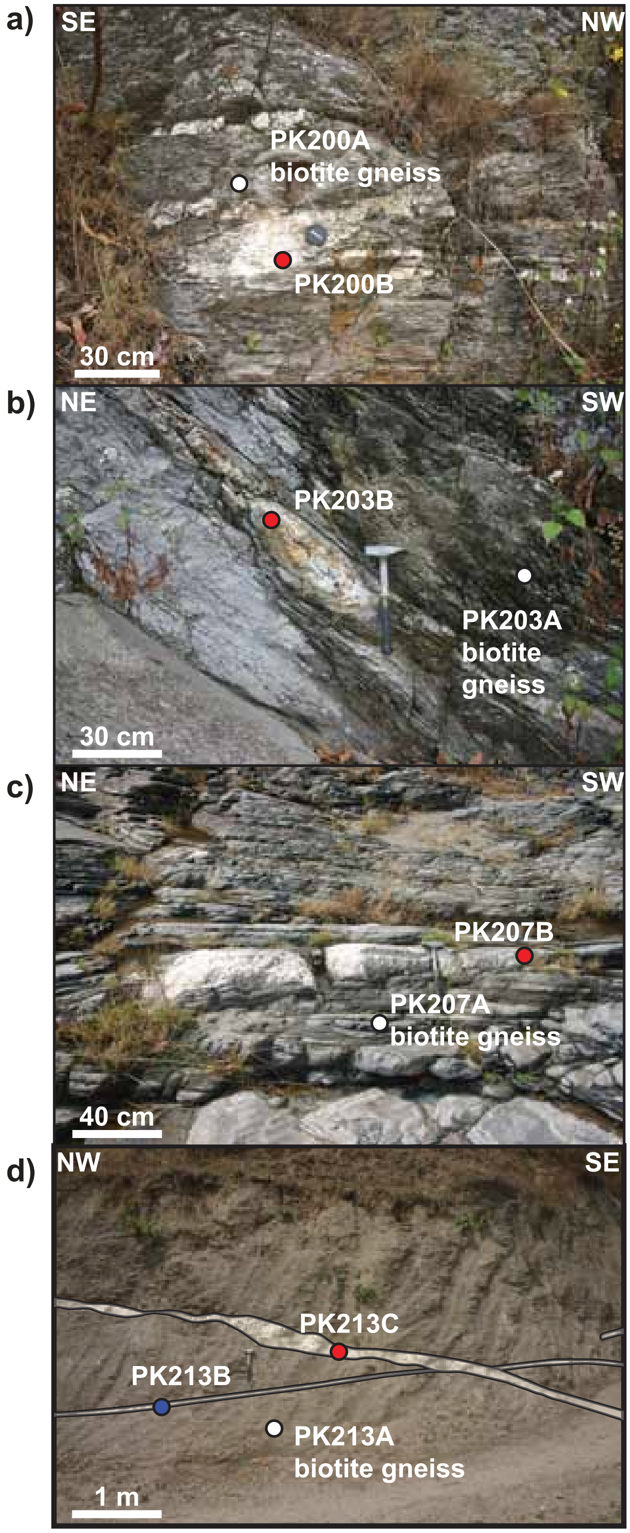

Figure 3.4 Field photographs of leucogranite dikes from the Mahabharat range. Deformed biotite gneiss is intruded by boudinaged leucogranites **a)** PK200B, **b)** PK203B and **c)** PK207B. **d)** Biotite gneiss is intruded by an early granite dike (PK213B) and cut by a later dike (PK213C).

toward the SE (160). PK207B is a leucogranite dike oriented parallel to foliation (116/32 W) in the host gneiss (Fig. 3.4c). The fine-grained host gneiss (PK207A) has a mineral-elongation lineation defined by muscovite and biotite.

PK213B and PK213C are leucogranites sampled from the same outcrop near (Fig. 3.4d). PK213B is oriented parallel to the host orthogneiss (PK213A), and is cut by PK213C. PK233 is a 10-cm-wide, tourmaline-bearing leucogranite dike oriented parallel to the foliation (261/46 NE) in the intercalated biotite-muscovite schists and quartzite host rock. The granite was sampled along the road from Katari Bazaar to Okhaldungha (Fig. 3.1). Additionally, a garnet-kyanite schist (PK199) from the Mahabharat range was sampled to compare metamorphic monazite ages to igneous monazite and xenotime ages.

3.4.1.3 GHS leucogranites

Collected ~4 km south of Namche Bazaar, PK068A is a leucogranite from a 1-m-thick dike that parallels the gently east-dipping foliation (000/20º E) of the garnet-biotite host gneiss (PK068B). The leucogranite contains abundant monazite and zircon, and shows evidence of biotite-rich selvages entrained in leucogranite (Fig. 3.5a). The host rock (PK068B) at this location is similar to that sampled for U-Th/Pb analysis ~2 km to the north (PK067). PK067 is a garnet-biotite migmatitic gneiss with abundant large (>100 μm) monazite grains.

PK090B and PK090C are leucogranites sampled from the same outcrop at near Dudh Kund. The host gneiss (PK090A) is complexly folded and consists mainly of metagreywacke intercalated with subordinate biotite schist. Thin (1-3 cm) leucosomes can be traced from the host rock into a megacrystic, biotite-bearing leucogranite dike (PK090B). The dike appears to cut the hinge of the folded gneiss (Fig. 4.5b). PK090C is

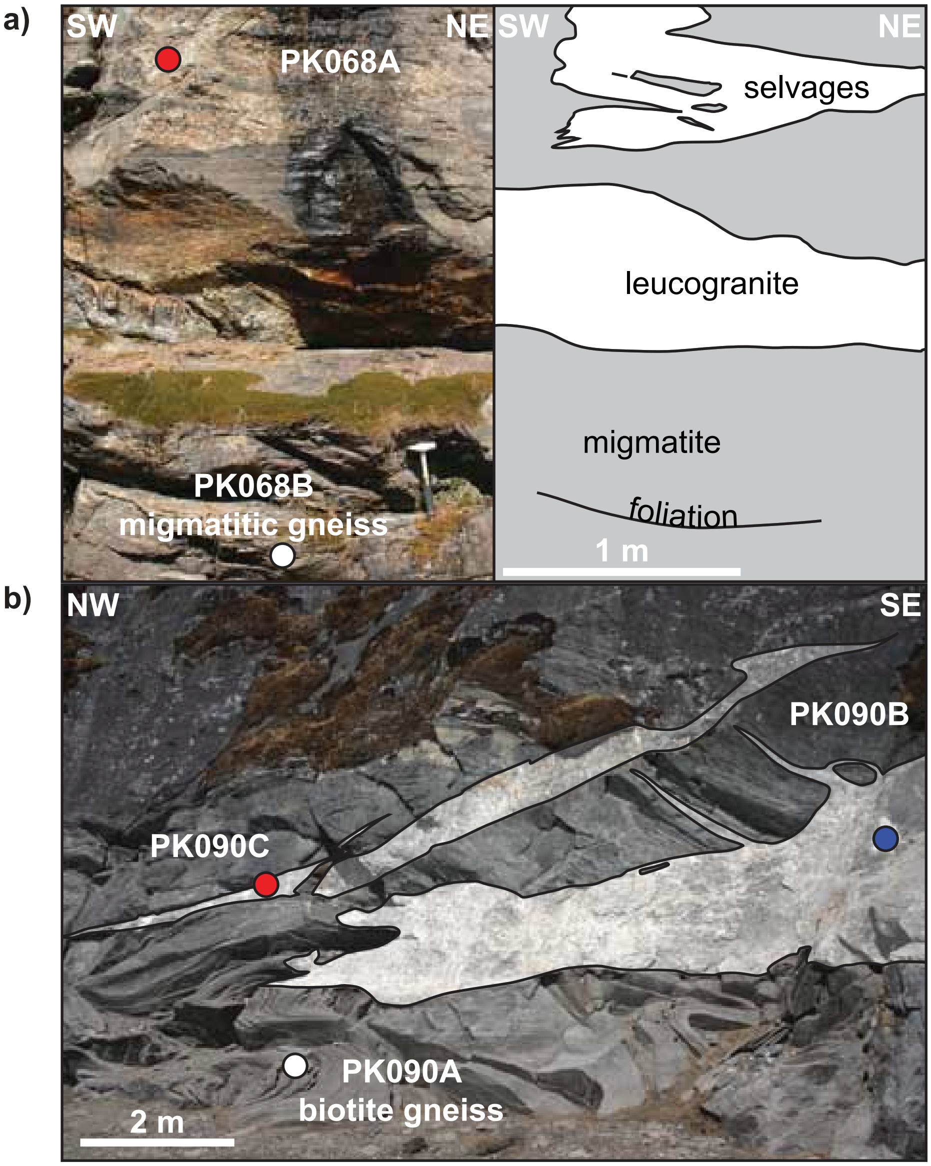

Figure 3.5 Field photographs of GHS leucogranites. **a)** Migmatitic gneiss (PK068B) is intruded by a massive leucogranite (PK068A) south of Namche Bazaar, incorporating selvages of the host gneiss. **b)** Two generations of massive leucogranites (PK090B and PK090C) intrude pervasively deformed biotite gneiss (PK090A) near Dudh Kund.

a garnet, tourmaline, and biotite-bearing leucogranite that obliquely cuts the host-rock foliation, but does not intersect PK090B.

3.4.2 U-Th/Pb and trace element analysis results

3.4.2.1 MCT zone orthogneiss

CL images from orthogneiss thin sections demonstrate metamictization and mechanical fracturing of most in situ zircon (Fig. 3.6a). Zircons with dark CL yield high-U concentrations and are metamict, whereas bright CL grains and cores are crystalline zircon. Bulk rock samples were crushed and separated to recover many (n > 100) euhedral grains with magmatic textures. All ranges of CL intensity were targeted in order to capture the variability contained in each sample as well as inherited signals. In general, orthogneiss analyses yield similar discordia arrays with upper intercepts of ~1800 Ma and lower intercepts indicative of recent Pb-loss (Fig. 3.6b). 1800 Ma zircon occurs as whole grains and magmatic overgrowths on the bright CL cores. Analyses of these cores do not define a discordia array and indicate inheritance from a variety of sources ranging in age from 2000-3600 Ma. The lower intercept corresponding to the date of Pb loss is poorly constrained, and is anchored to 0 Ma in order to calculate upper intercept ages.

In contrast to zircon dates from MCT orthogneiss samples, monazites in paragneisses from the MCT and overlying GHS yield exclusively Tertiary dates (Table 3.1). PK012 contains allanite rims surrounding monazite cores in a reaction texture where monazite is replaced by a thorite and LREE-rich allanite (Fig. 3.7). Monazite and allanite from this sample were analyzed for (U-Th)/Pb and trace elements via LASS-ICPMS. Monazite dates are considerably older than overlying GHS rocks and range from 27.9 to

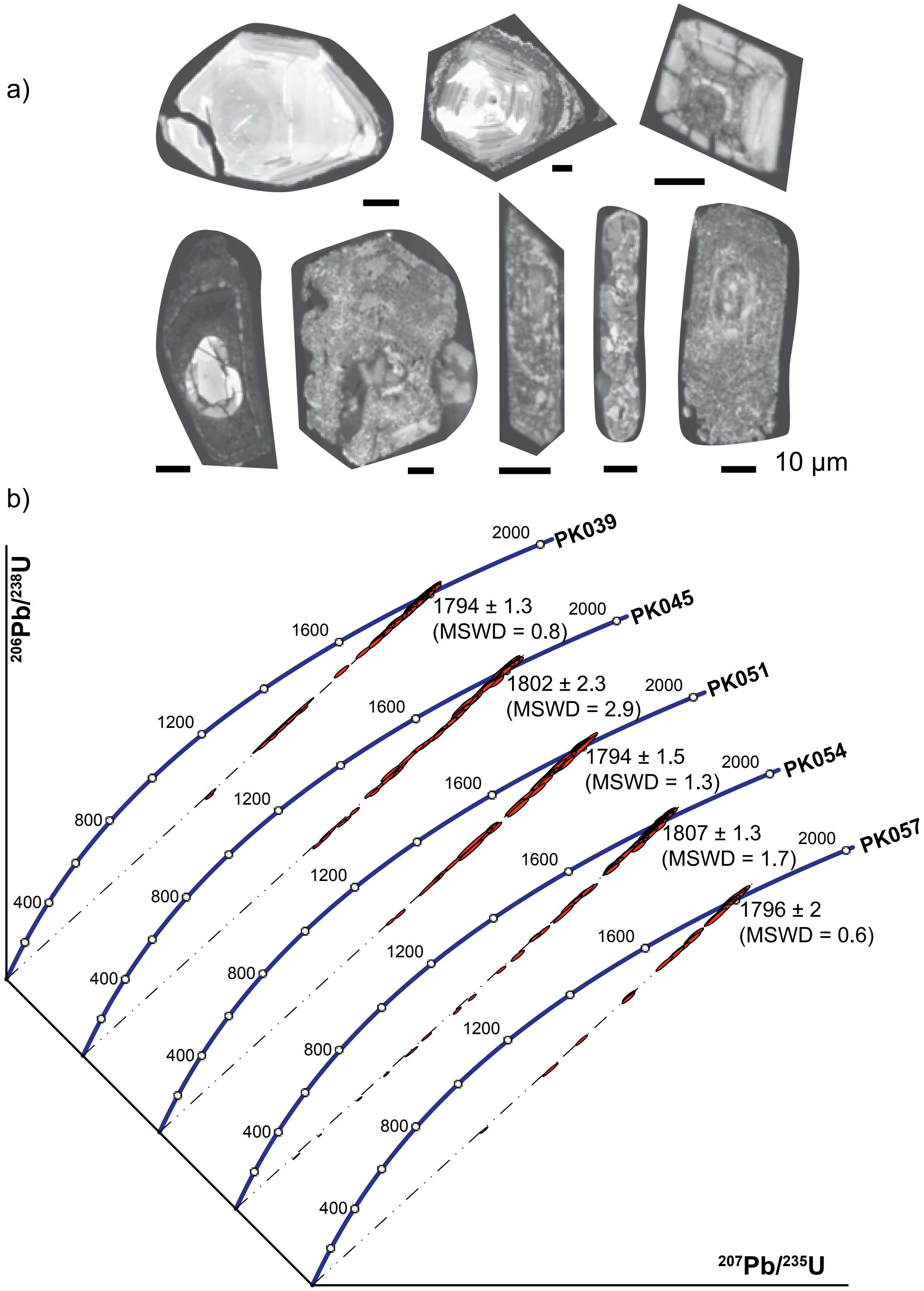

Figure 3.6 a) Cathodoluminescence (CL) images of MCT zone orthogneiss zircons display textures ranging from entirely crystalline to metamict. **b)** Zircon U/Pb geochronology results from orthogneiss samples show evidence for recent Pb-loss, likely associated with the degree of metamictization. Upper intercept ages, anchored to modern day Pb loss are shown.

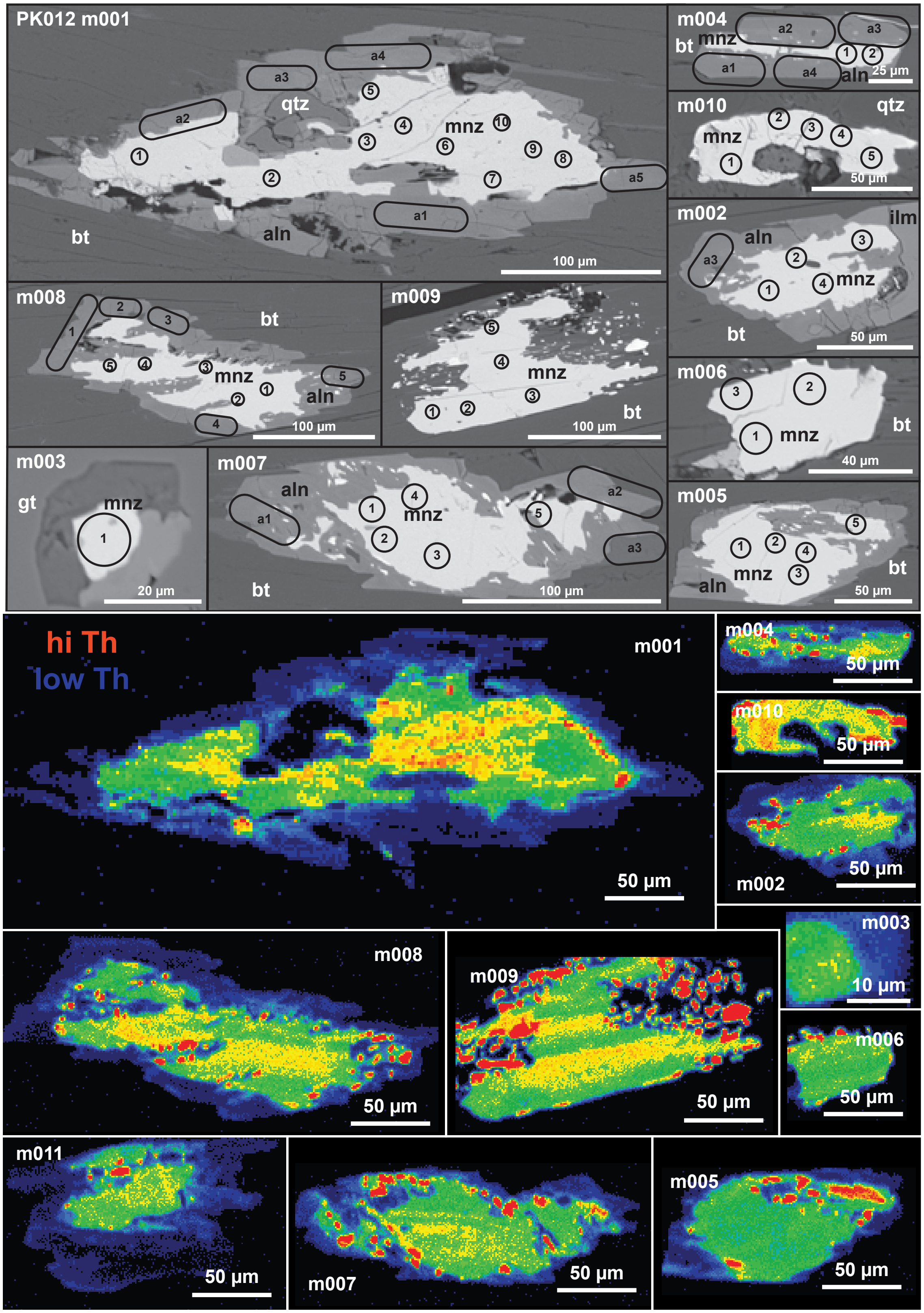

Figure 3.7 Back-scattered electron (BSE) images and Th X-ray maps of PK012; mnz, monazite; aln, allanite; bt, biotite; ilm, ilmenite.

23.5 Ma (Fig. 3.8a). Analyses of allanite rims yield a linear array from an upper intercept of 4976 ± 30 Ma to a lower intercept of 13.3 ± 1.9 Ma (MSWD = 2.2). The data indicate mixing between common Pb (upper intercept) and timing of monazite breakdown/allanite growth (lower intercept) (Fig. 3.8b).

Kyanite bearing gneiss (PK016A) from structurally above the MCT zone position yields monazite ^{208}Pb/^{232}Th dates ranging from 21.6 to 13.9 Ma (Fig. 3.8a). From the structurally highest position above the MCT zone, migmatitic gneiss (PK080) yields dates from 19.4 to 15.5 Ma (Fig. 3.8a). Monazite ages from both samples do not overlap with ages from the structurally lower PK012.

3.4.2.2 Mahabharat granites

CL imaging of zircons from PK200B reveal complex internal zoning including igneous oscillatory zoning, cores with igneous rims, and cores with dark CL overgrowths (Fig. 3.9a). Inherited zircon cores yield concordant analyses ranging from 600-1400 Ma. The igneous grains and overgrowths define a linear array with an upper intercept of 482 ± 3 Ma and a lower intercept of 24 ± 0.8 Ma (MSWD = 0.8; Fig. 3.9b).

X-ray maps of six monazite grains reveal distinct core/rim textures and oscillatory zoning, whereas xenotime is euhedral and homogeneous in fairly homogenous in composition (Fig. 3.10a). Y concentration in monazite varies from 12,000 to 24,000 ppm, whereas xenotime contains 20-25 wt. % Y. Monazite grains yield ^{208}Pb/^{232}Th ages ranging from 22-26 Ma (Fig. 3.10b). Within individual grains, age trends correlate spatially from core to rim (Fig. 3.10a), indicating protracted monazite growth during this period. The xenotime yields a ^{206}Pb/^{238}U date of 18.6 ± 0.2 Ma (MSWD = 1.5).

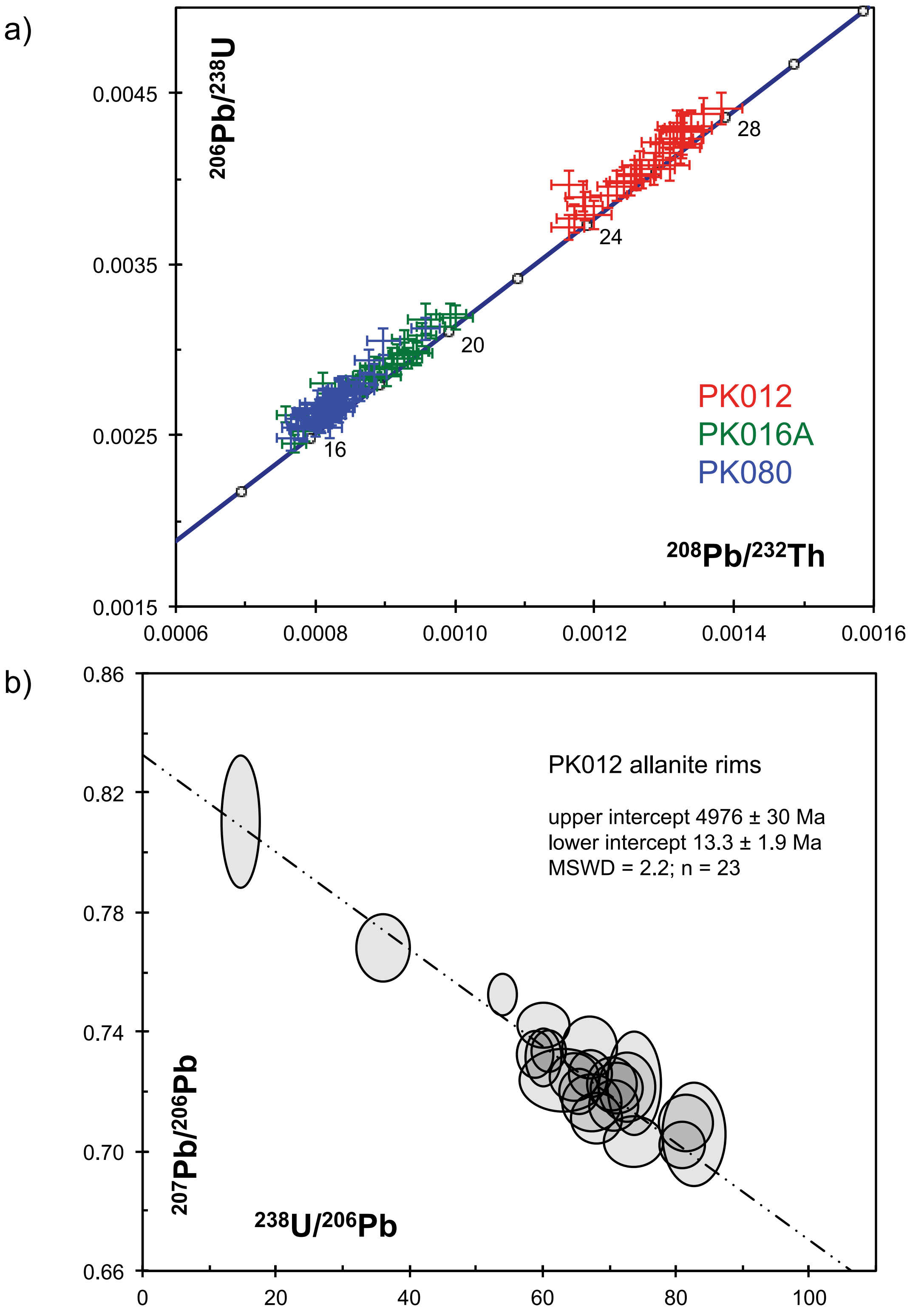

Figure 3.8 a) Modified concordia diagram of metamorphic monazite from GHS paragneisses above the MCT zone. **b)** Tera-Wasserburg concordia diagram of PK012 allanite rims.

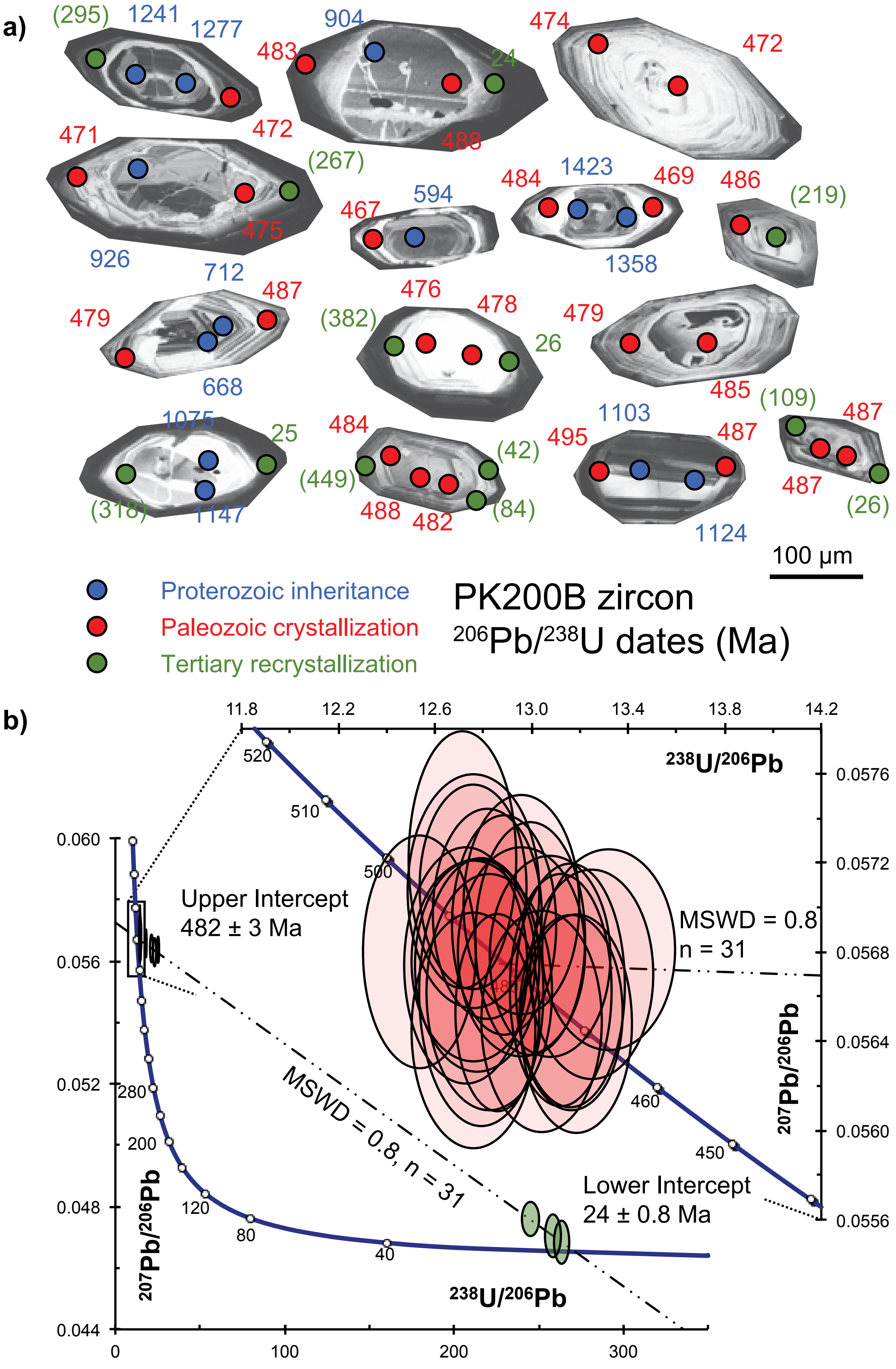

Figure 3.9 a) CL images of zircon from PK200B with spot analyses. **b)** Zircons define a linear array between Paleozoic igneous crystallization and Tertiary overgrowths.

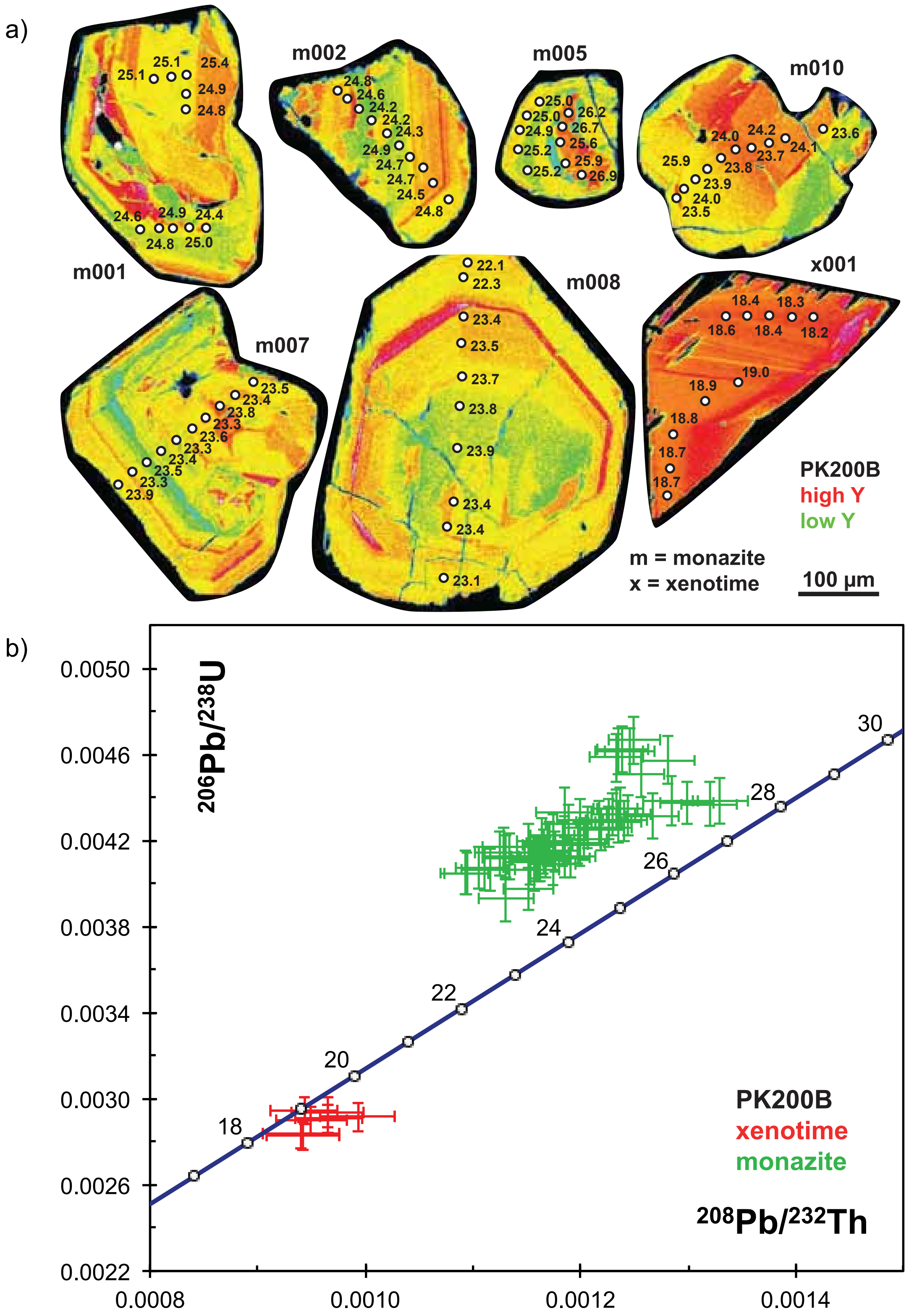

Figure 3.10 a) X-ray maps of Y distribution in one xenotime and six monazite grains from sample PK200B. Monazite maps are scaled similarly and range from 12,000 to 24,000 ppm Y; xenotime contains 200,000 to 250,000 ppm Y. LASS-ICPMS pit diameters are 10 µm; monazite ^{208}Pb/^{232}Th ages and xenotime ^{206}Pb/^{238}U ages have uncertainties of ± 0.5 Ma. **b)** Modified concordia diagram shows protracted crystallization of monazite.

CL imaging of PK233 reveals zircons with clear core/rim zoning textures (Fig. 3.11). Rim analyses yield ^{206}Pb/^{238}U dates ranging from 28-22 Ma, whereas core analyses indicate inheritance from 600-1800 Ma.

PK201A zircon and yields a linear array with an upper intercept of 490 ± 12 Ma and a poorly defined lower intercept of 27.3 ± 1.6 Ma (MSWD = 16). Because of the high MSWD, these data represent ternary mixing between upper intercept of ~480 Ma, and lower intercepts ranging from 36-20 Ma. Inherited zircon cores yield concordant dates ranging from 640-2200 Ma.

PK203B ^{206}Pb/^{238}U zircon dates range from 465-510 Ma with no evidence for Miocene recrystallization. A subset of 17 analyses yield a well defined concordia age of 480 ± 1.4 Ma (MSWD 0.8; Fig. 3.12a). Three monazite grains from PK203B were analyzed, each having a distinct U-Th/Pb isotopic composition. Analyses of grain m001 plots as an array on a Tera-Wasserburg diagram with an upper intercept indicating the presence of common Pb and a lower intercept of 31.5 Ma, whereas grains m002 and m003 plot as distinct clusters with little variation in ^{207}Pb/^{206}Pb. ^{208}Pb/^{232}Th dates define three distinct populations, each recorded by an individual grain: 1) m001 crystallized at 26.0 ± 0.2 Ma (MSWD = 1.3), 2) m002 crystallized at 29.5 ± 0.2 Ma (MSWD = 0.5), and 3) m003 crystallized at 22.3 ± 0.1 Ma (MSWD = 0.4). X-ray maps reveal complex, patchy zoning in m001 whereas m002 and m003 have more distinct domains of homogenous composition.

PK207B zircons yield ^{206}Pb/^{238}U dates ranging from 465-495 Ma, with minimal evidence for recrystallization at 21-26 Ma, and some inherited grains ranging from 720-940 Ma. 25 analyses yield a concordia age of 478.7 ± 1.3 Ma (MSWD = 0.7; Fig. 3.12b).

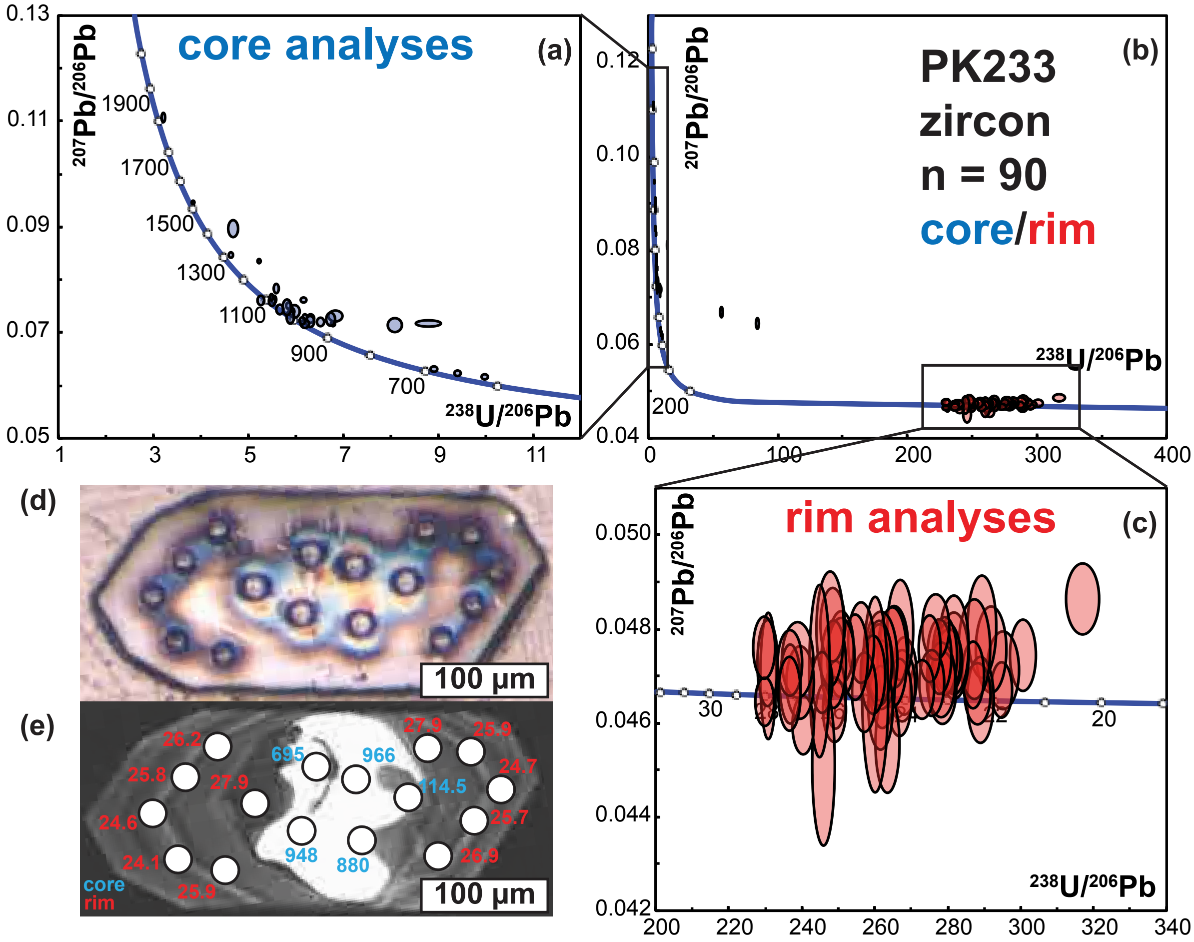

Figure 3.11 Results from U/Pb zircon geochronology of a leucogranite dike exposed in the Mahabharat. **a)** Analyses of PK233 cores range from Neoproterozoic to Paleoproterozoic and likely represent inheritance from a metasedimentary protolith. **b)** Tera-Wasserburg diagram of all data indicates limited mixing between inherited cores and younger magmatic rims. **c)** Rim analyses range from 20 to 28 Ma, suggesting protracted crystallization prior to emplacement. **d)** Photo of a zircon grain with 20 µm diameter laser ablation pits. **e)** Cathodoluminescence (CL) image of the same zircon reveals internal zoning that corresponds to ^{206}Pb/^{238}U ages.

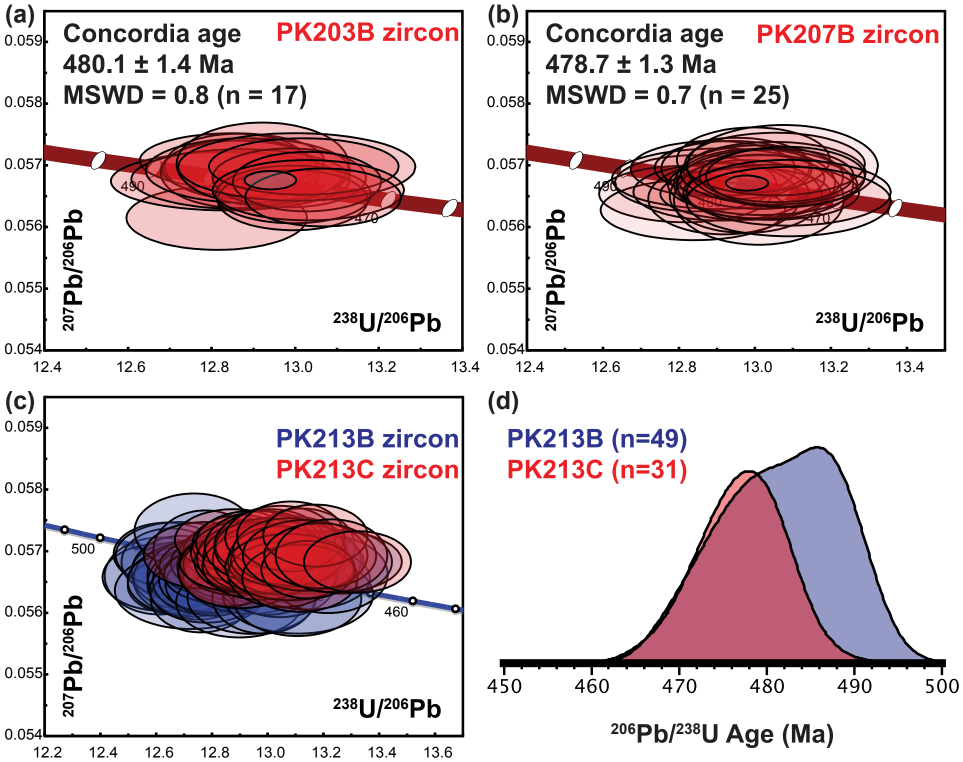

Figure 3.12 Results from U/Pb zircon geochronology of leucogranite dikes exposed in the Mahabharat. Zircons from **a)** PK203B and **b)** PK207B yield concordant Ordovician ages. **c)** Two dikes (PK213B and PK213C) yield overlapping age distributions. **d)** KDE plot of the age distributions demonstrate that PK213B also conatins older ages than PK213C, consistent with field relations.

Zircons from PK213B yield a $^{206}Pb/^{238}U$ date of 482 ± 2 Ma (MSWD = 6.0), with inheritance ranging from 730-1400 Ma. The high MSWD value indicates the zircons do not define a single population. A xenotime grain from PK213B yields a $^{206}Pb/^{238}U$ date of 21.8 ± 0.2 Ma (MSWD = 0.1). X-ray maps demonstrate that spots 1, 2, 6, and 7 analyzed a portion of the grain with evidence for monazite and/or thorite inclusions and were therefore excluded from the weighted mean calculation; the resulting low MSWD value indicates the remaining xenotime analyses from an inclusion-free, homogeneous portion of the grain are equivalent within error.

Zircons from PK213C yield a $^{206}Pb/^{238}U$ date of 478 ± 2 Ma (MSWD = 3.6). The high MSWD value indicates the zircons do not define a single population. Three monazite grains from PK213C were analyzed. Grain m002 and the core of grain m003 (#1-4,6, and 7) are homogeneously high in Th (90,000-110,000 ppm), and yield a $^{208}Pb/^{232}Th$ date of 31.2 ± 0.2 (MSWD = 1.2; n=15). By contrast, grain m001 and the rim of grain m003 exhibit patchy zoning, lower Th concentration (60,000-80,000 ppm) and yield $^{208}Pb/^{232}Th$ dates of 20-16 Ma.

In general, zircons from Mahabharat granites yield Paleozoic igneous crystallization ages of ~480 Ma, with evidence for inherited Proterozoic zircon cores from 640-2000 Ma and Tertiary overgrowths from 36-22 Ma. Monazite and xenotime from the Mahabharat yield exclusively Tertiary dates ranging from 30-19 Ma. Similarly, PK199, the kyanite-garnet schist from the Mahabharat range, yields monazite dates ranging from 35 to 20 Ma.

3.4.2.3 GHS Leucogranites

PK068A contains zircon and monazite permitting analysis of both phases in order to assess the sensitivity of each chronometer to crystallization during melting. Zircon CL images reveal inherited cores, however, analysis of zircon rims yields dates of 22.5 to 20.9 Ma. Monazite grains show clear chemical zoning with Y and HREE enriched rims surrounding low-Y cores along sharp boundaries (Fig. 3.13a). To assess the potential for mixing of chemical domains, three monazites were selected for raster analysis (Fig. 3.13b). Monazite dates range from 22.5 to 18.6 and form a bimodal distributions for targeted sampling as well as raster maps (Fig. 3.13c). The host migmatite (PK068B) yields monazite ages ranging from 34.7 to 23.7 Ma. Similarly, monazite from a migmatitic gneiss sample PK067 yields monazite ^{208}Pb/^{232}Th ages ranging from 34-17 Ma.

Both leucogranite dikes exposed at Dudh Kund contain zircon, however, only the larger dike (PK090B) also contains monazite and xenotime. Two PK090B xenotime grains yield a ^{206}Pb/^{238}U date of 15.8 ± 0.1 (MSWD = 0.7). X-ray maps demonstrate that these grains are homogeneous in composition. Nine monazite grains were analyzed and yield ^{208}Pb/^{232}Th dates of 16.4 to 13.5 Ma X-ray maps reveal complex zoning within these monazite grains which is reflected by the trace element distributions, in particular the heavy rare earth elements. Zircon ^{206}Pb/^{238}U dates range from 16.6 to 14.0 Ma and are correlated with an increasing U/Th ratio through time due to an increase in U concentration from 2,000 and 15,000 ppm, consistent with U/Th partitioning expected from the simultaneous crystallization of zircon and monazite from a melt.

Zircons from PK090C yield ^{206}Pb/^{238}U dates ranging from 16.1 to 15.4 Ma, overlapping in age with PK090B zircon and monazite ages (Fig. 3.14). Zircons from this sample have uniform U/Th ratios of 30-40, however U concentration varies between 500 to 35,000 ppm and Th concentration varies between 200 and 1000 ppm, which is considerably higher than PK090B and may contribute to the green appearance and/or CL

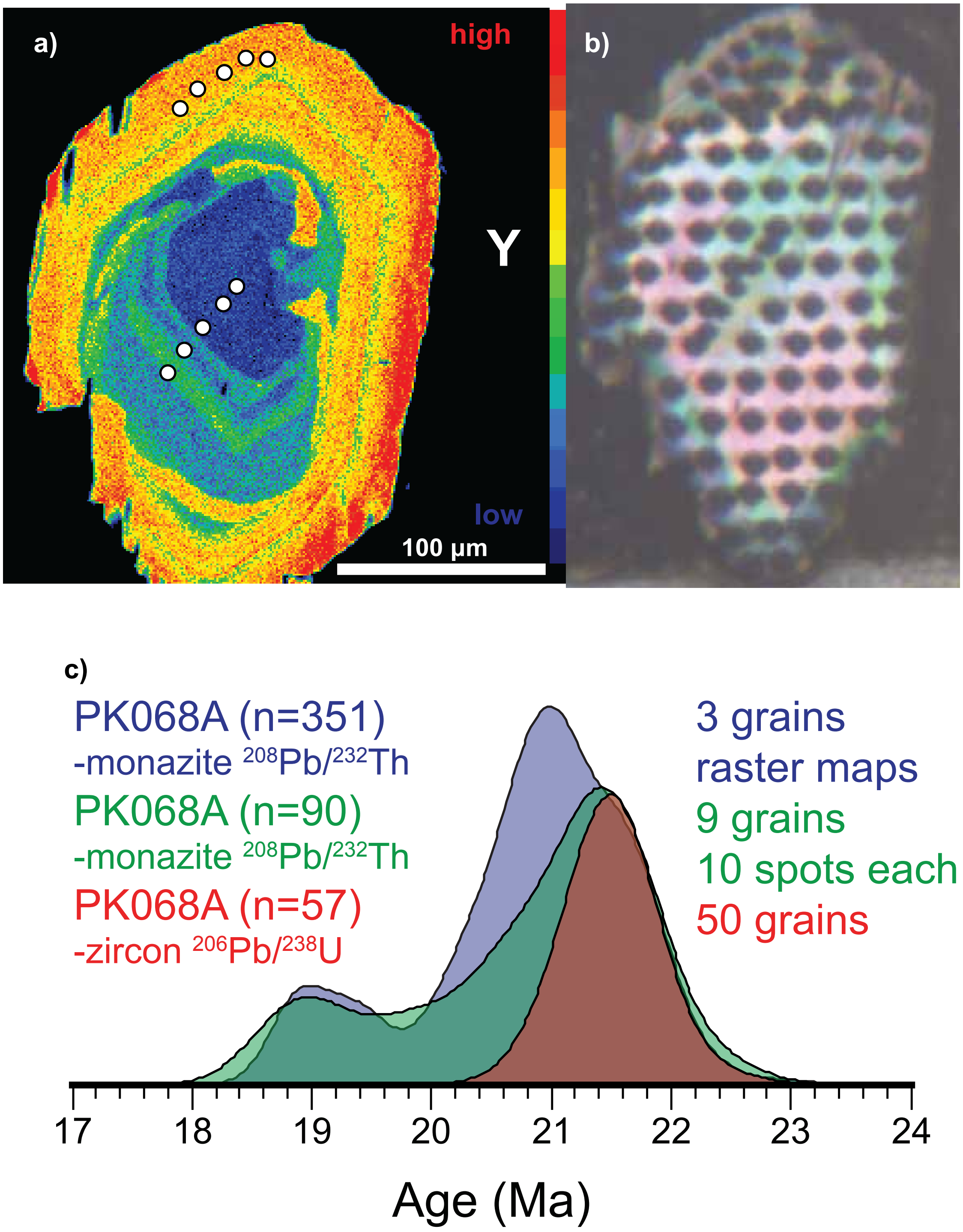

Figure 3.13 a) X-ray map of a typical monazite grain from PK068A with 10 µm ablation pits. Initial analyses targeted low-Y core and high-Y rim domains. **b)** Cross polarized view of the same grain after LASS-ICPMS raster analysis. **c)** KDE plots of zircon and monazite; monazite analyses reveal bimodal distributions.

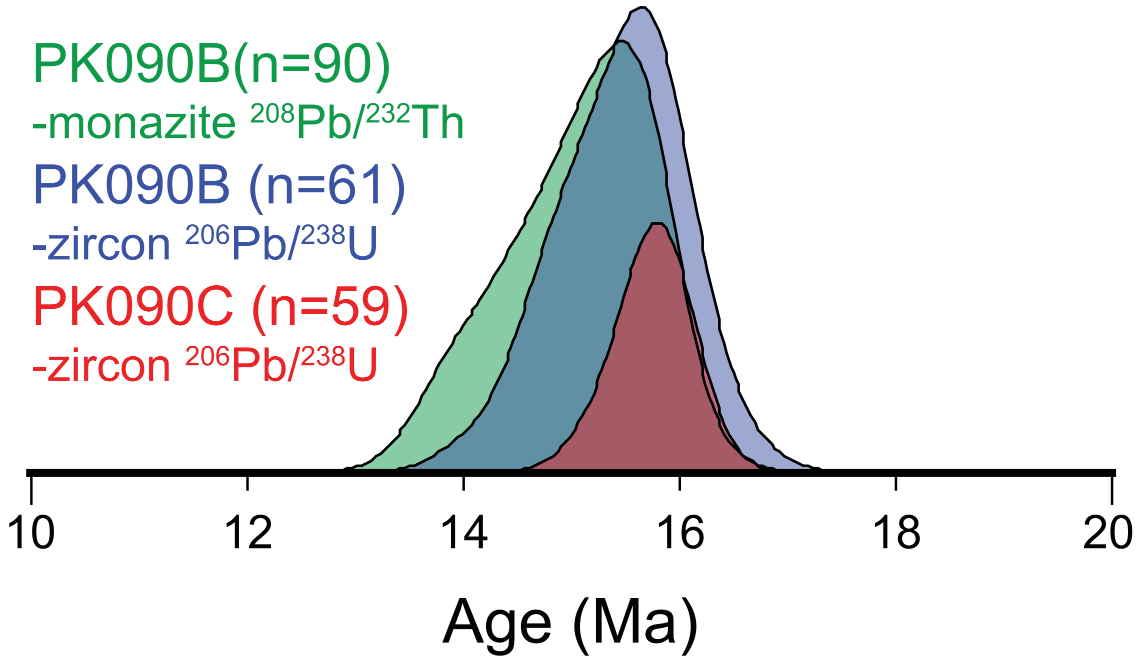

Figure 3.14 KDE plots of zircon and monazite age distributions demonstrate that monazite records later crystallization within the same sample. Zircons from PK090B and PK090C yield overlapping age distributions.

suppression characteristic of zircons from this sample. No monazite or xenotime was recovered from PK090C.

3.5 Discussion

3.5.1 The behavior of accessory phases during metamorphism, deformation, and melting

In order to interpret this dataset involving different phases and processes, a brief discussion of the behavior of zircon, monazite, and xenotime during metamorphism, deformation, and melting is required. Zircon represents the most robust U-Pb geochronometer, and essentially functions as a closed system with regard to retention of Pb at mid-crustal temperatures. Experiments on natural and synthetic zircons demonstrate that diffusion of Pb, U, and Th, and REE is minimal at temperatures below 900ºC (Cherniak and Watson, 2001, 2003). Chemically, zircon is highly refractory, and reacts with the other phases to very limited degree under subsolidus conditions. Furthermore, restitic zircons commonly survive partial melting, due to the low solubility of Zr in melts below 800ºC (Watson and Harrison, 1983; Boehnke et al. 2013). New zircon overgrowths, however, tend to nucleate on inherited zircons and record the time of crystallization from a melt. In general, igneous and metamorphic zircons can be distinguished based on textural relations revealed by CL imaging (Corfu et al. 2003) and by Th/U ratio, with metamorphic zircons generally having lower Th/U ratios (Rubatto, 2002). Pb-loss occurs mainly in metamict (amorphous) zircon with radiation damage accumulated below temperatures of 300-400ºC as a function of time and U content (Meldrum et al. 1998; Cherniak and Watson, 2003). Brittle deformation may enhance Pb-loss by mechanically weakening zircons with radiation damage and exposure to hydrothermal fluids associated with deformation.

In contrast to zircon, monazite is more reactive during moderate to high temperature metamorphism and constitutes a major component of the REE budget in a rock. Monazite chemistry is therefore closely linked to other phases, such as garnet and xenotime for Y and HREE, and apatite and allanite for LREE. Volume diffusion of Pb, Th, U, and REE in monazite is sluggish at temperatures below ~900ºC, and restitic monazite cores are commonly observed in Himalayan leucogranites (Copeland et al. 1988; Harrison, McKeegan, et al. 1995; Harrison et al. 1999). Radiation damage in monazite is annealed at temperatures above 200ºC (Meldrum et al. 1998), meaning the U-Th/Pb system can remain closed even during low-grade metamorphism and deformation. Recrystallization of monazite, however, occurs readily during anatexis, metamorphism, and deformation. Furthermore, monazite breakdown reactions occur at greenschist-facies conditions, resulting in the growth of other REE-bearing phases such as allanite. Diffusion experiments in xenotime indicate similarly high closure temperatures to monazite and zircon in excess 900ºC (Cherniak, 2006). U-Th/Pb systematics in xenotime and monazite, however, are prone to being reset by metamorphic reactions and dissolution/reprecipitation processes mediated by hydrothermal fluids (Watson et al. 1989; Teufel and Heinrich, 1997; Poitrasson et al. 2000; Spear and Pyle, 2002).

3.5.2 Crystallization and deformation of the MCT zone orthogneiss

All of the orthogneiss samples examined in this study yield concordant upper intercept ages of ~1800 Ma with a linear array indicative of recent Pb-loss and minor inheritance. The simplest interpretation of these data is that the orthogneisses share a common Mesoproterozoic granitoid protolith derived from melting of earlier-formed crust, as indicated by Archean inherited zircons. Fabric development and deformation likely occurred due to movement along the MCT zone in Tertiary time, however, the poorly defined lower intercept ages do not constrain when Pb-loss occurred. CL images of in-situ zircons from highly deformed samples exhibit the high degree of metamictization and mechanical weakening of individual zircon grains (Fig 3.7), with no evidence for recrystallization during metamorphism, consistent with brittle deformation under greenschist-facies conditions. Furthermore, no monazite or xenotime indicative of amphibolite-grade metamorphism was recovered from the orthogneiss, however this may reflect the different bulk composition of the granitic protolith, rather than metamorphic P-T conditions.

The Tertiary metamorphic monazite ages from the MCT zone paragneisses stand in stark contrast to the Paleoproterozoic orthogneiss protolith ages. The three samples examined in this study show a progression from older ages (28-24 Ma) just above the MCT zone in the base of the GHS to younger ages (20-16 Ma) in structurally higher sections. The paragneisses occur in the hanging wall of the MCT, and indicate that metamorphic ages of the GHS increase from the hinterland to foreland.

3.5.3 Mahabharat granite crystallization and alteration

The Mahabharat granites record a detailed history of melting and metamorphism of the Himalayan middle crust. Whereas higher temperatures and a greater degree of melt production resulted from subduction and exhumation of the Indian plate in the hinterland of the orogen, the crystalline thrust sheet of the Mahabharat in the foreland of the orogen experienced a much smaller degree of melting and is overprinted by lower-temperature metamorphism.

Dates obtained from the Mahabharat granites may be interpreted in two ways: 1) the granites were emplaced and crystallized in the Ordovician (~480 Ma), retaining inherited zircon cores from their metasedimentary protolith, and were overprinted by Tertiary deformation and metamorphism, or 2) melts were generated and emplaced during the Tertiary, carrying with them ~460-500 Ma inherited zircons. The first hypothesis is favored for the following reasons. In the Mahabharat granites, zircon cores are inherited from metasedimentary source rocks whereas zircon rims record the crystallization of the leucogranite around 480 Ma. Further evidence that zircon ages record emplacement is given by the preservation of cross-cutting relations in PK213B and PK213C, as well as the development of foliation and rotation parallel to the host rock foliation in each of these outcrops (Fig. 3.4). Monazite and xenotime, and rare zircon overgrowths, however, record protracted recrystallization coincident with Himalayan metamorphism and associated deformation. Monazite ages range from 30 Ma to 19 Ma, and overlap with zircon rim crystallization ages; for example PK233 clearly shows crystallization of young, high-U zircon rims. In addition to the apparently igneous zircon rims of PK233, a few high-U Tertiary zircon overgrowths were observed among the Mahabharat granites. The fact that monazite and xenotime record crystallization during the Tertiary suggest that the Mahabharat granites and host rocks experienced high grade metamorphism during the Himalayan orogeny with P-T paths similar to the GHS exposed north of the MCT. Magmatic textures in zircon and monazite grains also imply that melting occurred among the Mahabharat gneisses, extending evidence for Tertiary melting farther into the foreland than previously recognized. If the ages of melting from sample PK233 are representative of the Mahabharat in general, then it may be hypothesized that melting in this part of the GHS is broadly contemporaneous with melting elsewhere in the GHS, however, the absence of ages <22 Ma perhaps indicate that anatexis of the underlying source rocks had ceased in this part of the GHS thrust sheet by the late Oligocene.

3.5.4 Crystallization of GHS Leucogranites.

In contrast to the granites of the Mahabharat, zircon and monazite in GHS granites record voluminous melting of sillimanite-grade metapelites. Within the migmatitic portion of the GHS, the melting history has not been overprinted by later metamorphism, allowing for detailed comparison between intrusion ages of different leucogranite bodies. For example, zircons from two rocks sampled at the same outcrop appear to record complimentary zircon crystallization histories. PK090B contains low-Th, high U/Th ratio zircon compared to PK090C, which contains high-Th zircons. Furthermore, PK090B contains both monazite and xenotime, whereas PK090C contains neither. The U/Th partitioning behavior of these phases is consistent with coeval crystallization of zircon and monazite from a melt. The ages obtained for all phases are indistinguishable within uncertainty, and also display evidence for protracted crystallization.

Similarly, the range in $^{208}Pb/^{232}Th$ ages observed in PK068A monazite may be explained by protracted crystallization. Late magmatic crystallization of high-Y monazite rims as overgrowths on early-crystallized low-Y monazite cores occurred at 19 ± 0.5 Ma (Fig. 3.13). Monazite cores record crystallization over a longer duration, from 22.5 to 20 Ma, younger than the 35 to 24 Ma ages recorded in the host migmatite. A nearby migmatite yields dates of 34 to 17 Ma, overlapping the range of the host migmatite and the leucogranites. To resolve whether the continuous distribution in ages observed in the leucogranite monazites represents mixed sampling of different proportions of core and rim domains or protracted crystallization, raster maps of three grains were compared to targeted analysis of core and rim domains. Both techniques yield a bimodal distribution corresponding to core growth followed by rim growth. There is no hiatus, however, between core and rim growth, suggesting that monazite crystallized throughout 22.5 to 18.6. Zircons record protracted crystallization from 22.5 to 20.9 Ma, but do not record the younger phase of monazite crystallization. The contrasting chemical domains composition of the low-Y cores and high-Y rims indicates a change in melt chemistry. The sharp contacts between core and rim domains (Fig. 3.13a) suggest that some dissolution of the monazite cores occurred prior to crystallization of the rim, and potentially explains the paucity of intermediate ages. While the cause of changes in chemical composition cannot be linked to a specific phase, infiltration of a higher T, monazite, undersaturated melt may explain the core rim relationships. Alternatively, the rim ages may indicate the emplacement age of the leucogranite whereas the core represents early igneous monazite growth prior to melt migration.

3.6 Conclusions

The evidence for Oligo-Miocene leucogranite generation and emplacement as well as the record of metamorphism from 22-30 Ma indicates that rocks exposed in the Mahabharat share a similar thermal history and chronology with other parts of the GHS. This favors the tectonic interpretation of a single GHS thrust sheet overlying the MCT zone and underlying LHS exposed in the Ramechap window.

The MCT zone orthogneisses exposed in the Ramechap window share a common ~1800 Ma protolith and display evidence for recent Pb-loss, likely associated with MCT deformation. The Mahabharat granites indicate 470-480 Ma crystallization ages with evidence for inheritance of detrital zircons, consistent with crustal derivation from melting of metasedimentary protoliths during a Paleozoic orogenic event recognized elsewhere in the Himalaya.

Furthermore, this study highlights the value of analyzing multiple accessory phases that serve as chronometers of different processes. For example, analysis of zircon by U-Pb would have missed the information on subsequent metamorphism in the Mahabharat recorded by monazite and xenotime. Monazite is also more likely to record igneous crystallization from a minimum-temperature melt. The high-spatial resolution of LA-MC-ICPMS and capability to simultaneously measure trace element abundances permit analysis of complexly zoned mineral phases and campaign-style petrochronology.

4. Linking the generation and emplacement of the Manaslu pluton to its source

4.1 Abstract

The Manaslu granite of central Nepal is one of the best-studied leucogranite plutons in the Himalaya. Previous studies involving field mapping, structural analysis, bulk and trace element geochemistry, isotopic analysis of O, Sr, and Nd, as well as Rb/Sr, Sm/Nd, and (U-Th)/Pb geochronology have produced a wealth of information regarding the source, generation, and assembly of the composite body. This study exploits the well constrained structural and petrogenetic framework of the Manaslu region and employs combined (U-Th)/Pb and trace element monazite petrochronology to resolve the spatiotemporal relationships of leucogranites from within the Greater Himalayan Sequence (GHS) source, through the injection complex transport network, and into the main granite body. A preliminary dataset consisting of over 3000 LASS-ICPMS individual monazite spot analyses from 58 granite samples expands the existing age dataset by a factor of 10 and indicates complex internal trace element zoning that corresponds to intra-sample age variation within and between individual monazite grains. ^{208}Pb/^{232}Th ages range from 15-24 Ma with evidence for monazite inherited from earlier metamorphism and/or magmatism (17-36 Ma) as well as from Cambro-Ordovician (450-490 Ma) protoliths. While broadly consistent with previous (U-Th)/Pb studies, this dataset reveals a previously unrecognized 15-18 Ma pulse of granite magmatism that coincides with metamorphic monazite ages in the upper GHS. Furthermore, late stage magmatism is identified in only the source region and injection complex, but not in the main granite body, indicating limited melt transport after 18 Ma. Monazite crystallization

ages provide support for a model involving semi-continuous melt production in the source region punctuated by 1-2 m.y. pulses of magma transport and granite emplacement.

4.2 Introduction

Leucogranites within the Greater Himalayan Sequence (GHS) provide an opportunity to investigate the products of crustal anatexis within a well-constrained tectonic framework and assess the timescales associated with melting processes. Numerical modeling (Harris et al. 2000; Annen et al. 2006) suggests that melt transport and emplacement occur over short timescales (<100 k.y.), whereas melt generation occurs over much longer timescales (>1 m.y.). Further geologic evidence for the dichotomy between in situ, near source processes (melt generation and segregation) and ex situ processes (transport and emplacement) is required to test two hypotheses: 1) melt persists in the crust for long periods of time (>1 m.y.); and 2) emplacement of granites occurs rapidly (<100 k.y.). Knowledge of the timescales required for melt generation and granite emplacement is essential for evaluating geodynamic models involving mid-crustal crustal flow.

The Manaslu intrusive complex consists of pluton as well as a network of dikes and sills injected into host gneisses of the GHS. The pluton has been the subject of several studies, whereas the injection complex has received comparatively less attention. This study attempts to better define the relationship between the pluton, the injection complex, the host gneisses of the GHS, and major orogenic structures through the investigation of monazite crystallization ages and address several key questions and regarding its formation. Is the pluton a composite body of formed by the injection of multiple small batches of melt? Did emplacement occur in pulses separated by gaps, or was it continuous? Do monazite inheritance patterns indicate protracted melting of a single source or mixing of heterogeneous sources?

4.2.1 Granites of the Greater Himalayan Series

The GHS is characterized by pervasive evidence of melting at every observable scale, from in-situ leucosome segregations within migmatitic gneisses, to m-scale leucogranite dikes in injection complexes and km-scale plutons that form many of the highest Himalayan peaks. Granites occur throughout the GHS, however, evidence for melt generation and migration spatially correlates with structural position and metamorphic grade. At the base of the GHS inverted metamorphic sequence in the immediate hanging wall of the Main Central thrust (MCT) melt segregations and leucogranites are rare or absent, occurring mainly up structural section of the kyanite isograd and becoming voluminous above the sillimanite isograd (Le Fort, 1975; Larson et al. 2010; Searle et al. 2010; Larson et al. 2011; Searle, 2013). Among the sillimanite-grade rocks of the upper GHS, pervasive in-situ melt and stromatic migmatites connect into a network of leucogranite dikes and sills. Several phases of granite emplacement are distinguishable based on textures and field relationships. Early dikes and sills are macroscopically deformed, with boudinaged necks and fabric development defined by micas aligned parallel to the host rock foliation, whereas late bodies cut across earlier fabrics. At the top of the GHS, enormous (1 to 10-km-thick) sill-like plutons occur in the footwall of the South Tibetan Detachment (STD), consisting of massive granite with textural evidence for polyphase intrusion and granite emplacement. Exhumation of the GHS accommodated by normal-sense top-to-the-north movement along the STD and reverse-sense top-to-the-south movement along the Main Central thrust (MCT) has exposed granites in the structurally lower migmatites, the intermediate injection complex, and the structurally higher pluton in the Manaslu region.

4.2.2 Geologic setting of the Manaslu granite

The Manaslu pluton consists of a gently NE-dipping lenticular sheet of leucogranite with a maximum thickness of 10 km, an exposed area of 400 km^2 and an estimated volume of 3000 km^3 (Fig. 4.1; Le Fort et al. 1987; Guillot and Le Fort, 1995; Harris et al. 2000; Annen et al. 2006). Like many other leucogranite plutons in the Himalaya, it occurs at the interface between high-grade rocks of the GHS and relatively unmetamorphosed rocks of the Tibetan sedimentary series (TSS). The GHS in the Manaslu region consists of interlayered metapelite and metagreywacke paragneisses, calc-silicate gneiss, quartzo-feldspathic augen orthogneiss, and metamorphosed Paleozoic carbonates, whereas the TSS consists mainly of Paleozoic through Mesozoic sedimentary rocks (Fig. 4.1; Colchen et al. 1986). Peak P-T estimates for the GHS vary with structural position, ranging from 5-10 kbar and 500-750ºC. The TSS, by contrast, is weakly to non-metamorphosed, except for limited metamorphism in close proximity to the Manaslu granite contact (Guillot et al. 1995).

The GHS is pervasively deformed with a consistent north-dipping foliation and evidence for top-to-the south displacement at its base transitioning to top-to-the-north displacement at structurally higher positions (Larson et al. 2010). The TSS, by contrast, displays original sedimentary bedding deformed by north-verging folds (Colchen et al. 1986; Searle and Godin, 2003). Early mapping recognized the transition from high-temperature ductile fabrics in the GHS and to low-temperature folds in the TSS exposed

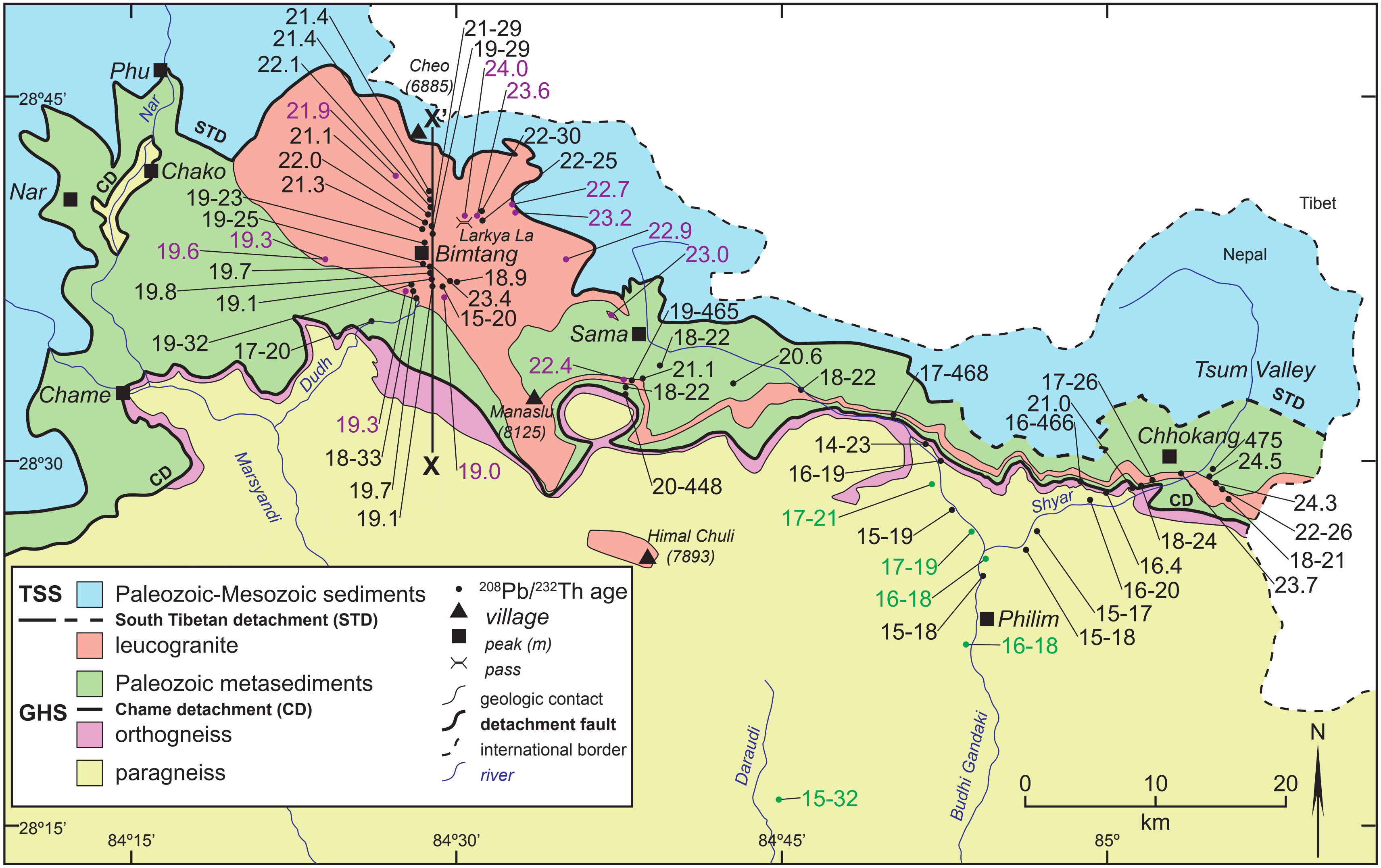

Figure 4.1 Geologic Map of the Manaslu region with ^{208}Pb/^{232}Th ages from this study in black, Harrison et al. (1999) in violet, and Larson et al. (2011) in green. GHS, Greater Himalayan Sequence; TSS, Tibetan sedimentary series.

in the Manaslu region (Colchen et al. 1986), however the contact between the lower Paleozoic calc-silicate gneisses and overlying upper Paleozoic to Mesozoic strata was reportedly stratigraphic (Fuchs and Paudel, 1998). More recently, several workers have noted structural discontinuities occurring within the GHS at the interface between augen gneiss and calc-silicate gneisses (North Himalayan Fault of Harrison et al. 1995; Chame detachment of Searle and Godin, 2003) and between metamorphosed Paleozoic calc-silicates of the GHS and overlying sediments of the TSS (Phu detachment of Searle and Godin, 2003). Both structures record top-to-the-north displacement, and represent the lower, ductile shear zone and upper brittle detachment of the STD. The base of the pluton is structurally concordant with the surrounding GHS gneisses, however the top contact of the pluton has been interpreted in two ways. Early mapping shows the Manaslu pluton intruding the overlying TSS (Le Fort, 1975, 1981; Colchen et al. 1986; Guillot et al. 1993, 1995), however, recent interpretations suggest the granite is entirely within the GHS and does not cut across the upper brittle STD (Searle and Godin, 2003; Larson et al. 2010, 2011).

4.2.3 Injection complex

An injection complex composed of leucogranite, aplite, and pegmatite dikes is well exposed in Nar Valley west of the Manaslu pluton as well as along the Budhi Gandaki and in the Tsum Valley east of the pluton (Fig. 4.1). Pervasive leucogranite melts intrude metamorphosed Paleozoic carbonates in the area near Chako above the Chame detachment and below the Phu detachment (STD), and are interpreted to represent a network of leucogranite sills and dikes emanating from the Manaslu pluton emplaced into structurally higher levels of the GHS (Le Fort, 1981; Searle and Godin, 2003).

Extending for ~60 km along the Budhi Gandaki to the ESE of the main plutonic body is a 100- to 500-m-thick sheet of leucogranite referred to as the Chhokang arm (Le Fort, 1981; Colchen et al. 1986). A parallel sheet of augen orthogneiss occurs structurally below the Manaslu granite, and extends into the Tsum Valley (Fig. 4.1). Contrary to the map pattern (Colchen et al. 1986), we observe the Chhokang arm as a discontinuous network of variably deformed dikes intruding paragneisses, augen orthogneiss, and lower Paleozoic calc-silicate gneisses. Previous workers have interpreted the Chhokang arm as emanating from the Manaslu pluton (Le Fort, 1981; Le Fort et al. 1987), as a feeder dike to the Manaslu pluton (Larson et al. 2011), or as a link to the Shisha Pangma pluton exposed ~100 km to the east (Le Fort, 1981).

A similar network of boudinaged granitic dikes oriented sub-parallel to the host rock foliation as well as late dikes that cut host rock foliation and earlier dikes occurs within migmatites exposed at the confluence of the Budhi Gandaki and Shyar Khola structurally below the Chame detachment and augen orthogneiss (Larson et al. 2011). The migmatites consist of in-situ melt and residuum, and have been interpreted as representative of the source rocks for the Manaslu pluton (Le Fort, 1981; Brouand et al. 1990; Barbey et al. 1995, 1996).

4.2.4 Mineralogy and geochemistry

The Manaslu pluton has been the focus of much geochemical research, including U/Pb, Rb/Sr, Sm/Nd radiometric dating as well as bulk rock major and trace elements and Sr, Nd, O and H isotopic analysis (Hamet and Allègre, 1976; Vidal et al. 1982; Schärer et al. 1986; Deniel et al. 1987; France-Lanord et al. 1988; Copeland et al. 1988, 1990; Guillot et al. 1994; Harrison, McKeegan, et al. 1995; Harrison et al. 1999).

The Manaslu leucogranite is remarkably homogeneous in mineralogy, containing on average 30-35% quartz, 35-40% plagioclase (An_{16-6}), 20-25% K-feldspar, 5-10% muscovite (Le Fort 1981). Biotite, tourmaline, and garnet occurs in variable amounts throughout the pluton, although tourmaline is generally absent in the interior of the pluton and locally abundant among aplite and pegmatite dikes and near the margins of the pluton (Le Fort 1981). Zircon, monazite, apatite, and xenotime occur as accessory phases in variable amounts. The main body of leucogranite is heterogeneous with respect to grain size and development of a magmatic foliation defined by aligned biotite and magnetic fabrics (Le Fort, 1981; Guillot et al. 1993). Manaslu leucogranites are characterized by highly enriched $^{87}Sr/^{86}Sr_i$ values (0.725-0.760) as well as radiogenic $^{207}Pb/^{204}Pb$ ratios of 15.7-15.8 (Vidal et al. 1982) and εNd_i values of -16.3 (Allègre and Othman, 1980) indicative of a isotopically heterogeneous crustal source inferred to be the migmatites of the GHS. Rare earth element (REE) patterns of the source migmatites are more enriched than the leucogranites, which can be explained through early crystallization and extraction of a small component of monazite from the melt into the residuum (Vidal et al. 1982). Zircon morphology revealed by cathodoluminescence (CL) imaging confirms the presence of inherited zircon in migmatite leucosomes and in the Manaslu granite, and Sm and Yb concentrations are consistent with fractional crystallization from a monazite-saturated, xenotime-undersaturated melt (Brouand et al. 1990; Barbey et al. 1995).

4.2.5 Geochronology

The Manaslu leucogranite has been the target of several geochronologic studies, including an early application of the Rb/Sr technique (Hamet and Allègre, 1976, 1978) that resulted in age determinations of 29 ± 1 Ma and ~23 Ma. Subsequent investigations (Vidal, 1978; Vidal et al. 1982) demonstrated initial $^{87}Sr/^{86}Sr$ isotopic heterogeneity that precludes isochronous whole-rock Rb/Sr dates, instead arguing that the granite formed between 40 and 23 Ma, and are most likely younger than 26 Ma. Deniel et al. (1987) utilized whole-rock and mineral Rb/Sr isochrons to obtain dates of 18.1 ± 0.5 Ma from the base and 21.3 ± 0.4 Ma from higher in the pluton.

Attempts at accessory phase U-Pb geochronology reveal similarly complex systematics resulting from Pb-loss, inheritance, and/or protracted crystallization. Deniel et al. (1987) obtained a monazite ^{207}Pb/^{235}U date of 25 Ma interpreted as representing crystallization, however, Copeland et al. (1990) reinterpreted this date to represent mixing between a Paleozoic inherited component and a reversely discordant date of ~20 Ma. Ion microprobe ^{208}Pb/^{232}Th analyses with a spatial resolution of 10-15 μm yield dates ranging from 21.5-25.6 Ma, defining a peak crystallization age of 22.4 ± 0.5 Ma with evidence for inheritance as old as 614 Ma for one sample in the Chhokang arm (Harrison et al. 1995). An updated study of 11 additional samples indicates two phases of granite emplacement, consisting of the Larkya La phase 22.9 ± 0.6 Ma and the Bimtang phase 19.3 ±0.3 Ma (Harrison et al. 1999). Further evidence for inheritance is also documented, including Paleozoic ages (450-600 Ma) interpreted to represent protolith ages as well as 35-23 Ma dates interpreted to represent prograde (Eohimalayan) metamorphism and/or early anatexis (Harrison et al. 1999).

Cooling ages for the granite include whole-rock K/Ar dates ranging from 14 to 17 ± 2 Ma (Krummenacher, 1971; Le Fort, 1975) as well as ^{40}Ar/^{39}Ar dates of 18.4 to 13.3 Ma for muscovite, 17.0-14.7 Ma for biotite, and 16.4-3.4 Ma for K-feldspar (Copeland et al. 1990). ^{40}Ar/^{39}Ar analysis of hornblende and mica from the upper contact aureole at the NE margin of the pluton indicate slow cooling through hornblende closure (T_c ~550ºC) by 22-23 Ma followed by rapid cooling through mica closure (T_c ~350º C) at 17.6 ± 0.4 to 18.6 ± 0.4 (Guillot et al. 1994, 1995; but see Harrison, Mahon, et al. 1995).

4.2.6 Models for generation and emplacement of the Manaslu pluton

Models for melt generation in the GHS predict distinct geochemical and geochronologic relationships between the Manaslu granite, its source, and bounding structures of the GHS. In addition to increased radioactive heat production of thickened continental crust, models for leucogranite melt generation involve either 1) fluids, 2) decompression, 3) shear heating, or some combination thereof. Melt generation due to thrusting can be explained either by fluid-fluxed melting of the GHS thrust sheet (Le Fort, 1975, 1981) or by shear heating along the MCT (England et al. 1992; Harrison et al. 1999). The MCT occurs ~60 km south of the Manaslu pluton (Larson et al. 2010), juxtaposing the GHS against underlying low-grade metasedimentary rocks of the Lesser Himalayan Sequence (LHS). Previous workers have attributed the southward transport of the higher temperature GHS rocks along the MCT as the cause for dehydration and release of volatiles (H_2O and CO_2) from the underlying lower temperature LHS (Le Fort et al. 1987; France-Lanord and Le Fort, 1988). In this model, the volatiles fluxed through the GHS, lowering the solidus and initiating partial melting. Shear heating along the MCT may have also facilitated melting of the basal GHS (Le Fort, 1975; England et al. 1992). Both models predict that displacement along the MCT initiated prior to generation and emplacement of the Manaslu granite, and that the age of the granite places a minimum age constraint on the timing of initial MCT movement.

H_2O-fluxed melting of Himalayan metapelitic source rocks at temperatures below 750ºC produces melts of trondhjemitic rather than leucogranitic composition (Patiño Douce and Harris, 1998). By contrast, fluid-absent muscovite dehydration melting during isothermal (750-780ºC) decompression from 8 to 6 kbar is capable of producing >10% melt from fertile metapelitic source rocks (Patiño Douce and Harris, 1998). Zr and REE saturation thermometry indicate melting occurred at temperatures under 730ºC (Copeland et al. 1988; Montel, 1993; Harrison, McKeegan, et al. 1995). The high Rb/Sr ratios of leucogranites relative to the GHS metapelites supports the notion that incongruent melting of muscovite and K-feldspar under fluid-absent conditions represents the dominant process involved in leucogranite production (Harris et al. 1993).

In models involving coeval decompression and melt generation, the emplacement age of the Manaslu granite provides a minimum age estimate for the initiation of exhumation of the GHS through movement along the MCT and/or the STD. A hybrid model involving early decompression melting followed by later higher-temperature (>750ºC) dehydration melting of muscovite of the same source rock via shear heating along the MCT has also been proposed (Harrison et al. 1999).

The top contact of the Manaslu pluton occurs at the interface between the GHS and the overlying TSS (Figs. 4.1, 4.2). Elsewhere in the Himalaya, such as the Everest region (Cottle et al. 2009) this contact is identified as the South Tibetan Detachment (STD), a system of north-dipping, low-angle brittle normal faults and ductile shear zones accommodating southward displacement of the GHS. Three possible relationships between the Manaslu pluton and the STD have been proposed, including: 1) the pluton is cut by the STD and therefore predates it (Searle and Godin, 2003); 2) the pluton cuts across the STD (Guillot et al. 1995; Harrison et al. 1999); or 3) the granite formed contemporaneously with movement along the STD (syn-STD) (Searle and Godin, 2003). Guillot et al. (1995) interpret that the contact between the Manaslu pluton and overlying TSS as intrusive, with a contact aureole developed on the NE margin (i.e. post-STD).

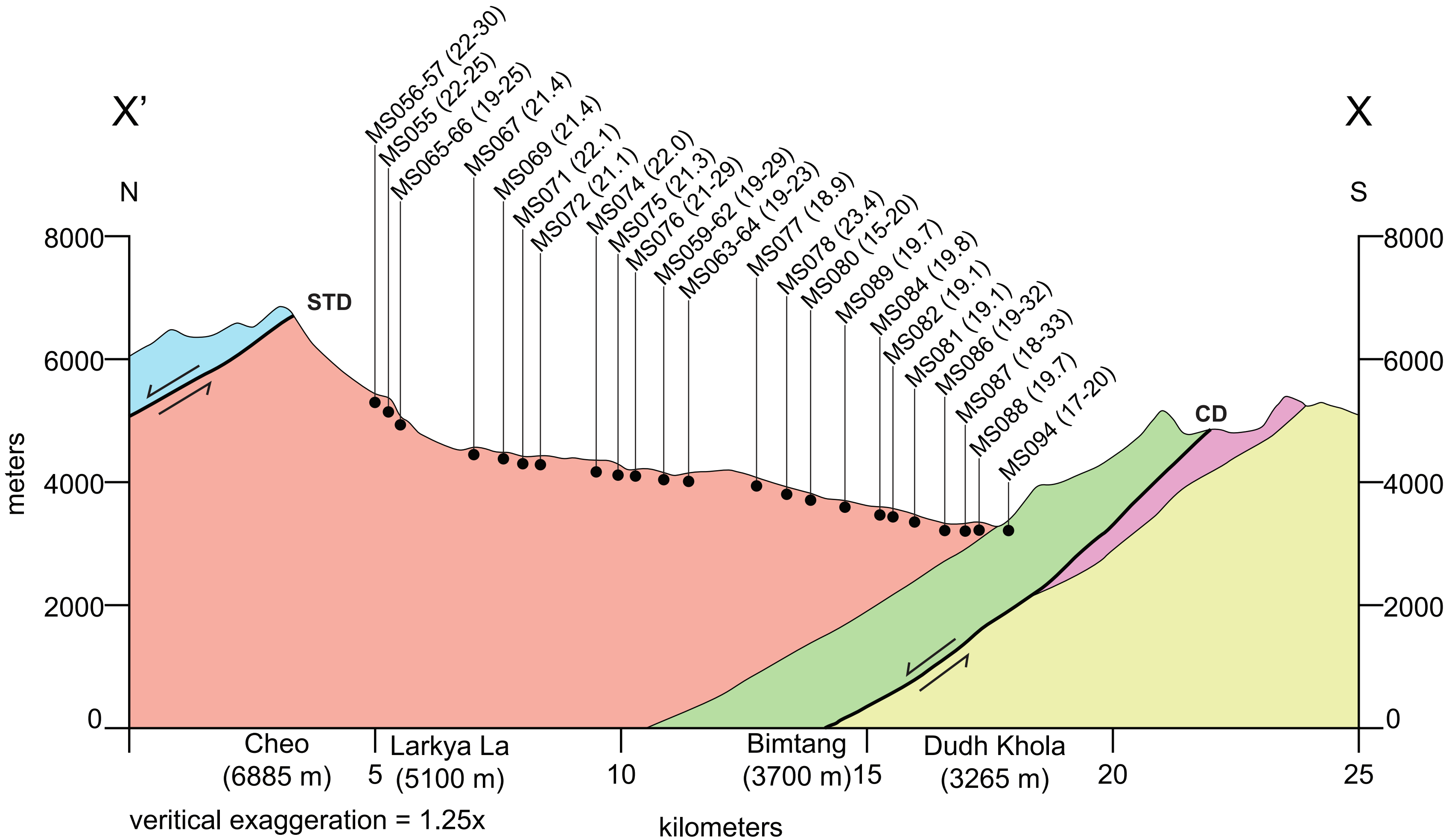

Figure 4.2 Geologic cross section of the Manaslu pluton from X' to X. Colors and symbols identical to geologic map. Sample locations are projected into the line of section and $^{208}Pb/^{232}Th$ ages are given in (Ma).

Later, the recognition of the North Himalayan Fault in the Manaslu region led Harrison et al. (1995, 1999) to interpret the pluton as intruding across the STD, placing a minimum age constraint on its latest kinematic activity at 19-23 Ma (syn-to-late STD). More recently, Searle and Godin (2003) reinterpreted the North Himalayan Fault of Harrison et al. (1995, 1999) as the structurally lower Chame detachment, and report that the top contact of the northwestern portion of the Pluton is cut by the structurally higher Phu detachment segment of STD, implying that the Manaslu pluton formed largely pre-STD, and any metamorphism of the TSS hanging wall rock can be attributed to the thermal input of the hot footwall. Furthermore, distinguishing between the three proposed structural relationships for STD (pre-, post-, or syn-) is further complicated by polyphase intrusive history of the Manaslu pluton.

Three models exists for the emplacement of the Manaslu pluton: 1) emplacement of the entire pluton in one magmatic pulse (Copeland et al. 1990), 2) bimodal emplacement of the pluton in two main pulses (Harrison et al. 1999), or 3) semi-continuous emplacement of over at least 5 m.y. (Deniel et al. 1987, Annen et al, 2006). Heterogeneities in εSr_i values on scales < 10 m indicate that magma mixing by convection was insufficient to homogenize melt batches from different sources and provide evidence that the Manaslu pluton represents an amalgamation of numerous accreted intrusions (Deniel et al. 1987). $^{40}Ar/^{39}Ar$ cooling ages, on the other hand, are consistent with a single crystallization age of 20 Ma (Copeland et al. 1988). Monazite $^{208}Pb/^{232}Th$ ages (n=158) from 12 samples in the Manaslu pluton define distinct age peaks interpreted to represent two phases of crystallization; Larkya La phase at ~22.9 ± 0.6 Ma, followed by a hiatus at ~21 Ma and the Bimtang phase at ~19.3 ± 0.3 Ma (Harrison et al. 1999). Thermal modeling indicates progressive emplacement of 20-60 m thick sills every

20-60 k.y. over a period of 5 m.y. best fits the available P-T-t constraints (Annen et al. 2006).

4.2.7 This study

Knowledge of the timescales involved for the emplacement of the Manaslu pluton is critical for assessing the relationship between the Manaslu pluton, the GHS source, and its bounding structures (the MCT and STD). A comprehensive, campaign-style approach to different phases of the leucogranite pluton is required in order to elucidate the timescales involved in its formation. Crucially, a technique with high spatial and temporal resolution is necessary in order to interpret any dates obtained in their spatial and geochemical context and assess complicating factors such as dissolution/reprecipitation, protracted crystallization, and inheritance. Furthermore, the occurrence of inherited accessory phase minerals (Copeland et al. 1988; Brouand et al. 1990; Barbey et al. 1995; Harrison, McKeegan, et al. 1995; Harrison et al. 1999) provides a record of the earlier melt history of the Manaslu granite and its source rocks through examination of restitic grains unaffected by later igneous crystallization.

This study attempts to resolve competing hypotheses regarding the timing of granite generation and emplacement, namely: 1) granite emplacement occurred in distinct pulses (e.g. Harrison et al. 1999); 2) granite emplacement occurred via continuous emplacement (e.g. Annen et al. 2006); and 3) granite generation occurred continuously in its source. Furthermore, ages presented herein provide important constraints on the timing of decompression, and exhumation of the GHS along orogen-scale structures (the MCT and STD).

4.3 Methods

In contrast to highly refractory zircon, monazite is more reactive in minimum-temperature melts and records new growth during leucogranite crystallization (Parrish, 1990). Monazite U-Th/Pb geochronology has been successfully employed to date granites throughout the Himalaya (Schärer, 1984; Schärer et al. 1986; Deniel et al. 1987; Copeland et al. 1988; Harrison, Mahon, et al. 1995; Harrison et al. 1999; Simpson et al. 2000; Catlos, Gilley, et al. 2002; Viskupic et al. 2005; Cottle et al. 2007; Cottle, Searle, et al. 2009; Larson et al. 2011). Additionally, previous studies have linked trace element distributions in monazite to the chemical conditions present at the time of crystallization (Cocherie et al. 1998; Williams et al. 1999; Zhu and O'Nions, 1999; Kohn et al. 2005; Williams et al. 2007). This study integrates monazite geochronology and geochemistry with field observations and petrologic context of leucogranites exposed in the Manaslu pluton and injection complex.

4.3.1 Sampling strategy

In order to obtain and interpret geochronologic data while preserving its context, samples were selected according to three specific criteria at a variety of scales: 1) km-scale spatial distribution and structural position; 2) m-scale outcrop relations; and 3) µm-scale mineral characteristics. The goal of this sampling strategy is to characterize the melting history of the Manaslu pluton with respect to structural setting, deformation and chemical composition. Crosscutting relations, the degree of fabric development, and the orientation of the intrusive bodies relative to host rock fabrics were documented. A total of 78 samples were collected and prepared for laboratory analysis. Leucogranites range from medium- to very coarse-grained (3-10 mm) and share a peraluminous composition containing K-feldspar + plagioclase + quartz + muscovite ± tourmaline ± biotite ± garnet. Accessory phases include apatite, zircon, monazite, and occasional xenotime or intergrowths of zircon and xenotime. Monazite separates from 3-5 kg granite samples are prepared using standard techniques including crushing, milling, sieving, and separation by density and magnetic susceptibility. Monazite grains are handpicked, mounted in a 2.5 cm epoxy resin discs, and polished to expose approximately equatorial sections through the grains.

Previous investigations have documented the variable presence of monazite among Manaslu granites (Harrison, McKeegan, et al. 1995). Most samples processed using standard mineral separation yield a large number (50-100) of monazite grains, however a subordinate number yielded only a few grains or none at all. While the exact reason for the lack of monazite remains unclear, considering the similar mineralogy and peraluminous composition of these granites, the granites without monazite correlate with calc-silicate host rock lithology's.

4.3.2 EPMA X-ray chemical mapping

Five to ten representative monazite grains from each sample were selected for imaging using a Cameca SX-100 electron probe micro-analyzer (EPMA). X-ray maps are produced using five wavelength-dispersive spectrometers positioned to measure Y (LTAP, Lα), Th (LPET, Mα), and U (LPET, Mα). Analytical protocols consist of 15-20 keV accelerating voltage, 200 nA beam current (equating to a ~1 μm^3 interaction volume), and 25 to 100 ms dwell time. Y serves as a proxy for the behavior of HREE, and U, and Th variation bear directly on the isotopic analyses of these elements. Although qualitative, X-ray maps reveal textural information such as internal zoning patterns and core-rim relationships and aid in targeting specific chemical domains for isotopic analysis. Understanding the distribution of these elements potentially provides important information on the growth history of individual crystals (Williams et al. 1999, 2007; Zhu and O'Nions, 1999; Cocherie et al. 1998; Stepanov et al. 2012).

4.3.3 U-Th/Pb analysis

U-Th/Pb analyses are carried out using a laser ablation split stream inductively coupled plasma mass spectrometer (LASS-ICPMS). Monazites are ablated with a Photon Machines 193 nm ArF Excimer laser, mixed with He carrier gas, and introduced into a Nu Plasma HR multi-collector ICPMS set to measure ^{238}U and ^{232}Th on Faraday cups and ^{208}Pb, ^{207}Pb, ^{206}Pb, and ^{204}Pb + ^{204}Hg on secondary electron multipliers. No correction is made for common Pb due to isobaric interference of ^{204}Hg in the He carrier gas on ^{204}Pb. Ablation pits measure 5-10 µm in diameter with depths of <4 µm. Using X-ray maps, distinct compositional domains, such as cores and rims, are targeted for 5-10 replicate analyses per monazite grain or domain. To assess the possibility of mixing between domains and test the validity of the targeted sampling method to capture the spectrum of variability recorded in monazite grains, 8 monazite grains were selected for detailed raster analysis of the entire exposed surface of the grain. Utilizing a standard-sample bracketing technique, analyses of reference materials with known isotopic compositions are measured before and after each set of ten unknown analyses. Reference materials consist of several monazite grains or fragments with matrices similar to the unknowns and published isotopic ages including “44069” (424 Ma Pb/U ID-TIMS age; Aleinikoff et al. 2006) and “FC-1” (55.7 Ma Pb/U ID-TIMS age; Horstwood et al. 2003).

Data reduction, including corrections for baseline, instrumental drift, mass bias, down-hole fractionation as well as age calculations were carried out using Iolite v. 2.1.2 (Paton et al. 2010). 44069 monazite serves as the primary reference material to monitor and correct for mass bias as well as Pb/U and Pb/Th down-hole fractionation while the remaining two reference materials are treated as unknowns in order to assess accuracy and precision within each run and session. Concordia and weighted mean date plots were calculated in Isoplot v2.4 (Ludwig, 2000) using the ^{238}U, ^{235}U, and ^{232}Th decay constants of Steiger and Jäger (1977). Comparing analyses of secondary reference materials to published ID-TIMS ages indicates a reproducible accuracy of 1-2%.

4.3.4 REE analysis

Trace element data are collected using the same laser system described above and an Agilent 7700S Quadrupole ICPMS. Splitting the stream of He carrier gas into both ICPMS instruments allows for simultaneous collection of REE and U-Th/Pb data from the same ablation pit. Elemental abundances and their uncertainties are calculated using a simple matrix-matched sample-standard bracketing approach in Iolite v. 2.1.2 (Paton et al. 2010) including corrections for baseline and instrumental drift. Reported uncertainties incorporate a component based on the reproducibility of the primary reference material over the analytical session, and are typically <5% for Y and LREE and <10% for HREE.

4.3.5 Rejection criteria and data filtering

The entire dataset of 3060 U-Th/Pb analyses and 3000 trace element analyses was inspected for evidence of inclusions of other phases and/or common Pb contamination.

Optical and Scanning Electron Microscope (SEM) images of monazite grains were compared to X-ray maps to ensure trace element and U-Th/Pb ablation pits fall within targeted chemical domains and analyses located along micro-fractures or grain boundaries were identified. Additionally, simultaneous collection of REE and U-Th/Pb data enabled the identification of inclusions of other phases that were rejected due to the possibility of different ablation characteristics relative to matrix-matched monazite standards and the incorporation of common Pb residing along grain boundaries. 14 analyses with anomalously high Zr, or Y concentrations were identified and interpreted to represent inclusions of zircon, or xenotime. Analyses contaminated with micro-inclusions of Pb-bearing phases, (i.e. K-feldspar, rutile, titanite, or apatite), and/or surface contaminants not removed by pre-ablation shots may contain a small component of common Pb and require alternative means for identification.

Due to a Th/U partition coefficient >1, monazite preferentially incorporates excess ^{230}Th relative to ^{238}U, violating the assumption of secular equilibrium for U-Th/Pb systematics in young monazite (Schärer, 1984). The resulting excess, or unsupported ^{206}Pb common in young igneous monazite precludes the use of conventional concordia diagrams, discordance cutoff filters, or common Pb corrections typically utilized for U-Pb geochronology. The ^{207}Pb/^{235}U ratio is unaffected by excess ^{206}Pb, however, only small amounts of radiogenic ^{207}Pb are measurable in young monazite and therefore is sensitive to the effect of common Pb. ^{208}Pb/^{232}Th dates, on the other hand, are unaffected by excess ^{206}Pb and only slightly affected by common Pb.

In order to ensure ^{208}Pb/^{232}Th dates are free of common Pb and represent the best age estimates for monazite crystallization, analyses indicative of common Pb contamination were excluded. Although no common Pb correction is possible due to the isobaric interference of ^{204}Hg, analyses with high (i.e. > 100 cps) ^{204}Pb resolvable above background ^{204}Pb + ^{204}Hg are excluded from the dataset. Additionally, the ablation profile is inspected for anomalous or abrupt changes in intensity, and based on this three-dimensional assessment, spot analyses that sampled inclusions, grain boundaries, or fractures are excluded from the dataset. Furthermore, ^{207}Pb/^{206}Pb ratios > 0.7 or anomalously higher than analyses of the same grain were used to identify and exclude 139 analyses indicative of common Pb contamination. 61 imprecise analyses with > 5% uncertainty in either ^{206}Pb/^{238}U or ^{208}Pb/^{232}Th were also excluded. In total, < 7% (214 of 3060) U-Th/Pb analyses were excluded from age interpretations for analytical reasons.

To assess the validity of monazite ^{208}Pb/^{232}Th dates, a xenotime grain was selected for raster LASS-ICPMS analysis (n = 68), enabling comparison between ^{208}Pb/^{232}Th and ^{206}Pb/^{238}U dates between monazite and xenotime occurring in the same rock (MS008). Because xenotime preferentially incorporates U rather than Th, it is unaffected by excess ^{206}Pb derived from ^{230}Th, and the extent of ^{230}Th deficits are more limited than ^{230}Th excess due to its low (< 1) partition coefficient (Schärer, 1984). Also, bulk rock REE patterns imply that the leucogranite melts are monazite-saturated and xenotime-undersaturated (Barbey et al. 1995), meaning the occurrence of inherited xenotime is less likely than inherited monazite. Xenotime analyses are normalized to 44069 monazite primary reference material. Repeat analyses of FC-1 xenotime yield ^{206}Pb/^{238}U and ^{208}Pb/^{232}Th dates indistinguishable from FC-1 monazite within uncertainty.

4.4 Results

A total of 2,846 U-Th/Pb and 2,786 trace element analyses were obtained on 320 monazite grains from 58 leucogranites; 27 from the Manaslu pluton and 31 from the injection complex (Figs. 4.3, 4.4). Results are summarized in Table 4.1. A comparison between monazite and xenotime ages is presented in section 4.4.1 and summarized in Fig. 4.5.

^{208}Pb/^{232}Th dates range from 485.9 ± 11.5 Ma to 11.7 ± 0.4 Ma. At the upper end of this range, 87 analyses yield older dates indicative of inheritance or mixing between Paleozoic upper intercepts and Tertiary lower intercepts (Fig. 4.6). At the lower end, 77 analyses yield anomalously young dates in comparison to other analyses from the same sample, and are interpreted to indicate Pb-loss by dissolution/precipitation processes (Fig. 4.7). Additionally, 772 analyses yield dates that are older than other analyses from the same sample, and are interpreted to reflect Tertiary inheritance (Fig. 4.8). The remaining 1910 analyses constitute > 62 % of the entire dataset and are used to calculate the weighted mean age for each sample (Table 4.1).

4.4.1 Monazite/xenotime comparison

To test the validity of ^{208}Pb/^{232}Th monazite dates, a LASS-ICPMS raster map of a euhedral xenotime grain (x007, n = 68) was compared to a raster map (m007, n =7) and targeted analysis of euhedral monazite (m001-m004) from a leucogranite dike (MS008) with relatively simple X-ray patterns and U-Th/Pb behavior (Fig. 4.5). Y maps indicate monazite grains are fairly homogeneous in composition with sector zoning typical of igneous crystallization (Fig. 4.5a). Monazite analyses yield a ^{208}Pb/^{232}Th date of 16.5 ± 0.1 Ma (MSWD = 2.7, n = 89 of 96), with minor dispersion resulting from common Pb and excess ^{206}Pb. Xenotime analyses yield a precise ^{206}Pb/^{238}U date of 16 ± 0.1 (MSWD = 0.5; n = 68 of 68), with older ^{207}Pb/^{206}Pb, ^{207}Pb/^{235}U, ^{208}Pb/^{232}Th, dates. Monazite

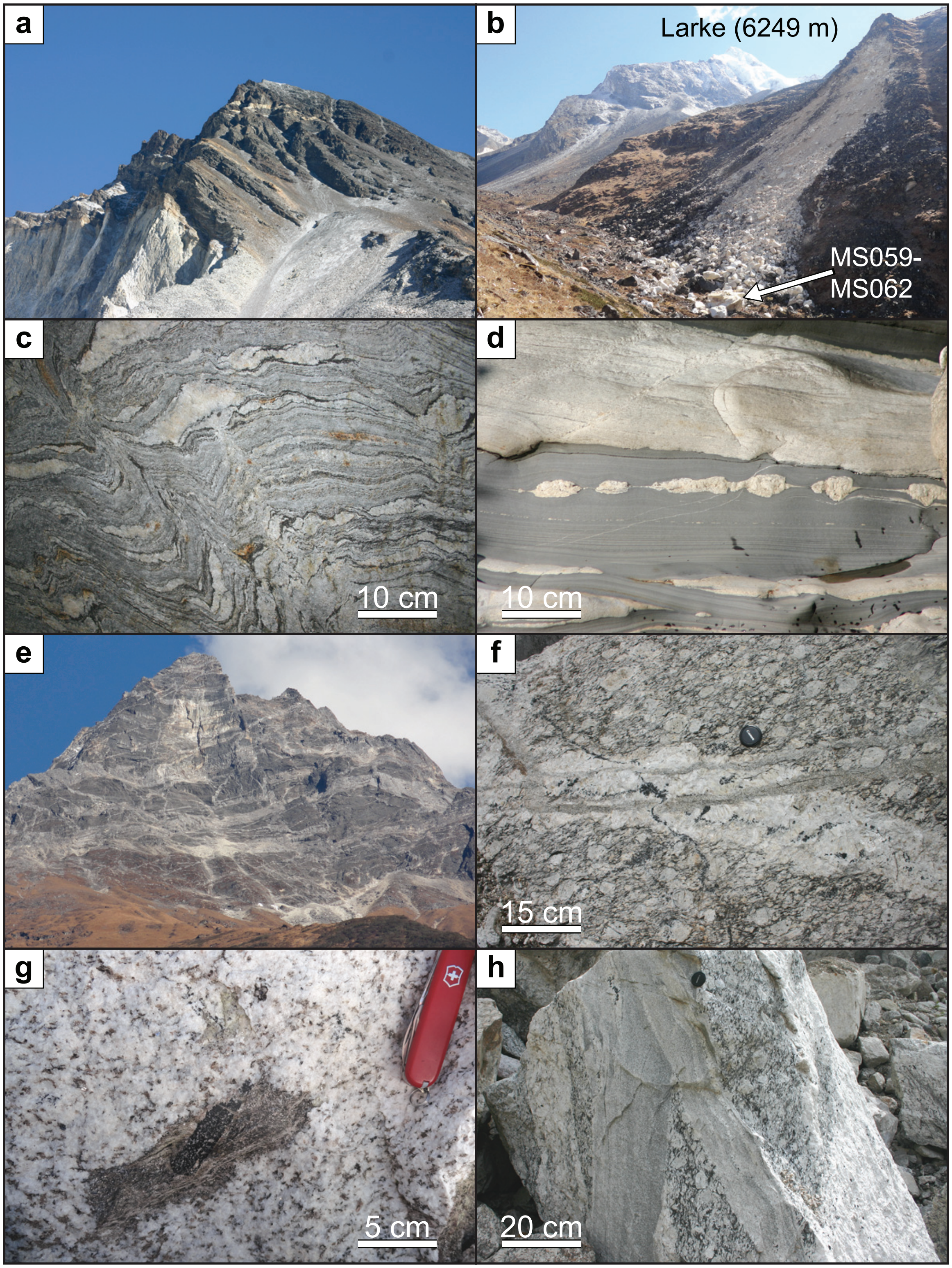

Figure 4.3 Field relationships observed in the Manaslu region. a) top contact of the Manaslu pluton with overlying TSS near Larkya La; b) freshly exposed granite boulders reveal two phases of intrusion (MS059-MS062), Larke Peak (6249 m) in background; c) unit **I** migmatites along the Budhi Gandaki; d) boudinaged leucogranite; e) injection complex SE of the pluton near ; f) unit **III** augen orthogneiss cut by tourmaline leucogranite; g) massive two-mice leucogranite with biotite selvages and euhedral tourmaline; h) orthogneiss boulder cut by several phases of leucogranite.

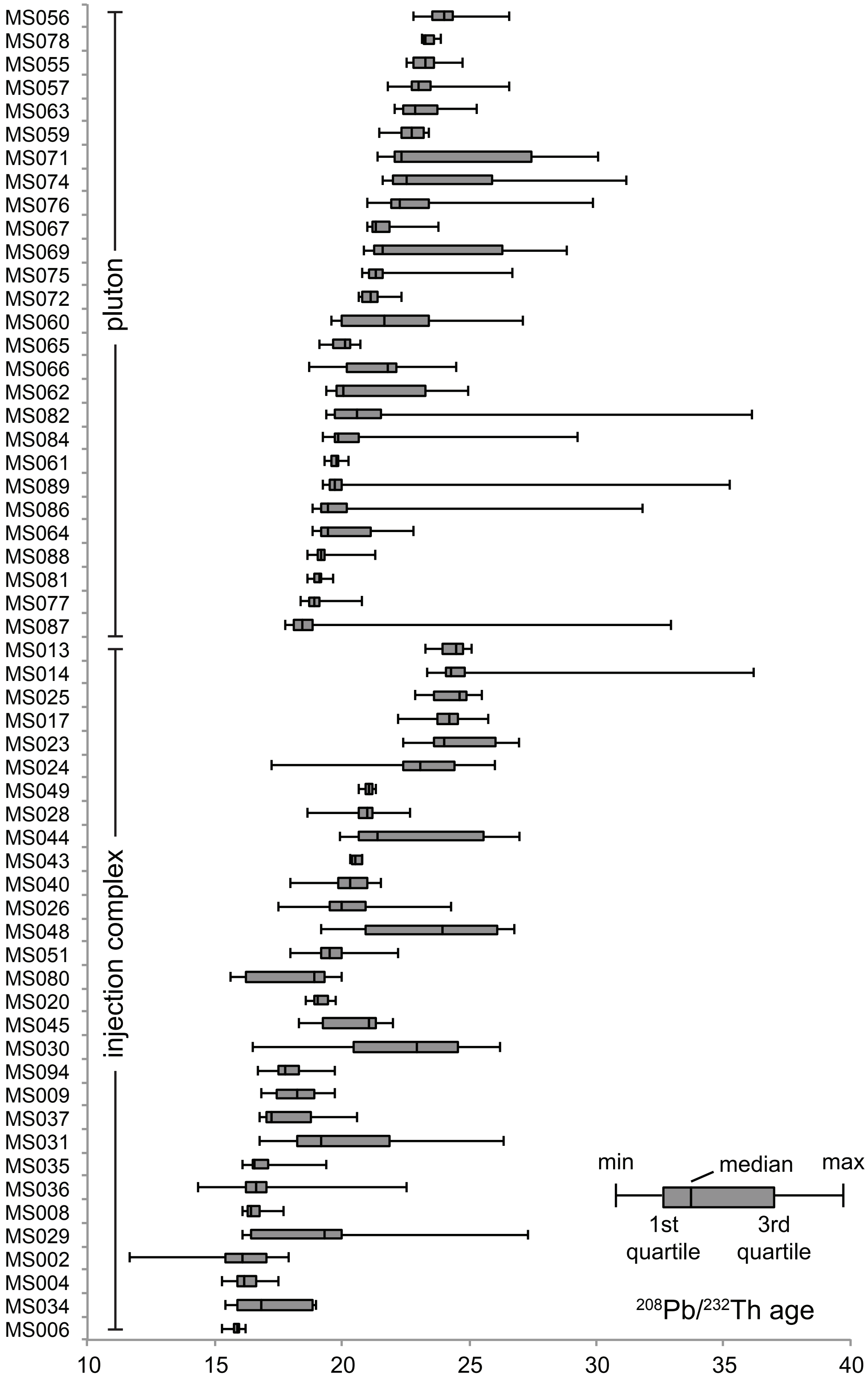

Figure 4.4 Results of U-Th/Pb analyses displayed as box and whisker plots to illustrate the range of dates contained in each sample. Paleozoic inherited grains are not plotted.

	Lat (ºN)	Long (ºE)	Elev (m)	Age (Ma)	2σ	MSWD	n /total	Min. (Ma)	Max. (Ma)	Dist	Mineralogy	Grain size	Texture	Host rock
Manaslu pluton														
MS055	28.666872	84.519807	5179	23.2	0.2	1.9	17/20	22.5	24.7	e	bt	fine	massive	granite
MS056	28.671488	84.518681	5259	23.7	0.2	2.1	34/54	22.8	26.6	e,d	tur bt	fine	massive	granite
MS057	28.671488	84.518681	5259	23.1	0.1	2.8	86/100	21.8	26.6	e	tur bt	medium	dike	granite
MS059	28.659094	84.480032	4243	22.8	0.1	2.3	55/60	21.5	23.5	e	tur bt	fine	massive	granite
MS060	28.659094	84.480032	4243	20.0	0.1	0.8	25/54	19.6	27.1	d	tur bt gt	coarse	dike	granite
MS061	28.659094	84.480032	4243	19.7	0.1	0.7	54/54	19.3	20.3	s	tur bt gt	coarse	dike	granite
MS062	28.659094	84.480032	4243	19.9	0.1	0.8	36/54	19.4	25.0	d	tur bt gt	coarse	massive	granite
MS063	28.656372	84.476560	4161	23.0	0.2	8.4	50/54	22.1	25.3	e	tur bt	fine	massive	granite
MS064	28.656372	84.476560	4161	19.3	0.1	1.2	36/54	18.8	22.8	e,d	bt	medium	dike	granite
MS065	28.636163	84.470255	5129	20.0	0.1	2.9	51/60	19.1	20.7	e	tur bt	fine	massive	granite
MS066	28.636163	84.470255	5129	20.0	0.2	1.3	13/60	18.7	24.5	e,d	tur bt	fine	dike	granite
MS067	28.686503	84.476532	4441	21.4	0.1	1.2	29/36	21.0	23.8	e,d	bt	medium	massive	granite
MS069	28.682292	84.476879	4377	21.3	0.1	0.4	22/55	20.9	28.8	e,d	tur bt	fine	massive	granite
MS071	28.679418	84.476147	4313	22.1	0.1	1.1	28/54	21.4	30.1	d	bt	fine	massive	granite
MS072	28.678519	84.475726	4266	21.1	0.1	1.1	32/36	20.7	22.4	s	bt	medium	massive	granite
MS074	28.669046	84.474612	4164	22.0	0.1	0.8	29/60	21.6	31.2	d	tur	medium	massive	granite
MS075	28.665937	84.474261	4120	21.3	0.1	1.0	26/36	20.8	26.7	s	bt	fine	massive	granite
MS076	28.663666	84.477650	4221	22.0	0.2	2.4	29/45	21.0	29.9	e,d	bt	fine	massive	granite
MS077	28.624020	84.497763	4022	18.9	0.1	1.0	55/60	18.4	20.8	s	tur bt	fine	massive	granite
MS078	28.624464	84.496741	3926	23.4	0.3	1.1	5/5	23.1	23.9	s	tur	fine	massive	granite
MS080	28.623235	84.494740	3853	19.2	0.2	1.8	12/30	15.6	20.0	e,d	tur	fine	massive	granite
MS081	28.623434	84.474862	3563	19.1	0.1	0.8	41/42	18.6	19.7	s	bt	fine	massive	granite
MS082	28.626672	84.472457	3660	19.8	0.1	1.5	25/54	19.4	36.1	e,d	tur bt	fine	massive	granite
MS084	28.628286	84.472589	3717	19.8	0.1	0.4	31/54	19.3	29.3	e,d	tur bt gt	coarse	dike	granite
MS086	28.619186	84.464689	3540	19.3	0.1	0.7	40/60	18.9	31.8	e,d	tur	medium	massive	granite
MS087	28.616151	84.465931	3425	18.3	0.1	1.2	44/60	17.7	32.9	d	bt	fine	massive	granite
MS088	28.614430	84.466391	3407	19.2	0.1	0.8	33/36	18.6	21.3	s	tur bt	fine	massive	granite
MS089	28.633373	84.472433	3764	19.7	0.1	1.1	48/60	19.2	35.3	d	tur bt	medium	massive	granite

Table 4.1 Summary of U-Th/Pb ages for the Manaslu pluton. Age distribution (dist): Paleozoic inheritance (o); discrete inheritance (d); continuous distribution (e); single age (s). Mineralogy: tourmaline (tur); biotite (bt); garnet (gt).

	Lat (ºN)	**Long** (ºE)	**Elev** (m)	**Age** (Ma)	**2σ**	**MSWD**	**n** /total	**Min.** (Ma)	**Max.** (Ma)	**Dist**	**Mineralogy**	**Grain size**	**Texture**	**Host rock**
Injection complex														
MS002	28.421160	84.896233	1612	16.4	0.3	20.0	41/54	11.7	17.9	e	tur bt	coarse	dike	bt-gneiss
MS004	28.440377	84.931477	1616	16.2	0.1	3.2	49/53	15.3	17.5	s	tur bt	medium	sill	bt-gneiss
MS006	28.452891	84.938458	2099	15.9	0.1	0.7	52/54	15.3	16.2	s	tur bt	coarse	dike	bt-gneiss
MS008	28.472990	84.982924	2445	16.5	0.1	2.7	89/96	16.1	17.7	s	bt	coarse	dike	bt-gneiss
MS009	28.472990	84.982924	2445	17.2	0.1	1.0	17/54	16.8	19.7	e	bt	fine	sill	bt-gneiss
MS011	28.497871	85.076404	3287	475	3.5	0.8	10/12	468	482	o	tur bt	fine	foliated	calc-silicate
MS013	28.497631	85.075533	3277	24.5	0.1	1.8	32/36	23.3	25.1	s	tur gt	fine	dike	calc-silicate
MS014	28.494343	85.075637	3275	24.3	0.1	1.8	52/60	23.4	36.2	d	tur	fine	massive	calc-silicate
MS017	28.492892	85.079457	3339	24.0	0.1	1.5	24/36	22.2	25.8	d	tur	fine	massive	calc-silicate
MS020	28.488737	85.082261	3484	19.1	0.1	2.0	35/40	18.6	19.8	e	tur	medium	dike	calc-silicate
MS023	28.492710	85.049876	3095	23.7	0.2	0.6	11/36	22.4	27.0	d, o	tur bt	medium	massive	granite
MS024	28.486309	85.029347	2935	23.0	0.1	0.4	23/60	17.2	26.0	d	tur	fine	foliated	granite
MS025	28.486309	85.029347	2935	24.3	0.2	7.7	54/54	22.9	25.5	e	tur	medium	dike	granite
MS026	28.482291	85.020527	2738	19.8	0.2	3.5	42/60	17.5	24.3	e,d	bt	coarse	sill	bt-gneiss
MS028	28.480633	85.016826	2699	20.9	0.1	0.6	30/116	18.7	22.7	d, o	bt	coarse	foliated	augen gneiss
MS029	28.476408	84.994160	2903	16.4	0.1	0.6	44/102	16.1	27.3	d	bt	coarse	dike	augen gneiss
MS030	28.487750	84.971915	3080	18.1	0.1	1.5	17/186	16.5	26.2	e	tur bt	coarse	sill	augen gneiss
MS031	28.487750	84.971915	3080	17.1	0.2	0.7	8/60	16.8	26.4	d, o	bt	fine	dike	augen gneiss
MS034	28.467355	84.877593	1760	16.1	0.2	7.7	21/36	15.4	19.0	e,d	tur bt	coarse	dike	bt-gneiss
MS035	28.499903	84.868157	2110	16.6	0.1	1.3	47/60	16.1	19.4	d	tur	coarse	dike	bt-gneiss
MS036	28.511051	84.857046	1984	16.6	0.1	4.5	40/45	14.3	22.5	e	tur bt gt	medium	dike	bt-gneiss
MS037	28.532525	84.831212	2120	17.1	0.1	0.6	18/50	16.8	20.6	e, o	tur bt gt	fine	dike	augen gneiss
MS040	28.550248	84.760812	2643	20.3	0.2	6.6	51/60	18.0	21.5	e	tur gt	fine	dike	bt-gneiss
MS043	28.554661	84.713243	3160	20.6	0.2	0.6	5/5	20.3	20.8	s	tur bt	medium	sill	calc-silicate
MS044	28.547039	84.627661	4058	20.8	0.2	5.4	29/60	19.9	27.0	d, o	tur	medium	foliated	bt-gneiss
MS045	28.550530	84.627159	4063	18.4	0.2	0.4	9/36	18.3	22.0	d	tur bt	coarse	dike	bt-gneiss
MS048	28.556834	84.633239	4063	19.6	0.2	1.2	5/45	19.2	26.8	d, o	bt	fine	dike	calc-silicate
MS049	28.558518	84.639752	4369	21.1	0.1	0.5	18/18	20.7	21.4	s	tur	medium	dike	calc-silicate
MS051	28.567627	84.656614	3863	19.5	0.1	1.5	34/45	18.0	22.2	d	tur	medium	dike	calc-silicate
MS094	28.597678	84.437986	2887	17.8	0.1	2.8	22/30	16.7	19.7	e	tur bt	fine	dike	bt-gneiss

Table 4.1 (continued) Summary of U-Th/Pb ages for the injection complex. Age distribution (dist): Paleozoic inheritance (o); discrete inheritance (d); continuous distribution (e); single age (s). Mineralogy: tourmaline (tur); biotite (bt); garnet (gt).

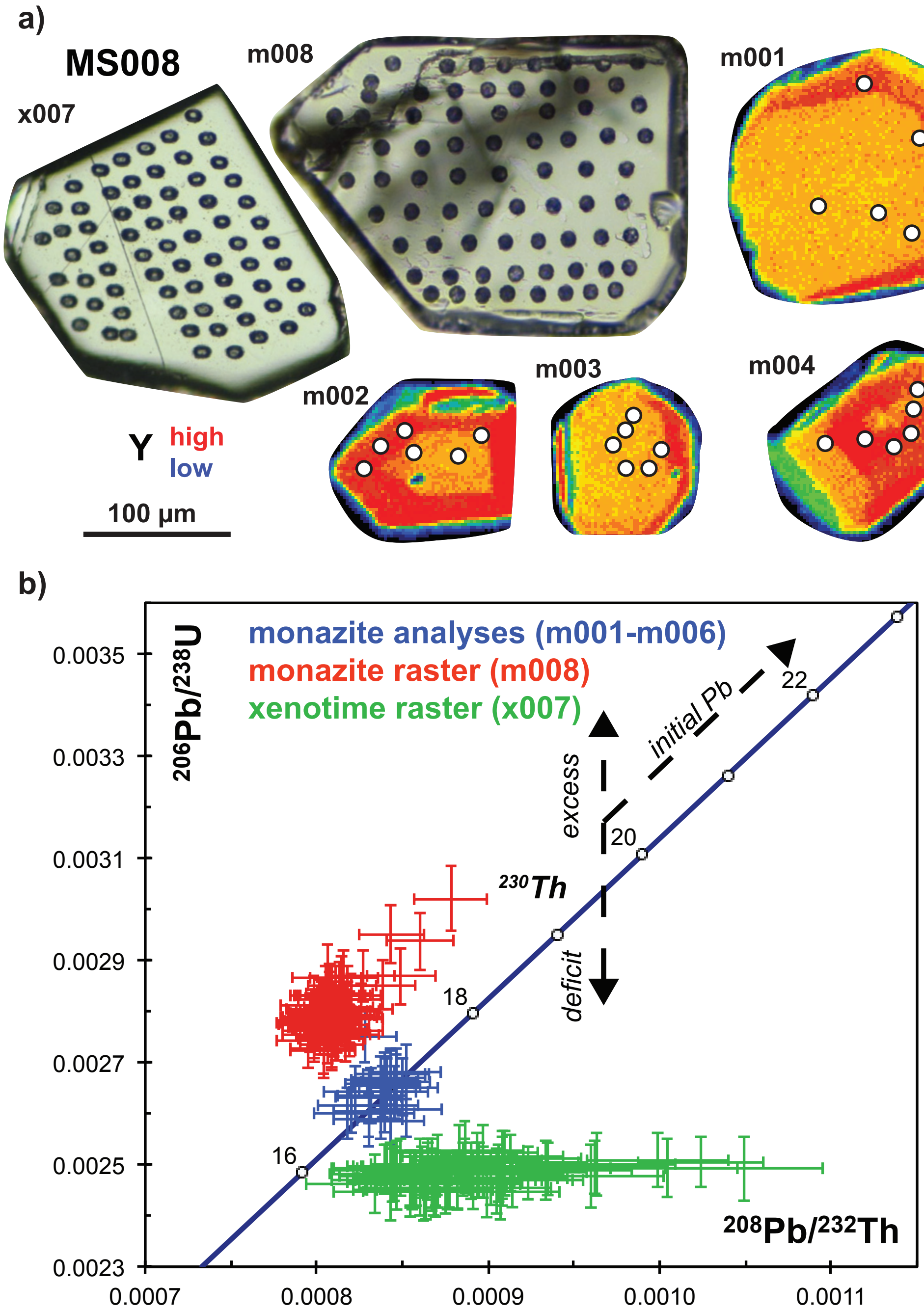

Figure 4.5 a) Images of one xenotime and five monazite grains selected for U-Th/Pb comparison analysis via LASS raster mapping (x007, m008) and targeted sampling of Y domains revealed by X-ray maps (m001-m004). b) U-Th/Pb results indicate ^{206}Pb excess in monazite and deficit in xenotime, with minor common Pb contamination. ^{208}Pb/^{232}Th dates are unaffected by initial ^{230}Th, and yield overlapping results.

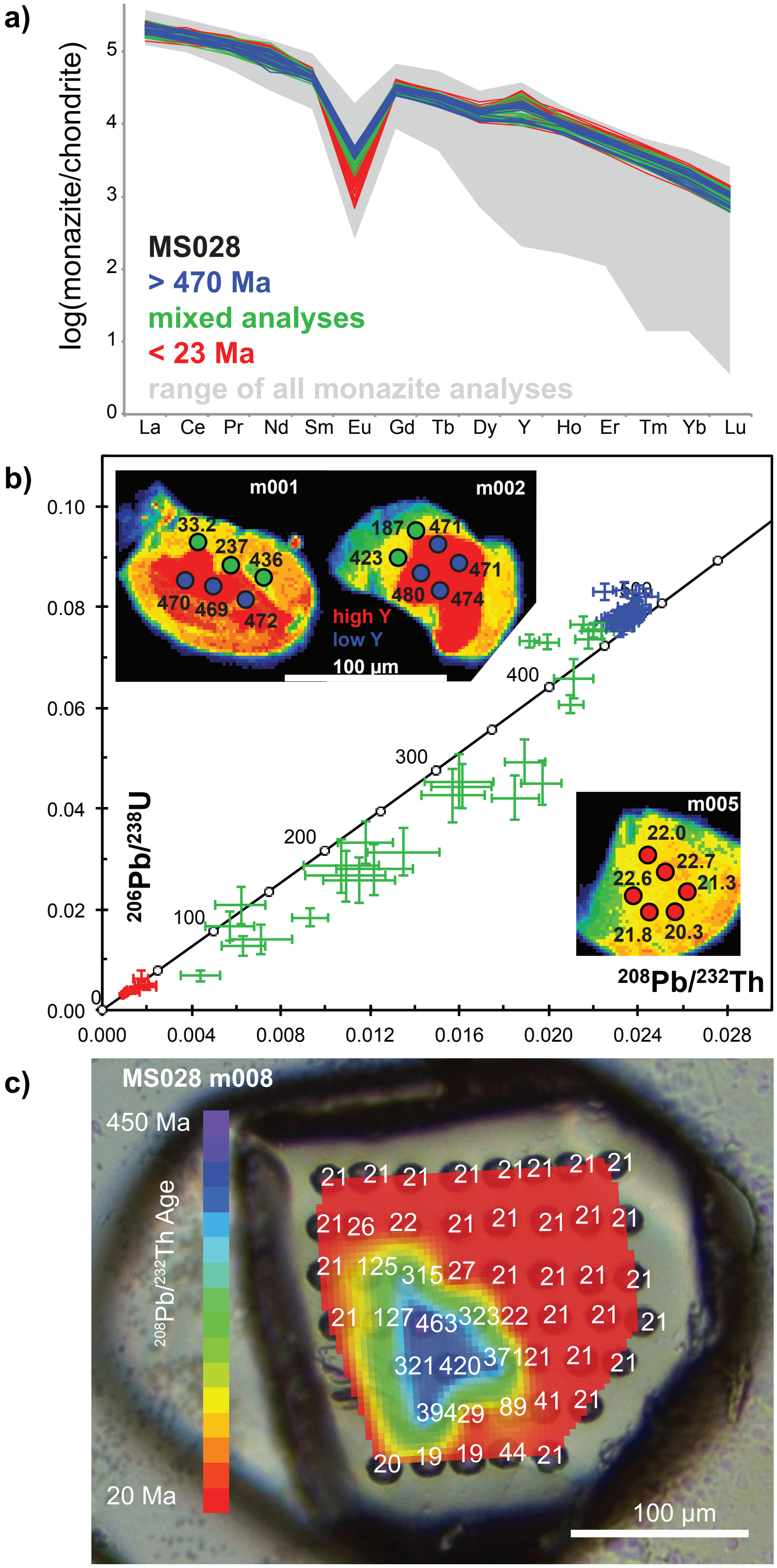

Figure 4.6 Sample MS028 displays evidence for Paleozoic inheritance in a) trace element data b) Th-Pb concordia with inset X-ray maps of Y and c) Raster map of ^{208}Pb/^{232}Th ages.

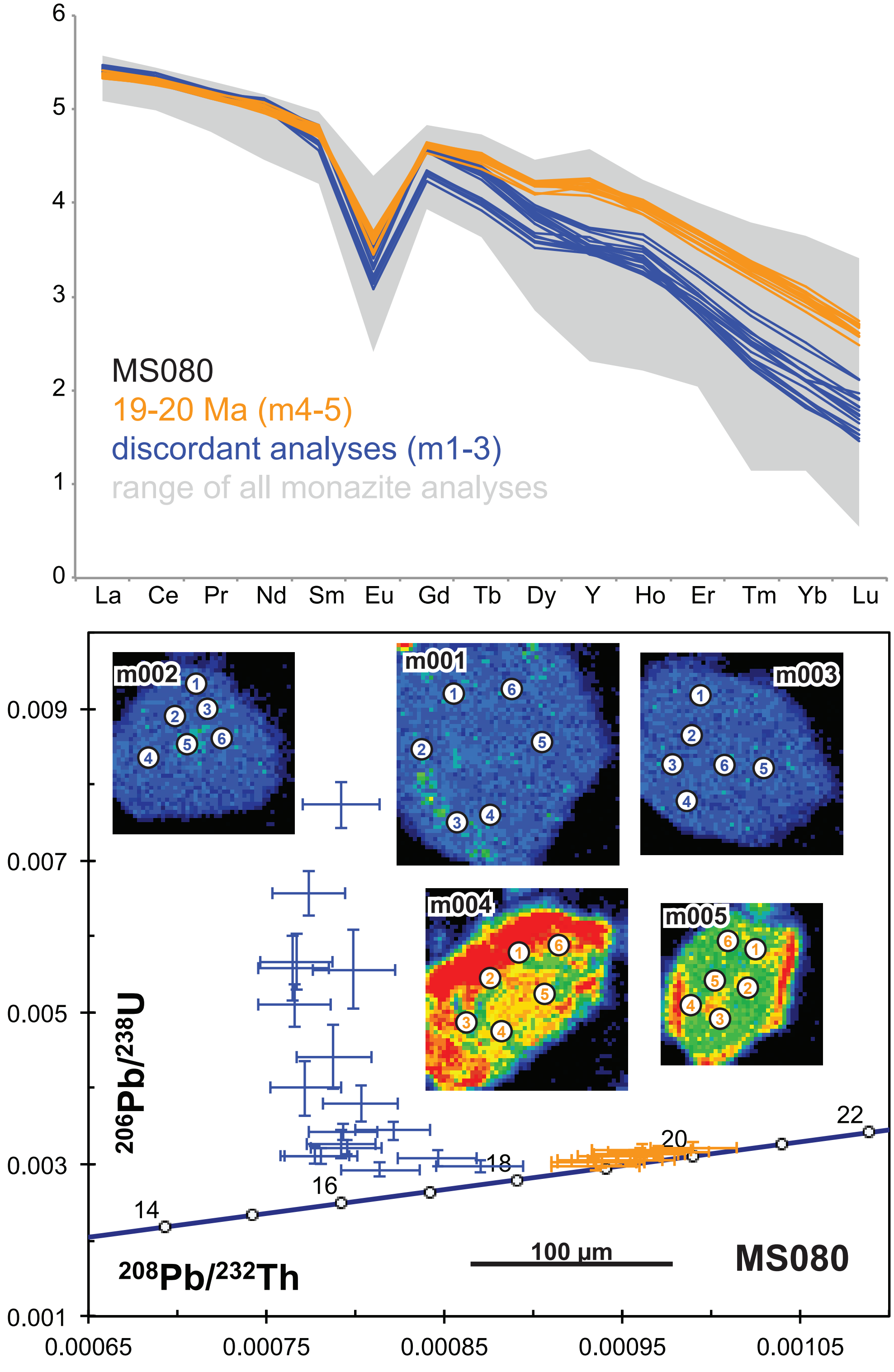

Figure 4.7 Sample MS080 displays evidence of dissolution/reprecipitation reflected by a) trace element data with depleted HREE and Eu and b) mobilization of U visible in X-ray maps of U and reset U-Th-Pb systematics on concordia diagram with $^{208}Pb/^{232}Th$.

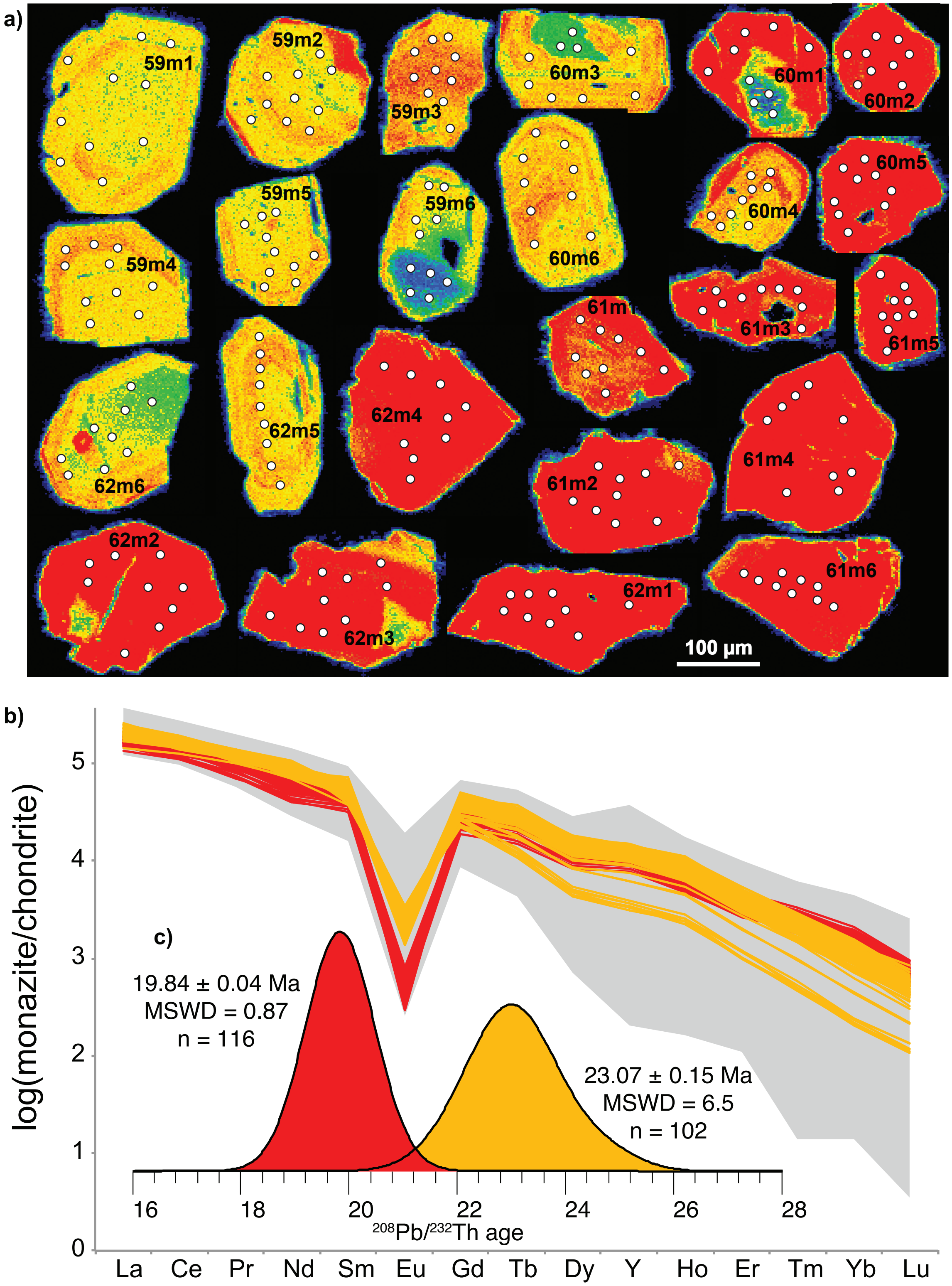

Figure 4.8 a) Identically scaled X-ray maps of Th zoning indicate two chemically distinct populations of monazite. The main granite (MS059) contains lower Th grains, whereas cross-cutting pegmatitic dikes contain exclusively higher Th grains (MS061) or both populations (MS060 and MS062). Circles mark locations of 10 µm diameter ablation spots. b) Trace element profiles indicate a more pronounced negative Eu anomaly among the higher Th grains. c) Kernel Density Estimate (KDE) plots of the two chemical populations yield distinct age peaks.

analyses are concordant to reversely discordant (Fig. 4.5b) and xenotime analyses plot slightly below concordia.

4.4.2 Paleozoic inheritance

The analyses with Paleozoic dates and/or evidence for mixing between Paleozoic and Tertiary components constitute a subordinate portion of the dataset (<3 %) and occur in seven samples located in the injection complex (Table 4.1). One foliated granite intruding calc-silicate gneiss from the Tsum Valley (MS011) yields a Paleozoic age of 474.5 ± 3.5 (MSWD = 0.8) with no evidence for Tertiary monazite growth. A sample of augen orthogneiss (MS028) intruded by leucogranite contains monazite with distinct chemical domains (Fig 4.6a). Cores have low U (1,000-2000 ppm), high Th/U (>30), moderate to high Y (20,000- 40,000 ppm), and Eu/Eu* of < 0.05; rims have high U (4,000-8,000), moderate Th/U (10-15), low to moderate Y (15,000-30,000 ppm), and Eu/Eu* of > 0.1. Plotted on concordia (Fig. 4.6b), the array of data indicates two-component mixing between Paleozoic dates of 470-480 Ma, and Tertiary crystallization ages yielding a weighted mean date of 20.9 ± 0.1 (MSDW = 0.6, n = 30 of 116). Raster analyses (n = 48) of a euhedral grain (m008) reveals the presence of an inherited Paleozoic core and a ~21 Ma rim (Fig. 4.6c). The other five granites show similar evidence for Paleozoic inheritance of whole grains and cores, but notably occur among massive to foliated granites as well as dikes emplaced into augen gneisses and calc-silicate gneisses in the injection complex (Table 4.1). Although unequivocal evidence of Paleozoic inheritance is not observed in the main body of the Manaslu pluton, this does not preclude the possibility of small component of unrecognized mixed analyses resulting in dispersion of Tertiary dates.

Excluding Paleozoic inheritance, the remaining 2759 analyses comprise >90% of the dataset and yield Tertiary dates ranging from 36.2 ± 1.0 to 11.7 ± 0.4 Ma (Fig. 4.5). This broad range results from the combined effects of dissolution/precipitation and Tertiary inheritance.

4.4.3 Dissolution/reprecipitation

One sample from the Manaslu pluton (MS080) displays evidence for dissolution/precipitation and U mobility (Fig. 4.7). X-ray maps reveal two populations of grains; two grains have moderate U cores with high U rims (4,000-18,000 ppm) and three grains have very low U (300-3,500 ppm). Trace element profiles indicate HREE depletion of low-U grains with low Y (5,000-10,000 ppm) and high La/Lu (2,000-6,000) relative to high-U rims with high Y (15,000-30,000) and low La/Lu (500-750). High-U grains yield a weighted mean age of 19.2 ± 0.2 (MSWD = 1.8), whereas low-U grains display dispersion in both ^{208}Pb/^{232}Th and ^{206}Pb/^{238}U. The extreme reverse discordance of low-U analyses is best explained by loss of U rather than excess ^{230}Th. Th/U varies 5-10 in the high-U grains to > 100 in the low-U grains, which is considerably higher than typical values 1-25 for igneous monazite in this study. Other samples display minimal evidence for U-Th/Pb disturbance by dissolution/reprecipitation, however, anomalous younger ages may represent the effect of similar Pb-loss processes. Excluding anomalous younger ages results in minimum age of 15.2 ± 0.3 Ma.

4.4.4 Tertiary inheritance

After accounting for Paleozoic inheritance and possible disturbances of the U-Th/Pb system by dissolution/reprecipitation, many samples display ranges of ages with large MSWD values precluding the calculation of weighted mean ages representative of single populations (Fig. 4.3; Table 4.1). Age distributions indicate discrete subpopulations as well continuous distributions with no discernable gaps. Furthermore, monazite X-ray maps indicate intra-grain age variability between chemical domains as well as inter-grain variability within a sample.

In order to characterize the spatial scale of temporal variability within the pluton, four samples were collected from multiple intrusive phases exposed in a 10-m-diameter granite boulder located at the foot of a talus slope west of Larkya La (Fig. 4.2b; Fig. 4.8). MS059 represents the main phase of medium-grained, muscovite-biotite leucogranite with a magmatic foliation defined by biotite-tourmaline schlieren. The leucogranite is cut by three phases of pegmatitic dikes, ranging from 5 to 10 cm in width and oriented sub-parallel to each other, including muscovite-biotite-tourmaline bearing (MS060) and muscovite-biotite-tourmaline-garnet bearing (MS061, MS062) leucogranites. X-ray maps of monazites from these rocks indicate two chemically distinct populations; high-Th grains only occur within the pegmatite dikes, whereas low-Th grains occur within the pegmatites and the host granite (Fig. 4.8a). Trace element analysis demonstrates that the high-Th (> 80,000 ppm) grains are characterized by more pronounced negative Eu anomalies than low-Th (< 80,000 ppm) grains (Fig. 4.8b). Analyses (n = 116) of the high-Th grains yield a ^{208}Pb/^{232}Th weighted mean date of 19.84 ± 0.04 Ma (MSWD = 0.87) indicating a single population, however, analyses (n = 102) of low-Th grains yield dates ranging from 25 to 21.5 Ma, with a weighted mean date of 23.07 ± 0.15 Ma (MSWD = 6.5) suggesting these monazites do not define a single population (Fig. 4.8c).

The preservation of monazites in the younger phases with chemical and isotopic similarities to the older phase indicates inheritance of Tertiary components. Discrete inheritance was identified in many samples from the Manaslu pluton and injection complex. Excluding inherited analyses yields emplacement ages ranging from 25.5 ± 0.6 to 15.2 ± 0.4 Ma. Within individual samples, continuous age distributions result in large MSWD values for some samples (Table 4.1), however emplacement ages and inheritance patterns indicate spatial trends in the crystallization of the Manaslu pluton and injection complex (Fig. 4.9).

4.4.5 Manaslu pluton

Granites from the Manaslu pluton yield weighted mean dates ranging from 23.7 to 18.3 Ma, with evidence for continuous and discrete inheritance from 36.1 to 18.8 Ma (Fig. 4.9). Samples from higher structural positions generally yield older ages than ages at lower structural positions. Granites collected from Larkya La (~5200 m) represent the structurally highest position of the exposed pluton and yield some of the oldest emplacement ages with broad, continuous age distributions. Fine-grained MS055 and nearby (~0.5 km) medium grained MS057 yield equivalent dates of 23.2 ± 0.2 (MSWD 1.9) and 23.1 ± 0.1 (MSWD = 2.8), and are interpreted to represent the same phase of crystallization that intruded MS056, a coarse-grained, tourmaline-bearing body with ^{208}Pb/^{232}Th date of 23.7 ± 0.2 (MSWD = 2.1).

Granites at lower structural positions, near the village of Bimtang yield dates of 18.9 to 19.9 Ma (Fig. 4.2). Although distinct generations of granite are recognized by differences in mineralogy and grain size, no robust correlation between age and texture or chemistry is observed.

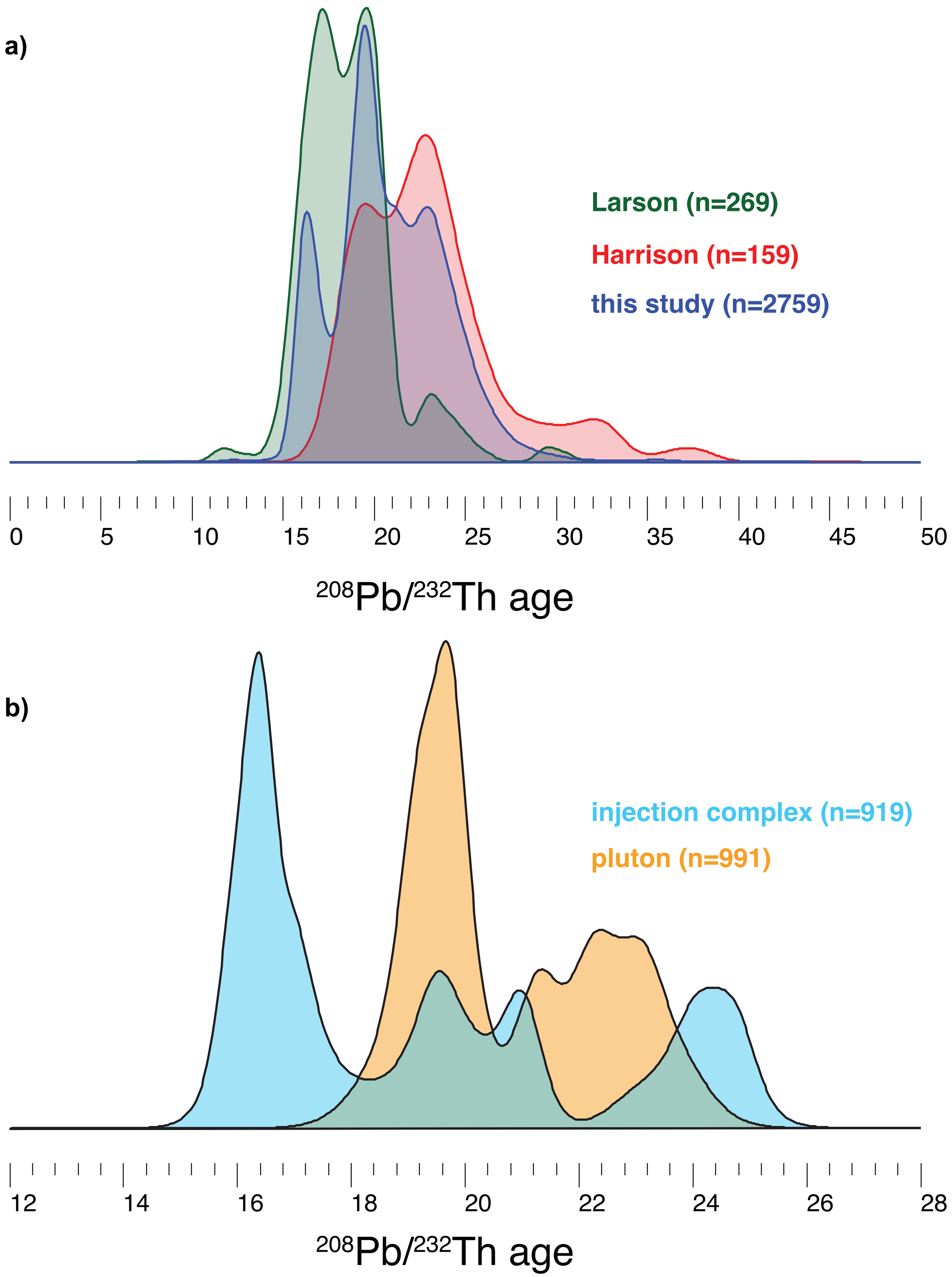

Figure 4.9 Kernel Density Estimate (KDE) plots of monazite ages. a) Data from Harrison et al. (1999), Larson et al. (2011), and analyses from this study. b) Emplacement ages for the Manaslu pluton and the injection complex.

4.4.6 Injection complex

Granites from the injection complex yield weighted mean dates ranging from 25.5 to 15.2 Ma with evidence for continuous and discrete inheritance from 36.2 to 17.0 Ma (Fig. 4.9). The duration of granite crystallization observed in the injection complex is longer than that observed in the pluton, however, emplacement ages define distinct peaks. Massive and foliated granites exposed in the Tsum Valley, near the village of Chhokang yield older dates of 24.5 ± 0.1 (MSWD = 1.8) to 23.0 ± 0.4 (MSWD = 0.4). Cross-cutting granites occur throughout the injection complex and yield younger dates ranging from 21.1 ± 0.1 (MSWD = 0.5) to 15.9 ± 0.1 (MSWD = 0.7), with the youngest dikes (15-17 Ma) occurring within migmatitic gneisses near the confluence of the Budhi Gandaki and Shyar Khola.

4.5 Discussion

4.5.1 Interpretation of monazite dates

Monazite is extremely retentive of Pb, due in part to its ability to anneal radiation damage at T < 175ºC (Meldrum 1998), and limited diffusivity of Pb at T < 1000ºC (Cherniak et al. 2004). The widespread occurrence of inherited monazite in Himalayan leucogranites with undisturbed U-Th/Pb systematics (e.g. Copeland et al. 1988; Parrish et al. 1990; Harrison et al. 1995; Harrison et al. 1999) indicates volume diffusion of Pb in monazite can safely be ignored at T <800ºC required for melting of the GHS (Montel, 1993; Patiño Douce and Harris, 1998). Furthermore, the occurrence of inherited monazite implies 1) limited solubility of monazite due saturation of P or LREE in leucogranite melts, and/or 2) insufficient time for dissolution of monazite into an under-saturated melt. The time required for monazite dissolution depends on several factors including grain size, temperature, the degree of saturation of the melt, the rate of diffusion of REE and P in the melt away from dissolution site, and the degree of crystallinity of the melt. Studies of the partitioning behavior of REE during anatexis have demonstrated that the residence time of leucogranite melt in the source rock is sufficient for monazite to reach equilibrium with the melt (Ayres et al. 1997), albeit with notable exceptions in which melt extraction occurred faster than 50 k.y.

Broad ranges of ^{208}Pb/^{232}Th dates observed within individual monazite grains and between monazite grains within can be the result of four processes: 1) common Pb contamination; 2) dissolution/reprecipitation reactions and open U-Th/Pb system behavior; 3) inheritance of restitic monazite; and 4) protracted crystallization. Examples of each type of behavior is discussed here.

Analysis of monazite and xenotime from MS008 (Fig. 4.5) demonstrate the effects of excess ^{230}Th and unsupported ^{206}Pb manifested as reversely discordant behavior in monazite and ^{230}Th deficit in xenotime (Schärer, 1984; Parrish 1990). These results are consistent with U/Th partitioning between the two phases (Schärer, 1984). The pristine sector zoning visible in Y maps, euhedral morphology, and evidence for U/Th partitioning are consistent with primary igneous monazite and xenotime crystallization from a melt. A few xenotime analyses show dispersion to slightly higher ^{208}Pb/^{232}Th ratios, likely due to the lower abundance of radiogenic ^{208}Pb relative to common Pb in xenotime. Similarly, a few analyses located along fractures on the raster map m008 resulted in dispersion along concordia to higher ^{208}Pb/^{232}Th and ^{206}Pb/^{238}U values. The effect of common Pb is significantly more noticeable in the ^{207}Pb/^{206}Pb ratio, and therefore analyses with common Pb were rejected (see section 4.3.5). Monazites targeted for analysis by domain are free of common Pb, illustrating the value of this technique over raster mapping. A vertical line through all the remaining data indicates crystallization of both phases at ~ 16.5 Ma, confirming the validity of ^{208}Pb/^{232}Th monazite dates. Interpretation of this example indicates that common Pb effects are minimal, and closed U-Th/Pb systematics typical for igneous monazite.

Recrystallization of monazite via metamorphic reactions or dissolution/precipitation reactions can efficiently mobilize Pb and reset monazite ages (e.g. Seydoux-Guillame et al. 2002). Didier et al. (2013) demonstrate U-Th/Pb systematics are unaffected by late-stage hydrothermal-magmatic fluids, but subsequent interaction with F-rich fluids can dissolve monazite, mobilize Th, and precipitate monazite with common Pb. Textural evidence for dissolution/precipitation can be used to discriminate between fluid-mediated processes or primary igneous crystallization. For example, analyses of MS080 (Fig. 4.7) demonstrate the mobilization of U from monazite after crystallization. Unaltered grains contain retain HREE and U and older ^{208}Pb/^{232}Th dates, whereas the altered grains display a range of U, Th, HREE, and Pb mobility, resulting in extreme scatter in U/Th, beyond that observed in igneous monazite. While the date of dissolution/reprecipitation reaction is poorly constrained, it likely occurred after 16 Ma and may correspond to late-stage magmatic or hydrothermal fluids. Clear evidence of similar open U-Th/Pb behavior is rare among granites observed in the study, and constitutes < 3% of the entire dataset. We therefore conclude that the dispersion observed in ^{208}Pb/^{232}Th dates are not due to 1) common Pb or 2) the effect of fluid-mediated dissolution/reprecipitation, and are more likely the result of either 3) inheritance of restitic monazite and/or 4) protracted crystallization.

4.5.2 Inherited monazite

Dissolution of monazite occurs in the metapelitic source rocks during melting (Ayres et al. 1997), yet inherited monazite is well documented among Himalayan leucogranites and suggests some restitic monazite survives and is incorporated into the leucogranite magma (Copeland et al. 1998; Harrison et al. 1995; Harrison et al. 1999). Modeling of monazite behavior during anatexis (Yakymchuck et al. 2013) predicts subsolidus monazite in the residuum will be completely consumed during prograde metamorphism and subsequent decompression. The apparent conundrum between inherited monazite and dissolution of monazite during melting can be explained by saturation of the melt with respect to REE and P (Montel, 1993). Alternatively, incorporation of inherited monazite may occur during melt transport and/or emplacement rather than during melt generation in the source rock. In this model, the leucogranite magma need not be monazite-saturated in order to preserve inherited ages so long as the timescale of monazite dissolution is greater than melt transport and emplacement processes. Restitic monazite in the source rock, host rock, and/or transport network are likely sources for Paleozoic inheritance in Tertiary leucogranites.

For example, a granite emplaced into augen orthogneiss (MS028) displays evidence for anhedral inherited monazite cores surrounded by euhedral rims indicative of igneous crystallization (Fig. 4.6). The sharp boundary between inherited cores and magmatic overgrowth indicates dissolution of the inherited monazite by the melt and precipitation of igneous rims. The inherited grains may be derived from the host gneiss, or the augen gneiss may have melted. Fluid-present melting of orthogneiss has been observed in the North Himalayan domes as well as in the Karakorum and Zanskar region of the northwest Himalaya (Reichardt et al. 2010; Horton et al. 2014), whereas fluid-absent melting of granitic protoliths requires a large proportion of muscovite. The upper intercept ages of 470-480 Ma are consistent with protolith ages for the augen orthogneiss and Cambro-Ordovician granites exposed in the Mahabharat (Le Fort, 1975; Schärer and Allègre, 1983), and we interpret the host rock to represent the source of inheritance.

A foliated granite exposed in the Tsum Valley (MS011) yields an age of 474.5 ± 3.5, interpreted as the crystallization age for the augen gneiss protolith. Other inherited Paleozoic ages occur within the dikes of the injection complex and indicate that restitic monazite may be incorporated during melt transport. The dikes are emplaced into orthogneiss, paragneiss and calc-silicate gneiss, thus monazite may be derived from the source or the host rocks. Metamorphic monazite associated with the Paleozoic orogenic event (Catlos, Harrison, et al. 2002; Gehrels et al. 2003; Martin et al. 2007) and of Carboniferous age (Imayama and Suzuki, 2013) also represent a possible sources for inherited Paleozoic monazite.

Granites from the injection complex and the Manaslu pluton also show evidence for Tertiary inheritance. Some age distributions exhibit discrete populations of inherited monazite, whereas others show a continuous range of dates. For example, a massive granite sample (MS059) intruded by a series of pegmatite dikes (MS060-MS062) contains low-Th grains with oscillatory zoning and yields a weighted mean age of 22.8 ± 0.1 (MSWD = 2.3; n = 55 of 60). The high MSWD indicates a continuous age distribution from 23.5 to 21.5 Ma, and is interpreted to reflect protracted igneous crystallization. The pegmatite dikes contain two populations of monazite, including low-Th grains similar in appearance to the massive granite as well as high-Th grains. The low-Th grains show no evidence of dissolution, and yield ages consistent with the massive granite, suggesting that incorporation of restitic grains occurs during transport or emplacement of the pegmatites. The high-Th grains in the pegmatites yield similar weighted mean ages of 19.7 ± 0.1 Ma (MSWD = 0.7), 19.9 ± 0.1 Ma (MSWD = 0.8), and 20 .0 ± 0.1 Ma (MSWD = 0.7), suggesting dikes with similar compositions were emplaced simultaneously. The low-Th grains yield similar ages to host granite with slightly more dispersion, and is interpreted to represent incorporation of Tertiary igneous monazite during melt transport and/or emplacement. The discrete inheritance of the dikes contrast with the continuous inheritance observed in the granite, and indicate protracted crystallization of the main granite phase. Separating discrete Tertiary inheritance from protracted crystallization allows for the examination of "emplacement" ages that represent the time of igneous monazite growth (Fig. 4.9).

Early igneous monazite ages imply monazite began crystallizing by that time and melting had commenced, whereas later-formed monazite from the same rock records final crystallization of the granite following emplacement. The range of protracted crystallization ages thus indicates the timescales required between melt generation, segregation, amalgamation, mobilization, and emplacement to occur (Fig. 4.10). The pattern of igneous crystallization is further complicated by incorporation of metamorphic monazite from the source rock during segregation, mixing of melt batches and their inherited components during amalgamation, entrainment of monazite derived from the melt conduit wall rocks during mobilization or host rocks during emplacement. Thus, leucogranites potentially record a complex signal of monazite derived from a variety of sources, and can be used to infer characteristics of their source and emplacement history.

4.5.3 Generation and emplacement of the Manaslu granite

The occurrence of monazite with different age components within a single grain, and multiple grains of different age occurring within a single rock are consistent with

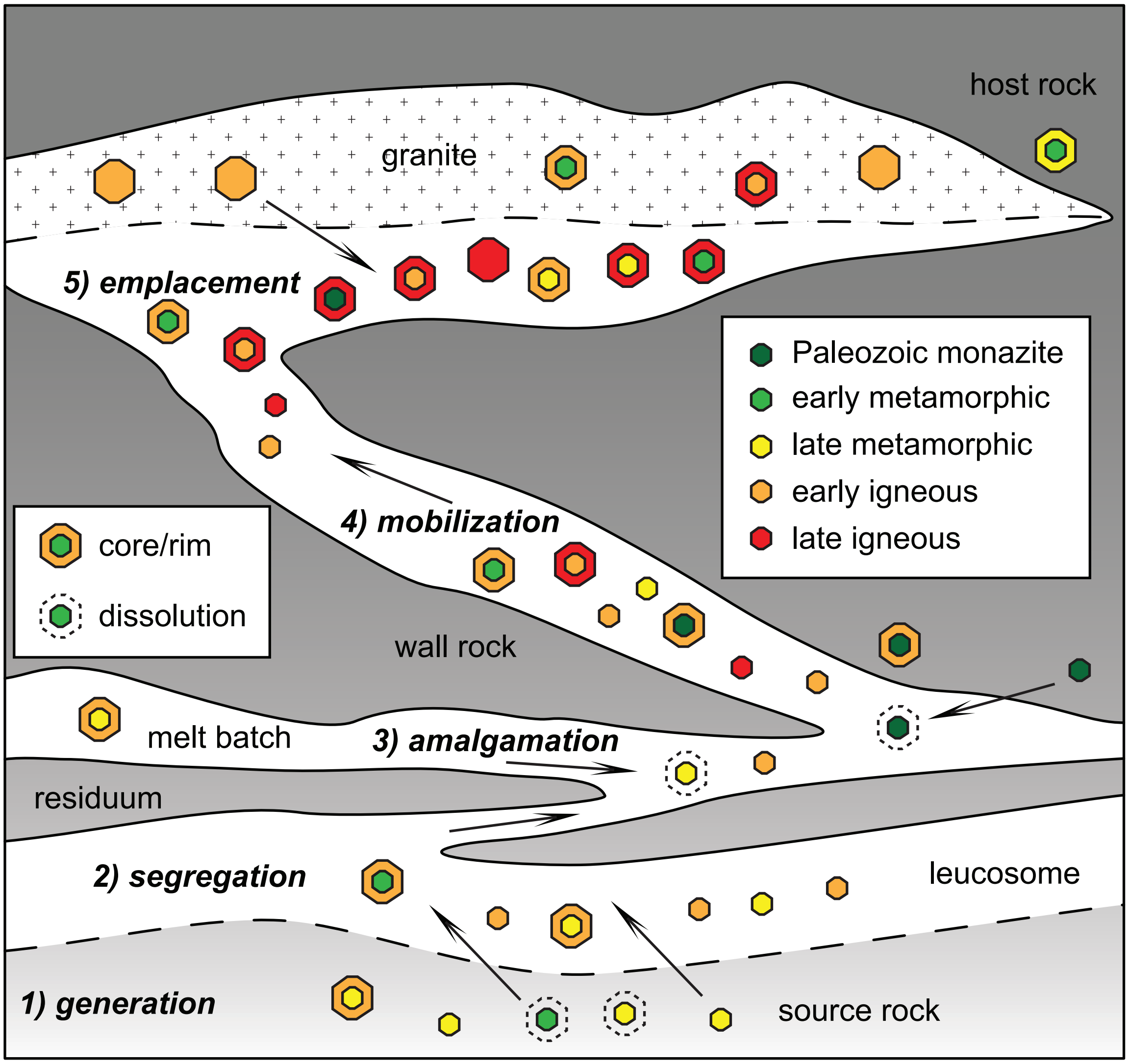

Figure 4.10 Schematic illustration of possible sources for inherited monazite in Himalayan leucogranites during five melting processes.

previous isotopic studies that document heterogeneity on a small scale (Vidal et al. 1982; Deniel et al. 1987). Isotopic variability has been interpreted as evidence that the Manaslu granite formed without significant mixing different batches of melt (France-Lanord et al. 1988). This study suggests that a significant portion of monazite crystallized prior to emplacement, consistent with injection of high-viscosity crystal-rich magmas in small batches.

Granite crystallization ages of the Manaslu pluton indicate emplacement occurred between 18.5 and 25 Ma. Although there is no distinct gap in ages, two peaks are observed at ~19.5 and ~22.5 Ma, consistent the Bimtang and Larkya La phases of Harrison et al. (1999). Whether these peaks define pulses of increased magmatism or a sampling bias of a continuous emplacement history is unclear. The older peak (Larkya La phase) however, is significantly broader than previously documented, and a subordinate peak at ~21.4 Ma is recognized.

Emplacement ages from the injection complex yield a continuous range that partially overlaps with the ages of the Manaslu pluton, but extends to younger and older dates. An older phase of intrusion is recognized in the Chhokang arm, indicating emplacement at 24 ± 1 Ma not recorded in the pluton. The ~19.5 Ma phase occurs in the as well as a ~21 Ma phase unrecognized in the pluton. Lastly, a distinct phase of magmatism at ~16.5 Ma occurs and reflects dikes within the GHS migmatites at the confluence of the Budhi Gandaki and the Shyar Khola below the Chame detachment (Fig. 4.1). These ages are consistent with observations of GHS migmatites that record melting from 18-16 Ma (Larson et al. 2011). Given their similarity in age, we infer a genetic relationship and interpret the GHS migmatites as the source for the late late-stage dikes. The initiation of anatexis suggests decompression of this section of the GHS did not occur until ~19 Ma, and is perhaps related to simultaneous movement on the MCT and STD.

Two hypotheses explain the limited overlap between $^{208}Pb/^{232}Th$ monazite ages from metapelitic gneisses of the GHS (Larson et al. 2011) and the main phase of Manaslu leucogranite crystallization: 1) the GHS migmatites are the source of the Manaslu granite, but retain no record of the 25-18 Ma melting history; or 2) the GHS migmatites exposed along in the Budhi Gandaki are not the source, and melting elsewhere in the GHS coalesced to form the Manaslu pluton.

The survival of restitic monazite in the melt, as evidenced by the component of inherited monazite ages in the granite implies that super-saturation of the melt with respect to monazite-forming components (LREE and P) persisted throughout the melting history of the GHS. It therefore seems unlikely that the GHS migmatites exposed along in the Budhi Gandaki represent the source, as that they retain no record of monazite crystallization during the time interval in which the Manaslu pluton was assembled. Instead, the Manaslu pluton may have been fed by dikes and sills sourced deeper in the GHS that has not yet been exposed in the Manaslu region. Exposures of the GHS in the Everest region are perhaps equivalent to the source rocks of the Manaslu pluton (Annen et al. 2006).

4.5.4 Constraints on melting and deformation

There are compelling reasons to interpret granite crystallization ages as providing constraints on deformation, however, doing so requires well-documented field relationships and geochronologically well-characterized ages. Previous workers suggest that the pluton cuts the STD (Guillot et al. 1995; Harrison et al. 1999) or is cut by the

STD (Searle and Godin, 2003). These seemingly contradictory relationships may be explained by multiphase intrusion of the Manaslu pluton over a protracted period. The large volume of granite that comprises the Manaslu pluton formed between 25-18 Ma, indicating that melting of its source rocks had initiated by 25 Ma and likely continued to 18 Ma. Granites from the injection complex suggest melting occurred from 26 to 15 Ma. Late-stage granitic dikes intruded the migmatites at the base of the Manaslu pluton below the Chame detachment from 15-17 Ma, consistent with in situ melting of their host rocks at this time. The late-stage dikes may represent 1) the last increment of melting of the same source as the Manaslu pluton, perhaps associated with deformation along the MCT (Harrison et al. 1999) or 2) the earlier granites may have derived from deeper GHS sources. The first hypothesis implies that any evidence of earlier melting in the migmatites of the upper GHS near the base of the pluton was destroyed. The similarity in age between a migmatite exposed structurally deeper (MS-62 of Larson et al. 2011) and the main phase of Manaslu granite crystallization supports the second hypothesis. Considering the propensity of at least some fraction monazite to remain in the residuum during partial melting, as well as the evidence of inherited monazite throughout the Manaslu pluton and injection complex, suggests multiple sources is a more feasible explanation.

4.6 Conclusions

1. The Manaslu pluton is heterogeneous with respect to monazite ^{208}Pb/^{232}Th ages with evidence for semi-continuous melt generation from 26 to 18 Ma.

2. The injection complex encompasses the range of dates recorded in the pluton, as well as an older ~26 Ma phase and a younger ~15-17 Ma phase of granite emplacement.

3. The 15-17 Ma pulse records the intrusion of post-kinematic dikes unrelated to the main phase of leucogranite crystallization, but are similar in age to monazite ages recorded in GHS migmatites.

4. The augen orthogneiss protolith represents the likely source of Paleozoic inherited monazite cores, which were entrained in younger leucogranites during intrusion.

5. Granites of the Tsum Valley, previously mapped as the Chhokang arm, consist of many distinct, discontinuous bodies of leucogranite with a variety of intrusive relationships that span a wide range of ages. Some ages from massive granite bodies are overlap with those of the Manaslu pluton, and may be related. Many bodies, especially cross-cutting dikes, postdate the main phase of Manaslu pluton, suggesting these granites may not share a genetic relationship as either feeder dikes or an eastern extension of the pluton.

5. Conclusions

As the previous chapters illustrate, the combined result of the three projects is a thorough understanding of the timescales of partial melting in the Greater Himalayan Sequence. In sum, over 6000 spot analyses of 300 monazite grains from over 100 rocks contribute to a very large dataset to help elucidate the timescales of granite crystallization throughout the Himalayan orogen. From this dataset, several conclusions can be drawn and are summarized here.

First, from a methodological point of view, documentation of the field relations is an important step for any geological study of Himalayan granites. The broad range of dates obtained in this study clearly illustrate that not all granites that occur in the GHS are equivalent. Field relations are essential for interpreting complicated crystallization histories, and reveal informative correlations between temporal and spatial variation. Furthermore, dating leucogranites with well-documented field relationships can provide important timing constraints on deformation, including when fabric development occurred, the orientation of the stress field at the time of emplacement, and even the timing of movement along orogen-scale structures. An important caveat, however, is that monazite U-Th/Pb dates of leucogranites sometimes yield ambiguous results due to inheritance, recrystallization, and dissolution/reprecipitation.

Second, this study demonstrates several characteristics of monazite that make it ideally suited as a geochronometer among crustal granites. The widespread occurrence of inherited monazite in Himalayan granites suggests that a complete record of monazite crystallization may be preserved, providing valuable insight into earlier phases of melting and crystallization. Additionally, this study highlights the necessity in characterizing the zoning of chemical domains in monazite either through the use of X-ray maps via EPMA or by trace element analysis using LA-ICPMS to aid in the interpretation of monazite growth history.

Further work envisioned as a result of this study is quantification of inherited monazite and zircon in a Himalayan leucogranites as well as GHS migmatites. The behavior of these phases is crucial for understanding the thermal and chemical evolution of the crust. The proportion of U and Th that partitions into a melt or held by entrained accessory phases during anatexis represents an important parameter that must be assessed.

References

Aleinikoff, J.N., Schenck, W.S., Plank, M.O., Srogi, L., Fanning, C.M., Kamo, S.L., and Bosbyshell, H., 2006, Deciphering igneous and metamorphic events in high-grade rocks of the Wilmington Complex, Delaware: morphology, cathodoluminescence and backscattered electron zoning, and SHRIMP U-Pb geochronology of zircon and monazite: Geological Society of America Bulletin, v. 118, p. 39–64, doi: 10.1130/B25659.1.

Allègre, C.J., and Othman, D. Ben, 1980, Nd–Sr isotopic relationship in granitoid rocks and continental crust development: a chemical approach to orogenesis: Nature, v. 286, p. 335–342, doi: 10.1038/286335a0.

Annen, C., Scaillet, B., and Sparks, R., 2006, Thermal constraints on the emplacement rate of a large intrusive complex: the Manaslu leucogranite, Nepal Himalaya: Journal of Petrology, v. 47, p. 71–95, doi: 10.1093/petrology/egi068.

Aoya, M., Wallis, S.R., Terada, K., Lee, J., Kawakami, T., Wang, Y., and Heizler, M., 2005, North-south extension in the Tibetan crust triggered by granite emplacement: Geology, v. 33, p. 853, doi: 10.1130/G21806.1.

Arita, K., 1983, Origin of the inverted metamorphism of the lower Himalayas, Central Nepal: Tectonophysics, v. 95, p. 43–60, doi: 10.1016/0040-1951(83)90258-5.

Ayres, M., Harris, N., and Vance, D., 1997, Possible constraints on anatectic melt residence times from accessory mineral dissolution rates; an example from Himalayan leucogranites: Mineralogical Magazine, v. 61, p. 29–36.

Barbey, P., Allé, P., Brouand, M., and Albarède, F., 1995, Rare-earth patterns in zircons from the Manaslu granite and Tibetan Slab migmatites (Himalaya): insights in the origin and evolution of a crustally-derived granite magma: Chemical Geology, v. 125, p. 1–17.

Barbey, P., Brouand, M., Fort, P.L., and Pêcher, a., 1996, Granite-migmatite genetic link: the example of the Manaslu granite and Tibetan Slab migmatites in central Nepal: Lithos, v. 38, p. 63–79, doi: 10.1016/0024-4937(96)00005-9.

Beaumont, C., 2004, Crustal channel flows: 1. numerical models with applications to the tectonics of the Himalayan-Tibetan orogen: Journal of Geophysical Research, v. 109, p. 1–29, doi: 10.1029/2003JB002809.

Beaumont, C., and Jamieson, R., 2010, Himalayan Tibetan orogeny: Channel flow versus (critical) wedge models, a false dichotomy, *in* Leech, M.L., Klemperer, S.L., and Mooney, W.D. eds., Proceedings for the 25th Himalaya-Karakoram-Tibet Workshop: U.S. Geological Survey, Open File Report 2010-1099, p. 25–26.

Boehnke, P., Watson, E.B., Trail, D., Harrison, T.M., and Schmitt, A.K., 2013, Zircon saturation re-revisited: Chemical Geology, v. 351, p. 324–334, doi: 10.1016/j.chemgeo.2013.05.028.

Bollinger, L., Henry, P., and Avouac, J., 2006, Mountain building in the Nepal Himalaya: thermal and kinematic model: Earth and Planetary Science Letters, v. 244, p. 58–71, doi: 10.1016/j.epsl.2006.01.045.

Brouand, M., Banzet, G., and Barbey, P., 1990, Zircon behaviour during crustal anatexis. Evidence from the Tibetan Slab migmatites (Nepal): Journal of Volcanology and Geothermal Research, v. 44, p. 143–161, doi: 10.1016/0377-0273(90)90016-9.

Brown, M., 2001, Orogeny, migmatites and leucogranites: A review: Journal of Earth System Science, v. 110, p. 313–336, doi: 10.1007/BF02702898.

Brown, M., 2004, The mechanism of melt extraction from lower continental crust of orogens: Transactions of the Royal Society of Edinburgh: …, v. 95, doi: 10.1017/S0263593300000900.

Brown, M., Averkin, Y.A., McLellan, E.L., and Sawyer, E.W., 1995, Melt segregation in migmatites: Journal of Geophysical Research, v. 100, p. 15655, doi: 10.1029/95JB00517.

Brown, M., and Solar, G., 1998, Shear-zone systems and melts: feedback relations and self-organization in orogenic belts: Journal of Structural Geology, v. 20, p. 211–227.

Brown, M., and Solar, G.S., 1999, The mechanism of ascent and emplacement of granite magma during transpression: a syntectonic granite paradigm: Tectonophysics, v. 312, p. 1–33, doi: 10.1016/S0040-1951(99)00169-9.

Brown, L., Zhao, W., Nelson, K., Hauck, M., Alsdorf, D., Ross, A., Cogan, M., Clark, M., Liu, X., and Che, J., 1996, Bright spots, structure, and magmatism in southern Tibet from INDEPTH seismic reflection profiling: Science, v. 274, p. 1688–1690.

Catlos, E.., Gilley, L.., and Harrison, T.M., 2002, Interpretation of monazite ages obtained via in situ analysis: Chemical Geology, v. 188, p. 193–215, doi: 10.1016/S0009-2541(02)00099-2.

Catlos, E.J., Harrison, T.M., Manning, C.E., Grove, M., Rai, S.M., Hubbard, M.S., and Upreti, B.N., 2002, Records of the evolution of the Himalayan orogen from in situ Th–Pb ion microprobe dating of monazite: Eastern Nepal and western Garhwal: Journal of Asian Earth Sciences, v. 20, p. 459–479, doi: 10.1016/S1367-9120(01)00039-6.

Chambers, J., Caddick, M., Argles, T., Horstwood, M., Sherlock, S., Harris, N., Parrish, R., and Ahmad, T., 2009, Empirical constraints on extrusion mechanisms from the upper margin of an exhumed high-grade orogenic core, Sutlej valley, NW India: Tectonophysics, v. 477, p. 77–92, doi: 10.1016/j.tecto.2008.10.013.

Chen, L., Booker, J., Jones, A., Wu, N., Unsworth, M., Wei, W., and Tan, H., 1996, Electrically conductive crust in southern Tibet from INDEPTH magnetotelluric surveying: Science, v. 274, p. 1694–1696.

Cherniak, D.J., 2006, Pb and rare earth element diffusion in xenotime: Lithos, v. 88, p. 1–14, doi: 10.1016/j.lithos.2005.08.002.

Cherniak, D.J., and Pyle, J.M., 2008, Th diffusion in monazite: Chemical Geology, v. 256, p. 52–61, doi: 10.1016/j.chemgeo.2008.07.024.

Cherniak, D.J., and Watson, E.B., 2003, Diffusion in zircon: Reviews in mineralogy and geochemistry, v. 53, p. 113–143.

Cherniak, D.J., and Watson, E.B., 2001, Pb diffusion in zircon: Chemical Geology, v. 172, p. 5–24.

Cherniak, D.J., Watson, E.B., Grove, M., and Harrison, T.M., 2004, Pb diffusion in monazite: a combined RBS/SIMS study: Geochimica et Cosmochimica Acta, v. 68, p. 829–840, doi: 10.1016/j.gca.2003.07.012.

Clemens, J.D., and Vielzeuf, D., 1987, Constraints on melting and magma production in the crust: Earth and Planetary Science Letters, v. 86, p. 287–306, doi: 10.1016/0012-821X(87)90227-5.

Cocherie, A., Legendre, O., Peucat, J., and Kouamelan, A., 1998, Geochronology of polygenetic monazites constrained by in situ electron microprobe Th-U-total lead determination: Implications for lead behaviour in monazite: Geochimica et Cosmochimica Acta, v. 62, p. 2475–2497.

Colchen, M., Le Fort, P., and Pêcher, A., 1986, Recherches Géologiques dans L'Himalaya du Népal: Annapurna-Manaslu-Ganesh Himal: Notice de la carte géologique au 1/200,000: Paris, France, Centre National de la Recherche Scientifique.

Collins, W.J., and Williams, I.S., 1995, SHRIMP ionprobe dating of short-lived Proterozoic tectonic cycles in the northern Arunta Inlier, central Australia: Precambrian Research, v. 71, p. 69–89.

Copeland, P., Mark Harrison, T., and Le Fort, P., 1990, Age and cooling history of the Manaslu granite: implications for Himalayan tectonics: Journal of Volcanology and Geothermal Research, v. 44, p. 33–50, doi: 10.1016/0377-0273(90)90010-D.

Copeland, P., Parrish, R., and Harrison, T., 1988, Identification of inherited radiogenic Pb in monazite and its implications for U-Pb systematics: Nature, v. 333, p. 760–763.

Corfu, F., Hanchar, J.M., Hoskin, P.W.O., and Kinny, P., 2003, Atlas of zircon textures: Reviews in Mineralogy and Geochemistry, v. 53, p. 469–500.

Corrie, S.L., and Kohn, M.J., 2008, Trace-element distributions in silicates during prograde metamorphic reactions: implications for monazite formation: Journal of Metamorphic Geology, v. 26, p. 451–464, doi: 10.1111/j.1525-1314.2008.00769.x.

Cottle, J.M., Jessup, M.J., Newell, D.L., Horstwood, M.S. a., Noble, S.R., Parrish, R.R., Waters, D.J., and Searle, M.P., 2009, Geochronology of granulitized eclogite from the Ama Drime Massif: implications for the tectonic evolution of the South Tibetan Himalaya: Tectonics, v. 28, doi: 10.1029/2008TC002256.

Cottle, J.M., Jessup, M.J., Newell, D.L., Searle, M.P., Law, R.D., and Horstwood, M.S.A., 2007, Structural insights into the early stages of exhumation along an orogen-scale detachment: the South Tibetan Detachment System, Dzakaa Chu section, Eastern Himalaya: Journal of Structural Geology, v. 29, p. 1781–1797, doi: 10.1016/j.jsg.2007.08.007.

Cottle, J., Searle, M., Horstwood, M., and Waters, D., 2009, Timing of midcrustal metamorphism, melting, and deformation in the Mount Everest region of southern Tibet revealed by U-(Th)-Pb geochronology: The Journal of Geology, v. 117, p. 643–664, doi: 10.1086/605994.

Cottle, J.M., Waters, D.J., Riley, D., Beyssac, O., and Jessup, M.J., 2011, Metamorphic history of the South Tibetan Detachment System, Mt. Everest region, revealed by RSCM thermometry and phase equilibria modelling: Journal of Metamorphic Geology, v. 29, p. 561–582, doi: 10.1111/j.1525-1314.2011.00930.x.

DeCelles, P.G., 2000, Tectonic Implications of U-Pb Zircon Ages of the Himalayan Orogenic Belt in Nepal: Science, v. 288, p. 497–499, doi: 10.1126/science.288.5465.497.

Deniel, C., Vidal, P., and Fernandez, A., 1987, Isotopic study of the Manaslu granite (Himalaya, Nepal): inferences on the age and source of Himalayan leucogranites: Contributions to Mineralogy and Petrology, v. 96, p. 78–92.

Edwards, M., and Harrison, T., 1997, When did the roof collapse? Late Miocene north-south extension in the high Himalaya revealed by Th-Pb monazite dating of the Khula Kangri granite: Geology, v. 25, p. 543–546, doi: 10.1130/0091-7613(1997)025<0543.

Eggins, S.M., Grün, R., McCulloch, M.T., Pike, A.W.G., Chappell, J., Kinsley, L., Mortimer, G., Shelley, M., Murray-Wallace, C. V., Spötl, C., and Taylor, L., 2005, In situ U-series dating by laser-ablation multi-collector ICPMS: new prospects for

Quaternary geochronology: Quaternary Science Reviews, v. 24, p. 2523–2538, doi: 10.1016/j.quascirev.2005.07.006.

Eggins, S.M., Kinsley, L.P.J., and Shelley, J.M.G., 1998, Deposition and element fractionation processes during atmospheric pressure laser sampling for analysis by ICP-MS: Applied Surface Science, v. 127-129, p. 278–286, doi: 10.1016/S0169-4332(97)00643-0.

England, P., Le Fort, P., Molnar, P., and Pêcher, A., 1992, Heat sources for Tertiary metamorphism and anatexis in the Annapurna-Manaslu region central Nepal: Journal of Geophysical Research, v. 97, p. 2107–2128.

England, P., and Thompson, A., 1984, Pressure-temperature-time paths of regional metamorphism I. heat transfer during the evolution of regions of thickened continental crust: Journal of Petrology, v. 25, p. 894–928.

Le Fort, P., 1975, Himalayas: the collided range. present knowledge of the continental arc: American Journal of Science, v. 275, p. 1–44.

Le Fort, P., 1981, Manaslu leucogranite: a collision signature of the Himalaya a model for its genesis and emplacement: Journal of Geophysical Research, v. 86, p. 10545–10568.

Le Fort, P., Cuney, M., Deniel, C., France-Lanord, C., Sheppard, S.M.F.M.F., Upreti, B.N.N., and Vidal, P.H., 1987, Crustal generation of the Himalayan leucogranites: Tectonophysics, v. 134, p. 39–57, doi: 10.1016/0040-1951(87)90248-4.

Le Fort, P., and Raï, S.M., 1999, Pre-Tertiary felsic magmatism of the Nepal Himalaya: recycling of continental crust: Journal of Asian Earth Sciences, v. 17, p. 607–628, doi: 10.1016/S1367-9120(99)00015-2.

Foster, G., Parrish, R.R., Horstwood, M.S. a., Chenery, S., Pyle, J., and Gibson, H.D., 2004, The generation of prograde P–T–t points and paths; a textural, compositional, and chronological study of metamorphic monazite: Earth and Planetary Science Letters, v. 228, p. 125–142, doi: 10.1016/j.epsl.2004.09.024.

France-Lanord, C., and Le Fort, P., 1988, Crustal melting and granite genesis during the Himalayan collision orogenesis: Transactions of the Royal Society of Edinburgh: Earth Sciences, v. 79, p. 183–195, doi: 10.1017/S0263593300014206.

France-Lanord, C., Sheppard, S., and Le Fort, P., 1988, Hydrogen and oxygen isotope variations in the High Himalaya peraluminous Manaslu leucogranite: evidence for heterogeneous sedimentary source: Geochimica et Cosmochimica Acta, v. 52, p. 513–526.

Friedrich, A., Bowring, S., Martin, M., and Hodges, K., 1999, Short-lived continental magmatic arc at Connemara, western Irish Caledonides: Implications for the age of the Grampian orogeny: Geology, v. 27, p. 27–30, doi: 10.1130/0091-7613(1999)027<0027.

Fuchs, G., and Paudel, L., 1998, Note on the Tethyan Sedimentary Series of the Manaslu Region (Northern Nepal): Jahrbuch der Geologischen Bundesanstalt,, p. 45–50.

Gansser, A., 1964, Geology of the Himalayas: New York, Wiley-Interscience.

Gehrels, G., DeCelles, P., Martin, A., Ojha, T., Pinhassi, G., and Upreti, B., 2003, Initiation of the Himalayan orogen as an Early Paleozoic thin-skinned thrust belt: GSA Today, v. 13, p. 4–9.

Girard, M., and Bussy, F., 1999, Late Pan-African magmatism in the Himalaya: new geochronological and geochemical data from the Ordovician Tso Morari metagranites (Ladakh, NW India): Schweiz. Mineral. Petrogr. Mitt, v. 79, p. 399–418.

Guillot, S., and Le Fort, P., 1995, Geochemical constraints on the bimodal origin of High Himalayan leucogranites: Lithos, v. 35, p. 221–234, doi: 10.1016/0024-4937(94)00052-4.

Guillot, S., Le Fort, P., Pecher, A., Barman, M.R., and Aprahamian, J., 1995, Contact metamorphism and depth of emplacement of the Manaslu granite (central Nepal). Implications for Himalayan orogenesis: Tectonophysics, v. 241, p. 99–119, doi: 10.1016/0040-1951(94)00144-X.

Guillot, S., Hodges, K., Le Fort, P., and Pêcher, A., 1994, New constraints on the age of the Manaslu leucogranite: evidence for episodic tectonic denudation in the central Himalayas: Geology, v. 22, p. 559–562, doi: 10.1130/0091-7613(1994)022<0559.

Guillot, S., Pêcher, A., Rochette, P., and Le Fort, P., 1993, The emplacement of the Manaslu granite of central Nepal: field and magnetic susceptibility constraints, *in* Treloar, P. and Searle, M.P. eds., Himalayan Tectonics, Geological Society London Special Publication No 74, p. 413–428.

Hacker, B.R., 2000, Hot and Dry Deep Crustal Xenoliths from Tibet: Science, v. 287, p. 2463–2466, doi: 10.1126/science.287.5462.2463.

Hacker, B., Ritzwoller, M., and Xie, J., 2014, Partially melted, mica-bearing crust in Central Tibet: Tectonics,, p. 1408–1424, doi: 10.1002/2014TC003545.Received.

Hamet, J., and Allègre, C., 1976, Rb-Sr systematics in granite from central Nepal (Manaslu): significance of the Oligocene age and high 87Sr/86Sr ratio in Himalayan orogeny: Geology, v. 4, p. 470–472, doi: 10.1130/0091-7613(1976)4<470.

Hamet, J., and Allègre, C., 1978, Rb-Sr systematics in granite from central Nepal (Manaslu): significance of the Oligocene age and high 87Sr/86Sr ratio in Himalayan orogeny: comment and reply: reply: Geology, v. 6, p. 197, doi: 10.1130/0091-7613(1978)6<197.

Harlov, D.E., Wirth, R., and Hetherington, C.J., 2010, Fluid-mediated partial alteration in monazite: the role of coupled dissolution–reprecipitation in element redistribution and mass transfer: Contributions to Mineralogy and Petrology, v. 162, p. 329–348, doi: 10.1007/s00410-010-0599-7.

Harris, N., and Massey, J., 1994, Decompression and anatexis of Himalayan metapelites: Tectonics, v. 13, p. 1537–1546.

Harris, N., Massey, J., and Inger, S., 1993, The role of fluids in the formation of High Himalayan leucogranites: Geological Society, London, Special Publications, v. 74, p. 391–400, doi: 10.1144/GSL.SP.1993.074.01.26.

Harris, N., Vance, D., and Ayres, M., 2000, From sediment to granite: timescales of anatexis in the upper crust: Chemical Geology, v. 162, p. 155–167, doi: 10.1016/S0009-2541(99)00121-7.

Harrison, M.T., Grove, M., McKeegan, K.D., Coath, C.D., Lovera, O.M., and Fort, P.L., 1999, Origin and episodic emplacement of the Manaslu intrusive complex, central Himalaya: Journal of Petrology, v. 40, p. 3–19, doi: 10.1093/petroj/40.1.3.

Harrison, T.M., Mahon, K.I., Guillot, S., Hodges, K., Le Fort, P., and Pêcher, A., 1995, New constraints on the age of the Manaslu leucogranite: Evidence for episodic tectonic denudation in the central Himalaya: Comment and Reply: Geology, v. 23, p. 478–480.

Harrison, T.M., McKeegan, K., and LeFort, P., 1995, Detection of inherited monazite in the Manaslu leucogranite by 208Pb232Th ion microprobe dating: crystallization age and tectonic implications: Earth and Planetary Science Letters, v. 133, p. 271–282.

Hetherington, C.J., Harlov, D.E., and Budzyń, B., 2010, Experimental metasomatism of monazite and xenotime: mineral stability, REE mobility and fluid composition: Mineralogy and Petrology, v. 99, p. 165–184, doi: 10.1007/s00710-010-0110-1.

Hintersberger, E., Thiede, R.C., Strecker, M.R., and Hacker, B.R., 2010, East-west extension in the NW Indian Himalaya: Geological Society of America Bulletin, v. 122, p. 1499–1515, doi: 10.1130/B26589.1.

Hodges, K., 2000, Tectonics of the Himalaya and southern Tibet from two perspectives: Geological Society of America Bulletin, v. 112, p. 324–350, doi: 10.1130/0016-7606(2000)112<324.

Horstwood, M.S.A., Foster, G.L., Parrish, R.R., Noble, S.R., and Nowell, G.M., 2003, Common-Pb corrected in situ U-Pb accessory mineral geochronology by LA-MC-ICP-MS: Journal of Analytical Atomic Spectrometry, v. 18, p. 837, doi: 10.1039/b304365g.

Horton, F., Lee, J., Hacker, B., Bowman-Kamaha'o, M., and Cosca, M., 2014, Himalayan gneiss dome formation in the middle crust and exhumation by normal faulting: New geochronology of Gianbul dome, northwestern India: Geological Society of America Bulletin,, doi: 10.1130/B31005.1.

Imayama, T., and Suzuki, K., 2013, Carboniferous inherited grain and age zoning of monazite and xenotime from leucogranites in far-eastern Nepal: Constraints from electron probe microanalysis: American Mineralogist, v. 98, p. 1393–1406, doi: 10.2138/am.2013.4267.

Inger, S., and Harris, N., 1993, Geochemical constraints on leucogranite magmatism in the Langtang Valley, Nepal Himalaya: Journal of Petrology, v. 34, p. 345–368.

Jamieson, R.A., Unsworth, M.J., Harris, N.B.W., Rosenberg, C.L., and Schulmann, K., 2011, Crustal melting and the flow of mountains: Elements, v. 7, p. 253–260.

King, J., Harris, N., Argles, T., Parrish, R., and Zhang, H., 2010, Contribution of crustal anatexis to the tectonic evolution of Indian crust beneath southern Tibet: Geological Society of America Bulletin, v. 123, p. 218–239, doi: 10.1130/B30085.1.

Kohn, M.J., 2008, P-T-t data from central Nepal support critical taper and repudiate large-scale channel flow of the Greater Himalayan Sequence: Geological Society of America Bulletin, v. 120, p. 259–273, doi: 10.1130/B26252.1.

Kohn, M.J., Wieland, M.S., Parkinson, C.D., and Upreti, B.N., 2005, Five generations of monazite in Langtang gneisses: implications for chronology of the Himalayan metamorphic core: Journal of Metamorphic Geology, v. 23, p. 399–406, doi: 10.1111/j.1525-1314.2005.00584.x.

Kylander-Clark, A.R.C., Hacker, B.R., and Cottle, J.M., 2013, Laser-ablation split-stream ICP petrochronology: Chemical Geology, v. 345, p. 99–112, doi: 10.1016/j.chemgeo.2013.02.019.

Langille, J.M., Jessup, M.J., Cottle, J.M., Lederer, G., and Ahmad, T., 2012, Timing of metamorphism, melting and exhumation of the Leo Pargil dome, northwest India: Journal of Metamorphic Geology,, doi: 10.1111/j.1525-1314.2012.00998.x.

Larson, K.P., Cottle, J.M., and Godin, L., 2011, Petrochronologic record of metamorphism and melting in the upper Greater Himalayan sequence, Manaslu–Himal Chuli Himalaya, west-central Nepal: Lithosphere, v. 3, p. 379 –392, doi: 10.1130/L149.1.

Larson, K.P., Godin, L., and Price, R.A., 2010, Relationships between displacement and distortion in orogens: linking the Himalayan foreland and hinterland in central

Nepal: Geological Society of America Bulletin, v. 122, p. 1116–1134, doi: 10.1130/B30073.1.

Lee, J., Hacker, B., Dinklage, W., and Wang, Y., 2000, Evolution of the Kangmar Dome, southern Tibet: structural, petrologic, and thermochronologic constraints: Tectonics, v. 19, p. 872–895.

Lee, J., Hacker, B., and Wang, Y., 2004, Evolution of North Himalayan gneiss domes: structural and metamorphic studies in Mabja Dome, southern Tibet: Journal of Structural Geology, v. 26, p. 2297–2316, doi: 10.1016/j.jsg.2004.02.013.

Leech, M.L., 2008, Does the Karakoram fault interrupt mid-crustal channel flow in the western Himalaya?: Earth and Planetary Science Letters, v. 276, p. 314–322, doi: 10.1016/j.epsl.2008.10.006.

Leech, M.L., 2009, Reply to comment by M.P. Searle and R.J. Phillips (2009) and R.R. Parrish (2009) on: “Does the Karakoram fault interrupt mid-crustal channel flow in the western Himalaya?” by Mary L. Leech, Earth and Planetary Science Letters 276 (2008) 314–322: Earth and Planetary Science Letters, v. 286, p. 592–595, doi: 10.1016/j.epsl.2009.05.039.

Ludwig, K.R., 2000, User’s manual for Isoplot/Ex version 2.4: A geochronological toolkit for Microsoft Excel. Berkeley Geochronological Center, Special Publication No. 1a:.

Makovsky, Y., Klemperer, S., Ratschbacher, L., Brown, L., Li, M., Zhao, W., and Meng, F., 1996, INDEPTH wide-angle reflection observation of P-wave-to-S-wave conversion from crustal bright spots in Tibet: Science, v. 274, p. 1690–1691.

Marquer, D., Chawla, H.S., and Challandes, N., 2000, Pre-alpine high grade metamorphism in High Himalaya: Eclogae Geologicae Helvetiae, v. 93, p. 207–220.

Martin, A.J., Gehrels, G.E., and DeCelles, P.G., 2007, The tectonic significance of (U,Th)/Pb ages of monazite inclusions in garnet from the Himalaya of central Nepal: Chemical Geology, v. 244, p. 1–24, doi: 10.1016/j.chemgeo.2007.05.003.

McDonough, W., and Sun, S., 1995, The composition of the Earth: Chemical Geology, v. 2541, p. 223–253.

McFarlane, C., and McCulloch, M., 2007, Coupling of in-situ Sm–Nd systematics and U–Pb dating of monazite and allanite with applications to crustal evolution studies: Chemical Geology, v. 245, p. 45–60, doi: 10.1016/j.chemgeo.2007.07.020.

Meldrum, A., Boatner, L.A., Weber, W.J., and Ewing, R.C., 1998, Radiation damage in zircon and monazite: Geochimica et Cosmochimica Acta, v. 62, p. 2509–2520, doi: 10.1016/S0016-7037(98)00174-4.

Miller, C., Thöni, M., Frank, W., Grasemann, B., Klötzli, U., Guntli, P., and Draganits, E., 2001, The early Palaeozoic magmatic event in the northwest Himalaya, India: source, tectonic setting and age of emplacement: Geological Magazine, v. 138, p. 237–251, doi: 10.1017/S0016756801005283.

Montel, J.-M., 1993, A model for monazite/melt equilibrium and application to the generation of granitic magmas: Chemical Geology, v. 110, p. 127–146, doi: 10.1016/0009-2541(93)90250-M.

Montel, J., 1986, Experimental determination of the solubility of Ce-monazite in SiO2-Al2O3-K2O-Na2O melts at 800 ^{o}C, 2 kbar, under H2O-saturated conditions: Geology, v. 14, p. 659–662, doi: 10.1130/0091-7613(1986)14<659.

Murphy, M.A., Yin, A., Kapp, P., Harrison, T.M., Manning, C.E., Ryerson, F.J., Lin, D., and Jinghui, G., 2002, Structural evolution of the Gurla Mandhata detachment system, southwest Tibet: implications for the eastward extent of the Karakoram fault system: Geological Society of America Bulletin, v. 114, p. 428–447, doi: 10.1130/0016-7606(2002)114<0428:SEOTGM>2.0.CO;2.

Nabelek, P.I., and Liu, M., 2007, Petrologic and thermal constraints on the origin of leucogranites in collisional orogens: Transactions of the Royal Society of Edinburgh: Earth Sciences, v. 95, p. 73–85, doi: 10.1017/S0263593300000936.

Nabelek, P.I., Whittington, A.G., and Hofmeister, A.M., 2010, Strain heating as a mechanism for partial melting and ultrahigh temperature metamorphism in convergent orogens: implications of temperature-dependent thermal diffusivity and rheology: Journal of Geophysical Research, v. 115, p. 1–17, doi: 10.1029/2010JB007727.

Nelson, D., Brown, D., Zhao, W., Kuo, J., Che, J., Liu, X., Klemperer, L., Makovsky, Y., Meissner, R., Mechie, J., Kind, R., Wenzel, F., Ni, J., Nabelek, J., et al. 1996, Tibet : Synthesis Synthesis of of Project Project INDEPTH Tibet : Results:.

Parrish, R.R., 2009, Comment on: "Does the Karakoram fault interrupt mid-crustal channel flow in the western Himalaya?" by Mary L. Leech, Earth and Planetary Science Letters 276 (2008) 314–322: Earth and Planetary Science Letters, v. 286, p. 586–588, doi: 10.1016/j.epsl.2009.05.038.

Parrish, R., 1990, U-Pb dating of monazite and its application to geological problems: Canadian Journal of Earth Sciences, v. 27, p. 1431–1450.

Parrish, R., and Hodges, K., 1996, Isotopic constraints on the age and provenance of the Lesser and Greater Himalayan sequences, Nepalese Himalaya: Geological Society of America Bulletin, v. 108, p. 904–911, doi: 10.1130/0016-7606(1996)108<0904.

Paterson, M., 2001, A granular flow theory for the deformation of partially molten rock: Tectonophysics, v. 335, p. 51–61.

Patiño Douce, A.E., and Harris, N., 1998, Experimental Constraints on Himalayan Anatexis: Journal of Petrology, v. 39, p. 689–710, doi: 10.1093/petroj/39.4.689.

Paton, C., Hellstrom, J., Paul, B., Woodhead, J., and Hergt, J., 2011, Iolite: Freeware for the visualisation and processing of mass spectrometric data: Journal of Analytical Atomic Spectrometry, v. 26, p. 2508, doi: 10.1039/c1ja10172b.

Paton, C., Woodhead, J.D., Hellstrom, J.C., Hergt, J.M., Greig, A., and Maas, R., 2010, Improved laser ablation U-Pb zircon geochronology through robust downhole fractionation correction: Geochemistry Geophysics Geosystems, v. 11, doi: 10.1029/2009GC002618.

Pognante, U., Castelli, D., Benna, P., Genovese, G., Oberli, F., Meier, M., and Tonarini, S., 1990, The crystalline units of the High Himalayas in the Lahul–Zanskar region (northwest India): metamorphic–tectonic history and geochronology of the collided and imbricated Indian plate: Geological Magazine, v. 127, p. 101–116, doi: 10.1017/S0016756800013807.

Poitrasson, F., Chenery, S., and Shepherd, T., 2000, Electron microprobe and LA-ICP-MS study of monazite hydrothermal alteration: implications for U-Th-Pb geochronology and nuclear ceramics: Geochimica et Cosmochimica Acta, v. 64, p. 3283–3297.

Prince, C., Harris, N., and Vance, D., 2001, Fluid-enhanced melting during prograde metamorphism: Journal of the Geological Society, v. 158, p. 233–241, doi: 10.1144/jgs.158.2.233.

Pyle, J., and Spear, F., 2003, Four generations of accessory-phase growth in low-pressure migmatites from SW New Hampshire: American Mineralogist, v. 88, p. 338–351.

Quigley, M.C., Liangjun, Y., Gregory, C., Corvino, a., Sandiford, M., Wilson, C.J.L., and Xiaohan, L., 2008, U–Pb SHRIMP zircon geochronology and T–t–d history of the Kampa Dome, southern Tibet: Tectonophysics, v. 446, p. 97–113, doi: 10.1016/j.tecto.2007.11.004.

Rapp, R.P., and Watson, E.B., 1986, Monazite solubility and dissolution kinetics: implications for the thorium and light rare earth chemistry of felsic magmas: Contributions to Mineralogy and Petrology, v. 94, p. 304–316, doi: 10.1007/BF00371439.

Reichardt, H., Weinberg, R.F., Andersson, U.B., and Fanning, C.M., 2010, Hybridization of granitic magmas in the source: the origin of the Karakoram Batholith, Ladakh, NW India: Lithos, v. 116, p. 249–272, doi: 10.1016/j.lithos.2009.11.013.

Robinson, D.M., DeCelles, P.G., and Copeland, P., 2006, Tectonic evolution of the Himalayan thrust belt in western Nepal: implications for channel flow models: Geological Society of America Bulletin, v. 118, p. 865–885, doi: 10.1130/B25911.1.

Rosenberg, C.L., and Handy, M.R., 2005, Experimental deformation of partially melted granite revisited: implications for the continental crust: Journal of Metamorphic Geology, v. 23, p. 19–28, doi: 10.1111/j.1525-1314.2005.00555.x.

Royden, L., 1993, The steady-state thermal structure of eroding orogenic belts and accretionary prisms: Journal of Geophysical Research, v. 98, p. 4487–4507.

Rubatto, D., 2002, Zircon trace element geochemistry: partitioning with garnet and the link between U–Pb ages and metamorphism: Chemical Geology, v. 184, p. 123–138, doi: 10.1016/S0009-2541(01)00355-2.

Rubin, A., 1995, Getting granite dikes out of the source region: Journal of Geophysical Research, v. 100, p. 5911–5929.

Sawyer, E., 1994, Melt segregation in the continental crust: Geology, v. 22, p. 1019–1022, doi: 10.1130/0091-7613(1994)022<1019.

Sawyer, E.W., 2001, Melt segregation in the continental crust: distribution and movement of melt in anatectic rocks: Journal of Metamorphic Geology, v. 19, p. 291–309, doi: 10.1046/j.0263-4929.2000.00312.x.

Scaillet, B., France-Lanord, C., and Le Fort, P., 1990, Badrinath-Gangotri plutons (Garhwal, India) petrological and geochemical evidence for fractionation processes in a high Himalayan leucogranite: Journal of Volcanology and Geothermal Research, v. 44, p. 163–188.

Scaillet, B., Holtz, F., Pichavant, M., and Schmidt, M., 1996, Viscosity of Himalayan leucogranites: implications for mechanisms of granitic magma ascent: Journal of Geophysical Research, v. 101, p. 27691–27699.

Schärer, U., 1984, The effect of initial 230Th disequilibrium on young U-Pb ages: the Makalu case, Himalaya: Earth and Planetary Science Letters, v. 67, p. 191–204.

Schärer, U., and Allègre, C.J., 1983, The Palung granite (Himalaya); high-resolution U-Pb systematics in zircon and monazite: Earth and Planetary Science Letters, v. 63, p. 423–432.

Schärer, U., Xu, R., and Allègre, C., 1986, U-(Th)-Pb systematics and ages of Himalayan leucogranites, South Tibet: Earth and Planetary Science Letters, v. 77, p. 35–48.

Schelling, D., 1992, The tectonostratigraphy and structure of the eastern Nepal Himalaya: Tectonics, v. 11, p. 925–943.

Schelling, D., and Arita, K., 1991, Thrust tectonics, crustal shortening, and the structure of the far-eastern Nepal Himalaya: Tectonics, v. 10, p. 851–862.

Schulmann, K., Lexa, O., Štípská, P., Racek, M., Tajčmanová, L., Konopásek, J., Edel, J.-B., Peschler, a., and Lehmann, J., 2008, Vertical extrusion and horizontal channel flow of orogenic lower crust: key exhumation mechanisms in large hot orogens?: Journal of Metamorphic Geology, v. 26, p. 273–297, doi: 10.1111/j.1525-1314.2007.00755.x.

Searle, M., 2013, Crustal melting, ductile flow, and deformation in mountain belts: Cause and effect relationships: Lithosphere, v. 5, p. 547–554, doi: 10.1130/RF.L006.1.

Searle, M.P., Cottle, J.M., Streule, M.J., and Waters, D.J., 2010, Crustal melt granites and migmatites along the Himalaya: melt source, segregation, transport and granite emplacement mechanisms: Earth and Environmental Science Transactions of the Royal Society of Edinburgh, v. 100, p. 219–233, doi: 10.1017/S175569100901617X.

Searle, M., and Godin, L., 2003, The South Tibetan Detachment and the Manaslu Leucogranite: a structural reinterpretation and restoration of the Annapurna-Manaslu Himalaya, Nepal: The Journal of Geology, v. 111, p. 505–523.

Searle, M.P., Law, R.D., Godin, L., Larson, K.P., Streule, M.J., Cottle, J.M., and Jessup, M.J., 2008, Defining the Himalayan Main Central Thrust in Nepal: Journal of the Geological Society, v. 165, p. 523–534, doi: 10.1144/0016-76492007-081.

Searle, M., Noble, S., Hurford, A., and Rex, D., 1999, Age of crustal melting, emplacement and exhumation history of the Shivling Leucogranite, Garhwal Himalaya: Geological Magazine, v. 136, p. 513–525.

Searle, M.P., and Phillips, R.J., 2009, Comment on: "Does the Karakoram fault interrupt mid-crustal channel flow in the western Himalaya?" by Mary L. Leech, Earth and Planetary Science Letters 276 (2008) 314–322: Earth and Planetary Science Letters, v. 286, p. 589–591, doi: 10.1016/j.epsl.2009.05.036.

Seydoux-Guillaume, A.-M., Paquette, J.-L., Wiedenbeck, M., Montel, J.-M., and Heinrich, W., 2002, Experimental resetting of the U–Th–Pb systems in monazite: Chemical Geology, v. 191, p. 165–181, doi: 10.1016/S0009-2541(02)00155-9.

Simpson, R., Parrish, R., Searle, M., and Waters, D., 2000, Two episodes of monazite crystallization during metamorphism and crustal melting in the Everest region of the Nepalese Himalaya: Geology, v. 28, p. 403–406, doi: 10.1130/0091-7613(2000)28<403.

Singh, S., and Jain, A.K., 2003, Himalayan granitoids: Journal of the Virtual Explorer, v. 11, p. 1–20.

Sláma, J., Košler, J., Condon, D.J., Crowley, J.L., Gerdes, A., Hanchar, J.M., Horstwood, M.S.A., Morris, G. a., Nasdala, L., Norberg, N., Schaltegger, U., Schoene, B., Tubrett, M.N., and Whitehouse, M.J., 2008, Plešovice zircon — A new natural reference material for U–Pb and Hf isotopic microanalysis: Chemical Geology, v. 249, p. 1–35, doi: 10.1016/j.chemgeo.2007.11.005.

Spear, F.S., and Pyle, J.M., 2002, Apatite, monazite, and xenotime in metamorphic rocks: Reviews in Mineralogy and Geochemistry, v. 48, p. 293–335.

Steiger, R., and Jäger, E., 1977, Subcommission on geochronology: convention on the use of decay constants in geo-and cosmochronology: Earth and Planetary Science Letters, v. 36, p. 359–362.

Stepanov, A.S., Hermann, J., Rubatto, D., and Rapp, R.P., 2012, Experimental study of monazite/melt partitioning with implications for the REE, Th and U geochemistry of crustal rocks: Chemical Geology, v. 300-301, p. 200–220, doi: 10.1016/j.chemgeo.2012.01.007.

Teufel, S., and Heinrich, W., 1997, Partial resetting of the U-Pb isotope system in monazite through hydrothermal experiments: An SEM and U-Pb isotope study: Chemical Geology, v. 137, p. 273–281, doi: 10.1016/S0009-2541(96)00161-1.

Teyssier, C., and Whitney, D., 2002, Gneiss domes and orogeny: Geology, v. 30, p. 1139–1142, doi: 10.1130/0091-7613(2002)030<1139.

Thiede, R.C., Arrowsmith, J.R., Bookhagen, B., McWilliams, M., Sobel, E.R., Strecker, M.R., and Haute, V. Den, 2006, Dome formation and extension in the Tethyan Himalaya, Leo Pargil, northwest India: Geological Society of America Bulletin, v. 118, p. 635–650, doi: 10.1130/B25872.1.

Thompson, A., and Connolly, J., 1995, Melting of the continental crust: some thermal and petrological constraints on anatexis in continental collison zones and other tectonic settings: Journal of Geophysical Research, v. 100, p. 15565–15579.

Thöni, M., Miller, C., Hager, C., Grasemann, B., and Horschinegg, M., 2012, New geochronological constraints on the thermal and exhumation history of the Lesser and Higher Himalayan Crystalline Units in the Kullu–Kinnaur area of Himachal Pradesh (India): Journal of Asian Earth Sciences, v. 52, p. 98–116, doi: 10.1016/j.jseaes.2012.02.015.

Unsworth, M.J., Jones, A.G., Wei, W., Marquis, G., Gokarn, S.G., Spratt, J.E., Bedrosian, P., Booker, J., Leshou, C., Clarke, G., Shenghui, L., Chanhong, L., Ming, D., Sheng, J., et al. 2005, Crustal rheology of the Himalaya and Southern Tibet inferred from magnetotelluric data.: Nature, v. 438, p. 78–81, doi: 10.1038/nature04154.

Vermeesch, P., 2012, On the visualisation of detrital age distributions: Chemical Geology, v. 312-313, p. 190–194, doi: 10.1016/j.chemgeo.2012.04.021.

Vidal, P., 1978, Rb-Sr systematics in granite from central Nepal (Manaslu): significance of the Oligocene age and high 87Sr/86Sr ratio in Himalayan orogeny: comment and reply: comment: Geology, v. 6, p. 196, doi: 10.1130/0091-7613(1978)6<196.

Vidal, P., Cocherie, A., and Le Fort, P., 1982, Geochemical investigations of the origin of the Manaslu leucogranite (Himalaya, Nepal): Geochimica et Cosmochimica Acta, v. 46, p. 2279–2292.

Viskupic, K., and Hodges, K. V., 2001, Monazite–xenotime thermochronometry: methodology and an example from the Nepalese Himalaya: Contributions to Mineralogy and Petrology, v. 141, p. 233–247, doi: 10.1007/s004100100239.

Viskupic, K., Hodges, K. V, and Bowring, S. a, 2005, Timescales of melt generation and the thermal evolution of the Himalayan metamorphic core, Everest region, eastern Nepal: Contributions to Mineralogy and Petrology, v. 149, p. 1–21, doi: 10.1007/s00410-004-0628-5.

Watson, E.B., and Harrison, T.M., 1983, Zircon saturation revisited: temperature and composition effects in a variety of crustal magma types: Earth and Planetary Science Letters, v. 64, p. 295–304, doi: 10.1016/0012-821X(83)90211-X.

Watson, E.B., Vicenzi, E.P., and Rapp, R.P., 1989, Inclusion/host relations involving accessory minerals in high-grade metamorphic and anatectic rocks: Contributions to Mineralogy and Petrology, v. 101, p. 220–231, doi: 10.1007/BF00375308.

Watt, G., and Harley, S., 1993, Accessory phase controls on the geochemistry of crustal melts and restites produced during water-undersaturated partial melting: Contributions to Mineralogy and Petrology, v. 114, p. 550–566.

Weinberg, R., 1996, Ascent mechanism of felsic magmas: news and views: Transactions of the Royal Society of Edinburgh: Earth Sciences, v. 87, p. 95–103, doi: 10.1017/S0263593300006519.

Weinberg, R.F., 1999, Mesoscale pervasive felsic magma migration: alternatives to dyking: Lithos, v. 46, p. 393–410, doi: 10.1016/S0024-4937(98)00075-9.

Weinberg, R.F., and Mark, G., 2008, Magma migration, folding, and disaggregation of migmatites in the Karakoram Shear Zone, Ladakh, NW India: Geological Society of America Bulletin, v. 120, p. 994–1009, doi: 10.1130/B26227.1.

White, L.T., and Ireland, T.R., 2012, High-uranium matrix effect in zircon and its implications for SHRIMP U–Pb age determinations: Chemical Geology, v. 306-307, p. 78–91, doi: 10.1016/j.chemgeo.2012.02.025.

White, N., Parrish, R., Bickle, M., Najman, Y., Burbank, D., and Maithani, A., 2001, Metamorphism and exhumation of the NW Himalaya constrained by U–Th–Pb analyses of detrital monazite grains from early foreland basin sediments: Journal of the Geological Society, v. 158, p. 625–635.

Whitney, D., and Evans, B., 2010, Abbreviations for names of rock-forming minerals: American mineralogist, v. 95, p. 185–187, doi: 10.2138/am.2010.3371.

Wiedenbeck, M., Alle, P., and Corfu, F., 1995, Three natural zircon standards for U-Th-Pb, Lu-Hf, trace element and REE analyses: Geostandards Newsletter, v. 19, p. 1–23, doi: 10.1111/j.1751-908X.1995.tb00147.x.

Williams, M.L., Jercinovic, M.J., Harlov, D.E., Budzyń, B., and Hetherington, C.J., 2011, Resetting monazite ages during fluid-related alteration: Chemical Geology, v. 283, p. 218–225, doi: 10.1016/j.chemgeo.2011.01.019.

Williams, M.L., Jercinovic, M.J., and Hetherington, C.J., 2007, Microprobe monazite geochronology: understanding geologic processes by integrating composition and chronology: Annual Review of Earth and Planetary Sciences, v. 35, p. 137–175, doi: 10.1146/annurev.earth.35.031306.140228.

Williams, M., Jercinovic, M., and Terry, M., 1999, Age mapping and dating of monazite on the electron microprobe: deconvoluting multistage tectonic histories: Geology, v. 27, p. 1023–1026, doi: 10.1130/0091-7613(1999)027<1023.

Wolf, M., and London, D., 1995, Incongruent dissolution of REE-and Sr-rich apatite in peraluminous granitic liquids: differential apatite, monazite, and xenotime solubilities during anatexis: American Mineralogist, v. 80, p. 765–775.

Zeitler, P., Koons, P., Bishop, M., Chamberlain, C., Craw, D., Edwards, M., Hamidullah, S., Jan, M., Khan, A., Khattak, M., Kidd, W., Mackie, R., Meltzer, A., Park, S., et al. 2001, Crustal reworking at Nanga Parbat, Pakistan: metamorphic consequences of thermal-mechanical coupling facilitated by erosion: Tectonics, v. 20, p. 712–728, doi: 200110.1029/2000TC001243.

Zeng, L., Asimow, P.D., and Saleeby, J.B., 2005, Coupling of anatectic reactions and dissolution of accessory phases and the Sr and Nd isotope systematics of anatectic melts from a metasedimentary source: Geochimica et Cosmochimica Acta, v. 69, p. 3671–3682, doi: 10.1016/j.gca.2005.02.035.

Zhang, H., Harris, N., Parrish, R., Kelley, S., Zhang, L., Rogers, N., Argles, T., and King, J., 2004, Causes and consequences of protracted melting of the mid-crust exposed in the North Himalayan antiform: Earth and Planetary Science Letters, v. 228, p. 195–212, doi: 10.1016/j.epsl.2004.09.031.

Zhu, X.K., and O’Nions, R.K., 1999, Monazite chemical composition: some implications for monazite geochronology: Contributions to Mineralogy and Petrology, v. 137, p. 351–363, doi: 10.1007/s004100050555.

Appendices

Appendix A Analytical methods for Leo Pargil

EPMA x-ray chemical mapping

Analyses were carried out in beam scan mode using 15 kV accelerating voltage, 200 nA beam current (equating to a ~1 μm^3 interaction volume), and a dwell time of 25 ms. Monazite is relatively homogeneous with respect to the LREE, but may show considerable variation in Th, U, and Y, with the geochemical behavior of Y serving as a proxy for HREE (Foster et al. 2004). Understanding the distribution of these elements potentially provides important information on the growth history of individual crystals (Williams et al. 1999, 2007; Zhu and O'Nions, 1999; Cocherie et al. 1998; Stepanov et al. 2012).

LA-MC-ICPMS U-Th/Pb geochronology

The laser system utilizes a HelEx ("helium excimer") sample cell (Eggins et al. 1998, 2005) designed for enhanced signal intensity and rapid washout times using He carrier gas. Helium carrier gas conveys the laser aerosol to a glass mixing-bulb where Ar is added to stabilize the input to the plasma. Boiled liquid argon and ultra-high purity helium are passed through activated charcoal and gold-coated quartz sand filters upstream of the mass flow controllers to reduce ^{204}X (where X includes ^{204}Pb and ^{204}Hg) backgrounds to <200 cps. The collector array on the Nu Plasma is configured to measure ^{238}U and ^{232}Th on two high-mass side Faraday cups equipped with 10^{11} ohm resistors and ^{208}Pb, ^{207}Pb, ^{206}Pb, and ^{204}X on four low-mass side ETP discrete dynode secondary electron multipliers.

Ablations were conducted for 40 seconds each at 4.8 J/cm^2 fluence, a frequency of 3 Hz, and a pit diameter of approximately 7 μm yielding craters 5-6 μm deep (as assessed by optical microscopy). Five to ten spot analyses were collected on each monazite grain, targeting domains with different trace element chemistry visible in x-ray maps, including cores and rims. Location of individual laser pits was confirmed with an optical microscope after analysis. Utilizing a standard-sample bracketing technique, analyses of reference materials with known isotopic compositions were measured before and after each set of ten unknown analyses. Reference materials consisted of several monazite grains or fragments with matrices similar to the unknowns and published isotopic ages including “44069” (424 Ma Pb/U ID-TIMS age; Aleinikoff et al. 2006), “FC-1” (55.7 Ma Pb/U ID-TIMS age; Horstwood et al. 2003) and “554” (45 Ma Pb/Th age; Harrison et al. 1999). Concordia and weighted mean date plots were calculated in Isoplot v2.4 (Ludwig, 2000) using the ^{238}U, ^{235}U, and ^{232}Th decay constants of Steiger and Jäger (1977).

LA-ICPMS Trace Element analysis

Chemical domains identified during x-ray mapping were targeted for trace element analysis by sampling next to U-Th/Pb ablation pits. Following analysis, optical petrographic microscope images of monazite grains were compared to x-ray maps to ensure trace element and U-Th/Pb ablation pits fall within targeted chemical domains. Additionally, the ablation profile was inspected for anomalous or abrupt changes in intensity, and based on this three-dimensional assessment of whether each spot analysis sampled a single domain, analyses located on domain boundaries or fractures were excluded from the dataset. Ablations were conducted for 30 seconds each at 3.2 J/cm^2

fluence, a frequency of 3 Hz, and a pit diameter of approximately 6 μm yielding craters 3-4 μm deep.

Because the AttoM is a relatively new instrument, we briefly describe the analytical routine below. In Linked Scan mode, the magnet current is ramped up and down in a controlled manner such that a complete cycle (m/z 6 – 250 – 6) can be completed every 220ms (100ms each direction + 20ms settle time). To maximize counting time, each isotope of interest is deflected into the single discrete dynode secondary electron multiplier by simultaneous use of the magnet and the post-ESA deflectors. As the magnet sweeps, each mass remains in the ion counter for up to 40% of its mass along the magnet sweep. Elemental abundances and their uncertainties are calculated using a simple matrix-matched sample-standard bracketing approach in Iolite v. 2.1.2 (Paton et al. 2010) including corrections for baseline and instrumental drift.

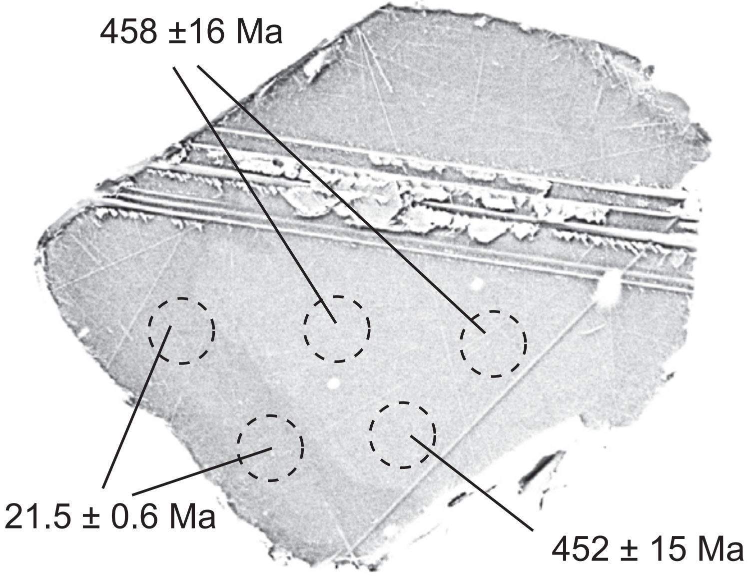

Appendix B Back-scattered electron (BSE) image of LP09_167_m003 with spot analyses and ^{208}Pb/^{232}Th ages. Note colors are inverted, with darker shading reflecting greater abundance of heavy atoms.